



UNIL | Université de Lausanne

Unicentre

CH-1015 Lausanne

<http://serval.unil.ch>

Year : 2015

THREE-DIMENSIONAL HYDRODYNAMIC NUMERICAL
MODELLING OF FOLD NAPPE FORMATION, BASEMENT-COVER
DEFORMATION AND SLAB DETACHMENT WITH APPLICATIONS
TO THE HELVETIC NAPPE SYSTEM (W SWITZERLAND)

Marina von Tscharner

von Tscharner Marina, 2015, Three-dimensional hydrodynamic numerical modelling of fold nappe formation, basement-cover deformation and slab detachment with applications to the Helvetic nappe system (W Switzerland)

Originally published at : Thesis, University of Lausanne

Posted at the University of Lausanne Open Archive <http://serval.unil.ch>
Document URN : urn:nbn:ch:serval-BIB_0EBE923D5B3D4

Droits d'auteur

L'Université de Lausanne attire expressément l'attention des utilisateurs sur le fait que tous les documents publiés dans l'Archive SERVAL sont protégés par le droit d'auteur, conformément à la loi fédérale sur le droit d'auteur et les droits voisins (LDA). A ce titre, il est indispensable d'obtenir le consentement préalable de l'auteur et/ou de l'éditeur avant toute utilisation d'une oeuvre ou d'une partie d'une oeuvre ne relevant pas d'une utilisation à des fins personnelles au sens de la LDA (art. 19, al. 1 lettre a). A défaut, tout contrevenant s'expose aux sanctions prévues par cette loi. Nous déclinons toute responsabilité en la matière.

Copyright

The University of Lausanne expressly draws the attention of users to the fact that all documents published in the SERVAL Archive are protected by copyright in accordance with federal law on copyright and similar rights (LDA). Accordingly it is indispensable to obtain prior consent from the author and/or publisher before any use of a work or part of a work for purposes other than personal use within the meaning of LDA (art. 19, para. 1 letter a). Failure to do so will expose offenders to the sanctions laid down by this law. We accept no liability in this respect.



UNIL | Université de Lausanne

Faculté des géosciences et de l'environnement
Institut des Sciences de la Terre

**THREE-DIMENSIONAL HYDRODYNAMIC NUMERICAL
MODELLING OF FOLD NAPPE FORMATION,
BASEMENT-COVER DEFORMATION AND SLAB
DETACHMENT WITH APPLICATIONS TO THE HELVETIC
NAPPE SYSTEM (W SWITZERLAND)**

Thèse de doctorat
présentée à la faculté des géosciences et de l'environnement de l'université de Lausanne par

MARINA VON TSCHARNER
MSc, ETH Zurich

pour l'obtention du grade de Docteur en sciences de la Terre

Jury

Prof. Dr. Stefan M. Schmalholz, Directeur de Thèse
Prof. Dr. Boris Kaus, Expert externe
Prof. Dr. Yury Podladchikov, Expert interne
sous la présidence du Prof. Eric Verrecchia

Lausanne, 2015

IMPRIMATUR

Vu le rapport présenté par le jury d'examen, composé de

Président de la séance publique :	M. le Professeur Eric Verrecchia
Président du colloque :	M. le Professeur Eric Verrecchia
Directeur de thèse :	M. le Professeur Stefan Schmalholz
Expert interne :	M. le Professeur Yuri Podladchikov
Expert externe :	M. le Professeur Boris Kaus

Le Doyen de la Faculté des géosciences et de l'environnement autorise l'impression de la thèse de

Madame Marina VON TSCHARNER

Titulaire d'un
Master of Science in Earth Science
Ecole Polytechnique Fédérale, Zürich

intitulée

**THREE DIMENSIONAL HYDRODYNAMIC NUMERICAL
MODELLING OF FOLD NAPPE FORMATION, BASEMENT-
COVER DEFORMATION AND SLAB DETACHMENT WITH
APPLICATIONS TO THE HELVETIC NAPPE SYSTEM
(W SWITZERLAND)**

Lausanne, le 16 janvier 2015

Pour le Doyen de la Faculté des géosciences et
de l'environnement



Professeur Eric Verrecchia, Vice-doyen

*When you talk you are only repeating what you know,
but when you listen, you may learn something new.*

Dalai Lama

Table of Contents

Summary	IX
Résumé	XI
Zusammenfassung	XIII
1. Introduction	1
1.1. Geological overview on the Helvetic nappe system	1
1.2. Modelling in geoscience	5
1.2.1. Analogue modelling	5
1.2.2. Computational science, geodynamics and numerical methods	6
1.3. Motivation and open questions	7
1.4. Thesis Organization	12
1.5. Related work	13
References	14
2. A 3-D Lagrangian finite element algorithm with re-meshing for simulating large-strain hydrodynamic instabilities in power-law viscoelastic fluids	20
Short title: 3-D FE algorithm	
2.1. Introduction	21
2.2. Governing equations	23
2.3. Numerical Method	27
2.3.1. Temporal discretisation	27
2.3.2. Spatial discretisation	29
2.3.3. Non-linear solver	30
2.3.4. Interface tracking	30
2.3.5. Re-meshing	33
2.4. Benchmark	34
2.4.1. Viscous inclusion test - convergence test	35

2.4.2.	Re-meshing test	39
2.5.	Simulations	42
2.5.1.	Single-layer viscoelastic folding	42
2.5.2.	Necking during slab detachment	44
2.5.3.	Fold nappe formation	49
2.6.	Discussion	56
2.7.	Conclusions	57
2.8.	Appendix A: Numerical methodology	58
2.9.	Appendix B: Benchmarks	64
2.9.1.	2-D Rayleigh-Taylor instability	65
2.9.2.	2-D folding and necking	66
2.9.3.	3-D single-layer folding	69
2.9.4.	3-D Rayleigh-Taylor instability	71
2.9.5.	Elasticity - elastic beam and elastic simple shear	73
2.9.6.	Viscous inclusion test - convergence test	75
	References	76
3.	Three-dimensional necking during viscous slab detachment	84
	Short title: 3-D necking of detaching slabs	
3.1.	Introduction	85
3.2.	Numerical Model	85
3.3.	Results	89
3.4.	Discussion	95
3.5.	Conclusions	96
	References	97
4.	3-D hydrodynamic modelling applied to fold nappes and the Rawil depression in the Helvetic nappe system (western Switzerland)	101
	Short title: 3-D FE Modelling	
4.1.	Introduction	102
4.2.	Introduction	102
4.3.	Geological background and potential tectonic scenarios	103
4.4.	Numerical Method	108
4.5.	Simulations	109

4.5.1. Fold nappe formation	109
4.5.2. 3-D formation of the Rawil depression	116
4.6. Discussion	125
4.7. Conclusions	127
4.8. Conclusions	127
References	129
5. Discussion	132
References	139
6. Conclusions	141
A. Intersection ellipses	144
A.1. Calculation of intersection ellipses	144
References	148
Acknowledgements	150
Curriculum Vitae	152
Publications and conference presentations	153

Summary

Many three-dimensional (3-D) structures in rock, which formed during the deformation of the Earth's crust and lithosphere, are controlled by a difference in mechanical strength between rock units and are often the result of a geometrical instability. Such structures are, for example, folds, pinch-and-swell structures (due to necking) or cusped-lobate structures (mullions). These structures occur from the centimeter to the kilometer scale and the related deformation processes control the formation of, for example, fold-and-thrust belts and extensional sedimentary basins or the deformation of the basement-cover interface. The 2-D deformation processes causing these structures are relatively well studied, however, several processes during large-strain 3-D deformation are still incompletely understood. One of these 3-D processes is the lateral propagation of these structures, such as fold and cusp propagation in a direction orthogonal to the shortening direction or neck propagation in direction orthogonal to the extension direction. Especially, we are interested in fold nappes which are recumbent folds with amplitudes usually exceeding 10 km and they have been presumably formed by ductile shearing. They often exhibit a constant sense of shearing and a non-linear increase of shear strain towards their overturned limb. The fold axes of the Morcles fold nappe in western Switzerland plunges to the ENE whereas the fold axes in the more eastern Doldenhorn nappe plunges to the WSW. These opposite plunge directions characterize the Rawil depression (Wildstrubel depression). The Morcles nappe is mainly the result of layer parallel contraction and shearing. During the compression the massive limestones were more competent than the surrounding marls and shales, which led to the buckling characteristics of the Morcles nappe, especially in the north-dipping normal limb. The Doldenhorn nappe exhibits only a minor overturned fold limb. There are still no 3-D numerical studies which investigate the fundamental dynamics of the formation of the large-scale 3-D structure including the Morcles and Doldenhorn nappes and the related Rawil depression. We study the 3-D evolution of geometrical instabilities and fold nappe formation with numerical simulations based on the finite element method (FEM). Simulating geometrical instabilities caused by sharp variations of mechanical strength between rock units requires a numerical algorithm that can accurately resolve material interfaces for large differences in material properties (e.g. between limestone and shale) and for large deformations. Therefore, our FE algorithm combines a numerical contour-line technique and a deformable Lagrangian mesh with re-meshing. With this

combined method it is possible to accurately follow the initial material contours with the FE mesh and to accurately resolve the geometrical instabilities. The algorithm can simulate 3-D deformation for a visco-elastic rheology. The viscous rheology is described by a power-law flow law. The code is used to study the 3-D fold nappe formation, the lateral propagation of folding and also the lateral propagation of cusps due to initial half graben geometry. Thereby, the small initial geometrical perturbations for folding and necking are exactly followed by the FE mesh, whereas the initial large perturbation describing a half graben is defined by a contour line intersecting the finite elements. Further, the 3-D algorithm is applied to 3-D viscous necking during slab detachment. The results from various simulations are compared with 2-D results and a 1-D analytical solution.

Résumé

On retrouve beaucoup de structures en 3 dimensions (3-D) dans les roches qui ont pour origines une déformation de la lithosphère terrestre. Ces structures sont par exemple des plis, des boudins (pinch-and-swell) ou des mullions (cusped-lobate) et sont présentés de l'échelle centimétrique à kilométrique. Mécaniquement, ces structures peuvent être expliquées par une différence de résistance entre les différentes unités de roches et sont généralement le fruit d'une instabilité géométrique. Ces différences mécaniques entre les unités contrôlent non seulement les types de structures rencontrées, mais également le type de déformation (thick skin, thin skin) et le style tectonique (bassin d'avant pays, chaîne d'avant pays). Les processus de la déformation en deux dimensions (2-D) formant ces structures sont relativement bien compris. Cependant, lorsque l'on ajoute la troisième dimension, plusieurs processus ne sont pas complètement compris lors de la déformation à large échelle. L'un de ces processus est la propagation latérale des structures, par exemple la propagation de plis ou de mullions dans la direction perpendiculaire à l'axe de compression, ou la propagation des zones d'amincissement des boudins perpendiculairement à la direction d'extension. Nous sommes particulièrement intéressés les nappes de plis qui sont des nappes de charriage en forme de plis couché d'une amplitude plurikilométrique et étant formées par cisaillement ductile. La plupart du temps, elles exposent un sens de cisaillement constant et une augmentation non linéaire de la déformation vers la base du flanc inverse. Un exemple connu de nappes de plis est le domaine Helvétique dans les Alpes de l'ouest. Une de ces nappes est la Nappe de Morcles dont l'axe de pli plonge E-NE tandis que de l'autre côté de la dépression du Rawil (ou dépression du Wildstrubel), la nappe du Doldenhorn (équivalent de la nappe de Morcles) possède un axe de pli plongeant O-SO. La forme particulière de ces nappes est due à l'alternance de couches calcaires mécaniquement résistantes et de couches mécaniquement faibles constituées de schistes et de marnes. Ces différences mécaniques dans les couches permettent d'expliquer les plissements internes à la nappe, particulièrement dans le flanc inverse de la nappe de Morcles. Il faut également noter que le développement du flanc inverse des nappes n'est pas le même des deux côtés de la dépression de Rawil. Ainsi la nappe de Morcles possède un important flanc inverse alors que la nappe du Doldenhorn en est presque dépourvue. A l'heure actuelle, aucune étude numérique en 3-D n'a été menée afin de comprendre la dynamique fondamentale de la formation des nappes de Morcles et du Doldenhorn ainsi que la

formation de la dépression de Rawil. Ce travail propose la première analyse de l'évolution 3-D des instabilités géométriques et de la formation des nappes de plis en utilisant des simulations numériques. Notre modèle est basé sur la méthode des éléments finis (FEM) qui permet de résoudre avec précision les interfaces entre deux matériaux ayant des propriétés mécaniques très différentes (par exemple entre les couches calcaires et les couches marneuses). De plus nous utilisons un maillage lagrangien déformable avec une fonction de re-meshing (production d'un nouveau maillage). Grâce à cette méthode combinée il nous est possible de suivre avec précision les interfaces matérielles et de résoudre avec précision les instabilités géométriques lors de la déformation de matériaux visco-élastiques décrit par une rhéologie non linéaire ($n > 1$). Nous utilisons cet algorithme afin de comprendre la formation des nappes de plis, la propagation latérale du plissement ainsi que la propagation latérale des structures de type mullions causé par une variation latérale de la géométrie (p.ex graben). De plus l'algorithme est utilisé pour comprendre la dynamique 3-D de l'amincissement visqueux et de la rupture de la plaque descendante en zone de subduction. Les résultats obtenus sont comparés à des modèles 2-D et à la solution analytique 1-D.

Zusammenfassung

Viele drei dimensionale (3-D) Strukturen, die in Gesteinen vorkommen und durch die Verformung der Erdkruste und Lithosphäre entstanden sind werden von den unterschiedlichen mechanischen Eigenschaften der Gesteinseinheiten kontrolliert und sind häufig das Resultat von geometrischen Instabilitäten. Zu diesen Strukturen zählen zum Beispiel Falten, Pinch-and-swell Strukturen oder sogenannte Cusate-Lobate Strukturen (auch Mullions). Diese Strukturen kommen in verschiedenen Grössenordnungen vor und können Masse von einigen Zentimeter bis zu einigen Kilometer aufweisen. Die mit der Entstehung dieser Strukturen verbundenen Prozesse kontrollieren die Entstehung von Gebirgen und Sediment-Becken sowie die Verformung des Kontaktes zwischen Grundgebirge und Sedimenten. Die zwei dimensional (2-D) Verformungs-Prozesse die zu den genannten Strukturen führen sind bereits sehr gut untersucht. Einige Prozesse während starker 3-D Verformung sind hingegen noch unvollständig verstanden. Einer dieser 3-D Prozesse ist die seitliche Fortpflanzung der beschriebenen Strukturen, so wie die seitliche Fortpflanzung von Falten und Cusate-Lobate Strukturen senkrecht zur Verkürzungsrichtung und die seitliche Fortpflanzung von Pinch-and-Swell Strukturen orthogonal zur Streckungsrichtung. Insbesondere interessieren wir uns für Faltendecken, liegende Falten mit Amplituden von mehr als 10 km. Faltendecken entstehen vermutlich durch duktile Verscherung. Sie zeigen oft einen konstanten Scherungssinn und eine nicht-lineare Zunahme der Scherverformung am überkippten Schenkel. Die Faltenachsen der Morcles Decke in der Westschweiz fallen Richtung ONO während die Faltenachsen der östlicher gelegenen Doldenhorn Decke gegen WSW einfallen. Diese entgegengesetzten Einfallrichtungen charakterisieren die Rawil Depression (Wildstrubel Depression). Die Morcles Decke ist überwiegend das Resultat von Verkürzung und Scherung parallel zu den Sedimentlagen. Während der Verkürzung verhielt sich der massive Kalkstein kompetenter als der umliegende Mergel und Schiefer, was zur Verfaltung der Morcles Decke führte, vor allem in gegen Norden einfallenden überkippten Schenkel. Die Doldenhorn Decke weist dagegen einen viel kleineren überkippten Schenkel und eine stärkere Lokalisierung der Verformung auf. Bis heute gibt es keine 3-D numerischen Studien, die die fundamentale Dynamik der Entstehung von grossen stark verformten 3-D Strukturen wie den Morcles und Doldenhorn Decken sowie der damit verbundenen Rawil Depression untersuchen. Wir betrachten die 3-D Entwicklung von geometrischen Instabilitäten sowie die Entstehung von Faltendecken mit Hilfe von

numerischen Simulationen basiert auf der Finite Elemente Methode (FEM). Die Simulation von geometrischen Instabilitäten, die aufgrund von Änderungen der Materialeigenschaften zwischen verschiedenen Gesteinseinheiten entstehen, erfordert einen numerischen Algorithmus, der in der Lage ist die Materialgrenzen mit starkem Kontrast der Materialeigenschaften (zum Beispiel zwischen Kalksteineinheiten und Mergel) für starke Verformung genau aufzulösen. Um dem gerecht zu werden kombiniert unser FE Algorithmus eine numerische Contour-Linien-Technik und ein deformierbares Lagranges Netz mit Re-meshing. Mit dieser kombinierten Methode ist es möglich den anfänglichen Materialgrenzen mit dem FE Netz genau zu folgen und die geometrischen Instabilitäten genügend aufzulösen. Der Algorithmus ist in der Lage visko-elastische 3-D Verformung zu rechnen, wobei die viskose Rheologie mit Hilfe eines power-law Fliessgesetzes beschrieben wird. Mit dem numerischen Algorithmus untersuchen wir die Entstehung von 3-D Faltendecken, die seitliche Fortpflanzung der Faltung sowie der Cusbate-Lobate Strukturen die sich durch die Verkürzung eines mit Sediment gefüllten Halbgrabens bilden. Dabei werden die anfänglichen geometrischen Instabilitäten der Faltung exakt mit dem FE Netz aufgelöst während die Materialgranzes des Halbgrabens die Finiten Elemente durchschneidet. Desweiteren wird der 3-D Algorithmus auf die Einschnürung während der 3-D viskosen Plattenablösung und Subduktion angewandt. Die 3-D Resultate werden mit 2-D Ergebnissen und einer 1-D analytischen Lösung verglichen.

1 Introduction

Generally, the presented thesis consists of two parts. In the first part the focus lies on the implementation and the technical details of the numerical algorithm. The numerical algorithm is realized in Matlab (TheMathWorks) and is developed to study 3-D large strain evolution of hydrodynamic instabilities, such as folding and necking with a power-law visco-elastic rheology. In the second part of the presented thesis the numerical algorithm is applied to different processes in geoscience. Once the algorithm is applied to viscous necking during slab detachment using a significantly simplified model configuration to identify and quantify the first order 3-D deformation processes during slab detachment. In contrast, the numerical algorithm is used to study the effect of initially laterally varying geometry on folding and basement-cover deformation during the compression of a sediment filled half graben. These simulations are applied to the formation of the Morcles and Doldenhorn nappes in western Switzerland. For the third application of the algorithm to the formation of the Rawil depression in the Helvetic nappe system in western Switzerland we use a simple model configuration to study the first order impact of an oblique graben (representing a weak zone) on the updoming of the basement during shortening and perpendicular extension. Therefore, these simulations combine folding with perpendicular necking.

1.1. Geological overview on the Helvetic nappe system

The study area is located at the border between the canton of Bern and Vallais in the Swiss Alps. In this region the Helvetic nappesystem is made up of different nappes which lie on top of each other. The lowermost nappes in the Helvetic nappe stack are autochthonous and paraautochthonous. In the western part of the study area this lowermost nappe is the Morcles nappe whereas in the eastern part it is the Doldenhorn nappe. On top of the Morcles nappe in the west follow the Diablerets nappe, the Mt. Gond nappe and the Sublage nappe. The eastern equivalents are the Jägerchrüz nappe, the Gellihorn nappe and the Wildhorn nappe. Figure 1.1 shows two cross sections through the Helvetic nappe stack in the Western Swiss Alps and a 3-D block dia-

gram of the geometry around the Rawil depression. The cross section through the western part of the study area showing the Morcles nappe and the overlying Diablerets nappe, Mt. Gond nappe and the Sublage nappe was reproduced after Escher *et al.* (1993) (Fig. 1.1a). The cross section through the area on the east side of the Rawil depression displaying the Doldenhorn nappe as well as the overlying Jägerchrüz nappe, Gellihorn nappe and Wildhorn nappe was reproduced after Kirschner *et al.* (1999) (Fig. 1.1b) and the block diagram showing the 3-D geometry around the Rawil depression was reproduced after Ramsay (1981) (Fig. 1.1c). The Helvetic nappes consist of sediments which are generally a repetition of limestones, marls, shales and sandstones. These sediments were deposited from late Triassic to Early Oligocene at the European margin north of the Valais domain (Furrer, 1938; Ramsay, 1989; Escher *et al.*, 1993; Pfiffner, 1993). After the last sedimentation the Helvetic nappes were formed due to compression by folding and overthrusting. The Morcles nappe represents a typical fold nappe with a prominent overturned limb (Fig. 4.1a). Fold nappes are recumbent folds with amplitudes usually exceeding 10 km, and they have been formed presumably by ductile shearing (Bauville *et al.*, 2013; Dietrich and Casey, 1989; Epard and Escher, 1996; Ramsay *et al.*, 1983). Fold nappes often exhibit a constant sense of shearing and a non-linear increase of shear strain from their normal to their overturned limb which has been observed across the Morcles nappe (Ramsay, 1981). The Morcles fold nappe and the Doldenhorn nappe are mainly the result of layer parallel compression and shearing (Ramsay, 1981). During this compression the massive limestone were more competent than the surrounding marls and shales. This led to the buckling characteristics of the Morcles nappe, especially in the north-dipping normal limb (Fig. 1.1a). The Doldenhorn nappe shows only a minor overturned fold limb and significantly more localized deformation at its base (Steck *et al.*, 1999). A possible explanation for this higher deformation at the base of the Doldenhorn nappe is that the weak basal sediments in the half graben forming now the Doldenhorn nappe have been thinner than the sediments of the Morcles nappe (Pfiffner, 2011).

The Morcles nappe is geologically separated from the Doldenhorn nappe by the Rawil depression (Fig. 1.1c). The Rawil or Wildstrubel depression is characterized by an opposite plunge of the fold axis in the Helvetic nappe stack and was first described by Argand (1902-1911) and Heim (1921). The fold axis of the Morcles nappe in the west of the Rawil depression plunges to the ENE whereas the fold axis of the Doldenhorn nappe plunges to the WSW.

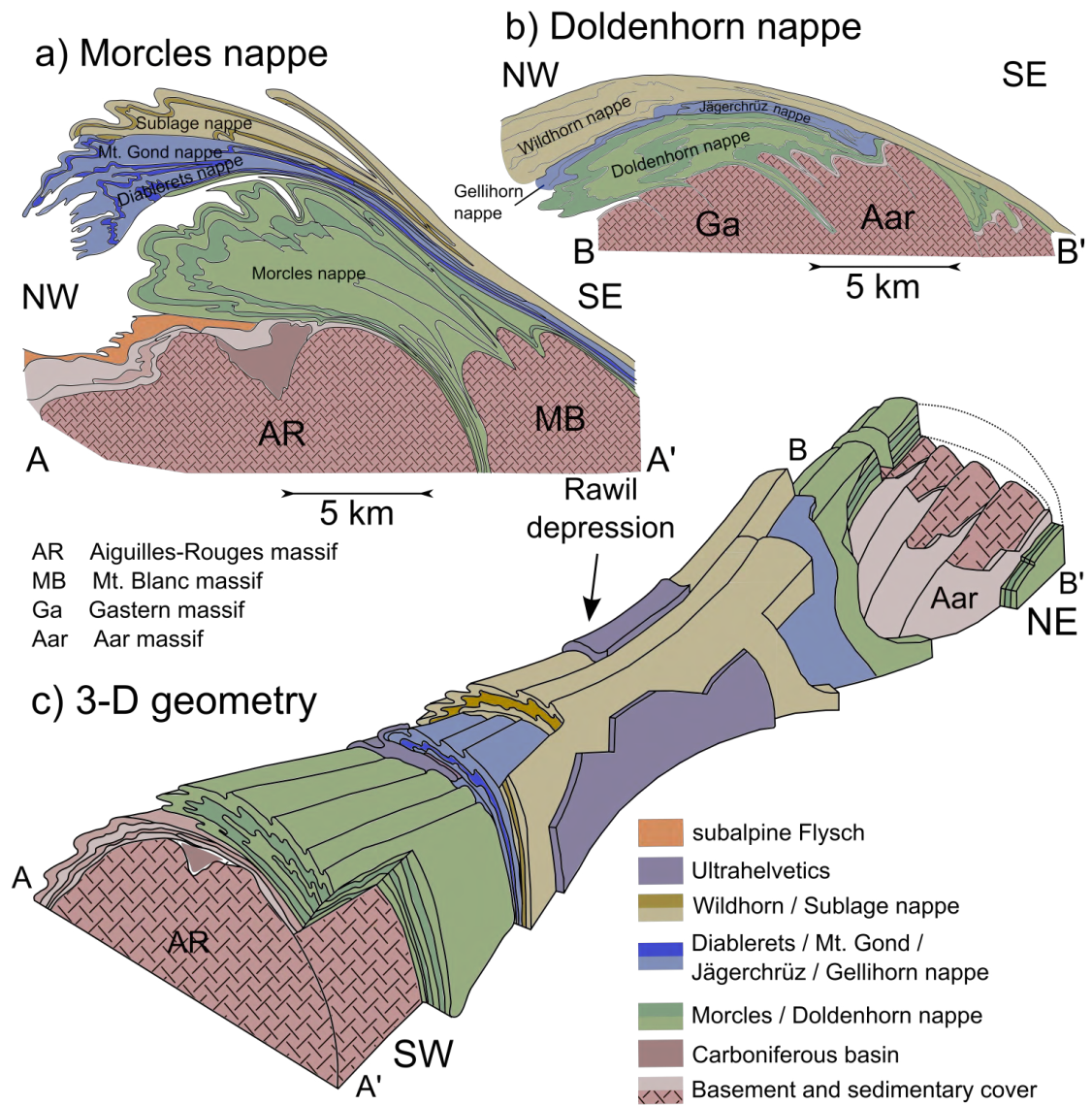


Figure 1.1: a) Cross section in the western part showing the Morcles nappe as well as the overlying Diablerets nappe, Mt. Gond nappe and Sublage nappe (reproduced after Escher et al., 1993). b) Cross section in the eastern part of the study area shows the Doldenhorn nappe as well as the overlying Diablerets nappe and Wildorn nappe (reproduced after Kirschner et al., 1999). c) Schematic 3-D geometry of the axial Rawil depression between the Morcles nappe in the west and the Doldenhorn nappe in the east (reproduced after Ramsay, 1981).

Figure 1.2 shows the isohypses of the crystalline basement in the region of the Central Alps (Pfiffner, 2009). The Rawil depression separates the Aiguilles Rouges and Mt. Blanc massifs in the west for the Aar and Gotthard massifs in the east. The amplitude of the crystalline massif culminations reaches up to 5 km. The two pairs of basement massifs are arranged en échelon (Dietrich, 1989; Pfiffner *et al.*, 1997; Pfiffner, 2009).

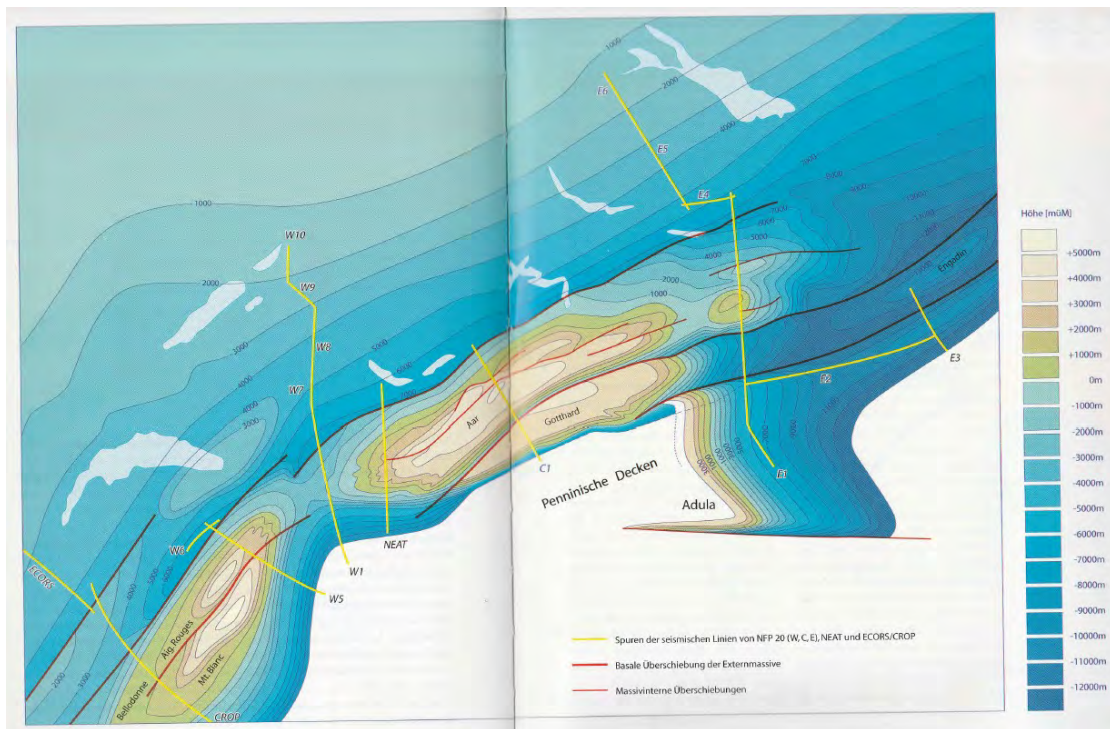


Figure 1.2: Isohyps of the crystalline basement topography in the region of the Central Alps showing the Aiguilles Rouges / Mt. Blanc and Aar massif culminations as well as the Rawil depression. From Pfiffner, 2009.

Due to continuous compression the Helvetic nappe stack was folded and updomed after the nappe stacking (Lugeon, 1914-1918; Masson *et al.*, 1980; Ramsay, 1981; Ramsay *et al.*, 1983; Burkhard, 1988; Ramsay, 1989; Herwegh and Pfiffner, 2005) which led to the exhumation of the external massifs. In the Rawil depression the Helvetic nappe stack is overprinted by a dextral transtension zone (Lugeon, 1914-1918; Ramsay *et al.*, 1983; Ramsay, 1989; Burkhard, 1988; Dietrich, 1989; Gasser and Mancktelow, 2010). In the deepest part of the depression, where the highest nappes of the Helvetic nappe stack are preserved, oblique normal faults with significant

displacement are observed (Gasser and Mancktelow, 2010). In this area ductile folding led to the axial depression as well as the dipping of the fold nappe axis and brittle faulting led to the normal faults. This documents the evolution from ductile to brittle deformation during the exhumation and cooling. The normal faults in the Rawil depression suggest that there is orogen parallel extension whereas the exhumation of the external massifs took place due to orogen perpendicular compression.

The Rawil depression has been explained with different tectonic scenarios. For example, according to Burkhard (1988) the Aiguilles Rouges massif and the Aar massif were updomed and exhumed on oblique thrusts in the underlying basement. The Rawil depression formed due to a dextral offset in the thrust plane in the crystalline basement. In contrast, Dietrich (1989) and Ramsay (1989) suggested that the Rawil depression formed due to changing thrusting directions. The change in thrusting direction from top to the N to top to the W in the early to late stages of the Alpine collision led to significant fold axis parallel extension and the formation of the axial Rawil depression as well as the culmination of the Aiguilles Rouges and Aar massifs.

1.2. Modelling in geoscience

1.2.1. Analogue modelling

Dynamic modelling in geoscience started with analogue models in the early 19th century. Probably the first analogue model was presented by Sir James Hall who modeled folds which are observed in geological strata (Hall, 1815). In the first experiment he used different pieces of cloth of different fabric (e.g. linen and wool) to model the geological layers. The layers were loaded with a flat door and two other boards were applied to the sides. These two boards on the sides were then forced towards each other to generate layer parallel shortening and folding in the cloth layers. Another experiment was built using beds of clay in a box. The layers were then subjected to compression with movable ends which were driven by screw jacks. This is basically the same model configuration which is used today for fold and thrust experiments. After these pioneering experiments several other modellers followed and used analogue experiments to study fractures, thrusts, folds, pinch-and-swell structures, boudins and salt domes (Daubree, 1878; Favre, 1878; Cadell, 1890; Willis, 1893; Escher and Kuenen, 1929; Ramberg, 1955). The

analogue models became a quantitative technique when Hubbert (1937) provided a well-founded scaling theory. In the 1980's realistic models were built using different types of materials (viscous and brittle) to simulate crustal and lithosphere scale processes (Faugere and Brun, 1984; Davy and Cobbold, 1988).

One of the limitations of analogue models is the reproducibility and the elaborateness. Further, it is difficult to measure the deformation, deformation rates and stresses in 3-D.

1.2.2. Computational science, geodynamics and numerical methods

The development of the theory of numerical methods and techniques which were designed by mathematicians (numerical mathematics) is closely related to the development of computers itself. The use of mathematics in the field of geodynamics started with simple analytical models to explain the first order behaviour of the Earth as well as plate tectonics. In order to get more realistic models scientists started to develop numerical simulations. The first 2-D model for a downgoing slab was presented in 1970 (Minear and Toksoz, 1970). Other 2-D models, developed to simulate mantle convection, salt domes and continental collision followed (Torrance and Turcotte, 1971; Berner *et al.*, 1972; Woitdt, 1978; Daigneres *et al.*, 1978; Bird, 1978). Since then, there was a large improvement of computational power and numerical methods. The first 3-D models were designed for mantle convection in the 80's (Baumgardner, 1985; Houseman, 1988). The numerical modelling community in geodynamics has been improving very rapidly and various numerical techniques have been presented for various applications. These studies include 2-D models (Weinberg and Schmeling, 1992; Fullsack, 1995; van Keken *et al.*, 1997; Schmalholz *et al.*, 2001; Babeyko *et al.*, 2002; Gerya and Yuen, 2003; Moresi *et al.*, 2003; Gerya and Yuen, 2007) as well as a few studies using 3-D models (Kaus and Podlatchikov, 2001; Kaus and Schmalholz, 2006; Moresi *et al.*, 2007; Popov and Sobolev, 2008; Lechmann *et al.*, 2011; Thieulot, 2011; Grasemann and Schmalholz, 2012). Recently, two books came out about numerical modelling in geodynamics (Gerya, 2010; Ismail-Zadeh and Tackley, 2010).

In this thesis we use the Finite Element (FE) Method to simulate large strain deformation of power-law visco-elastic material. The finite element (FE) method is a numerical technique to solve partial differential equations. The first Book dealing with the finite element method was

published in 1967 (Zienkewicz and Cheung, 1967). The research and field of applications expanded and therefore many developments occurred since then. The finite element (FE) method is based on continuum mechanics which deals with the motion of materials which are modeled as continuous mass, i.e. materials which fill the space continuously. The concepts of continuum mechanics is highly suited to model geological processes because geo-materials can often be approximated by fluids with certain material properties (Turcotte and Schubert, 2002). The motion of the deformable materials is described by basic physical equations as the conservation of mass, the conservation of linear momentum (i.e. force balance), the conservation of angular momentum, the conservation of energy and the rheological equations (i.e. constitutive equations). The rheological equations describe the behaviour of the material under a certain stress and therefore for example relate the stress with the strain rate. The mentioned equations provide a closed system of equations which means that there are as many equations as unknown variables (i.e. velocity, pressure, temperature,...).

1.3. Motivation and open questions

There exist a few tectonic models for the formation of fold nappes (e.g. Ramsay *et al.* (1983) or Gillcrist *et al.* (1987)). Ramsay *et al.* (1983) presented a model where the movement of each Helvetic nappe between its roof thrust and its basal floor thrust led to the simple shear deformation within the fold nappes (Fig. 1.3). According to them the nappes formed during the overthrusting on thrust ramps (Fig. 1.3a). During the simple shear deformation competent rock units which are oblique to the shearing are compressed and folded, especially in the frontal part of the nappes (Fig. 1.3b and c). The amount of simple shear deformation increases towards the base of the fold nappe where the layers become intensively elongated and thinned.

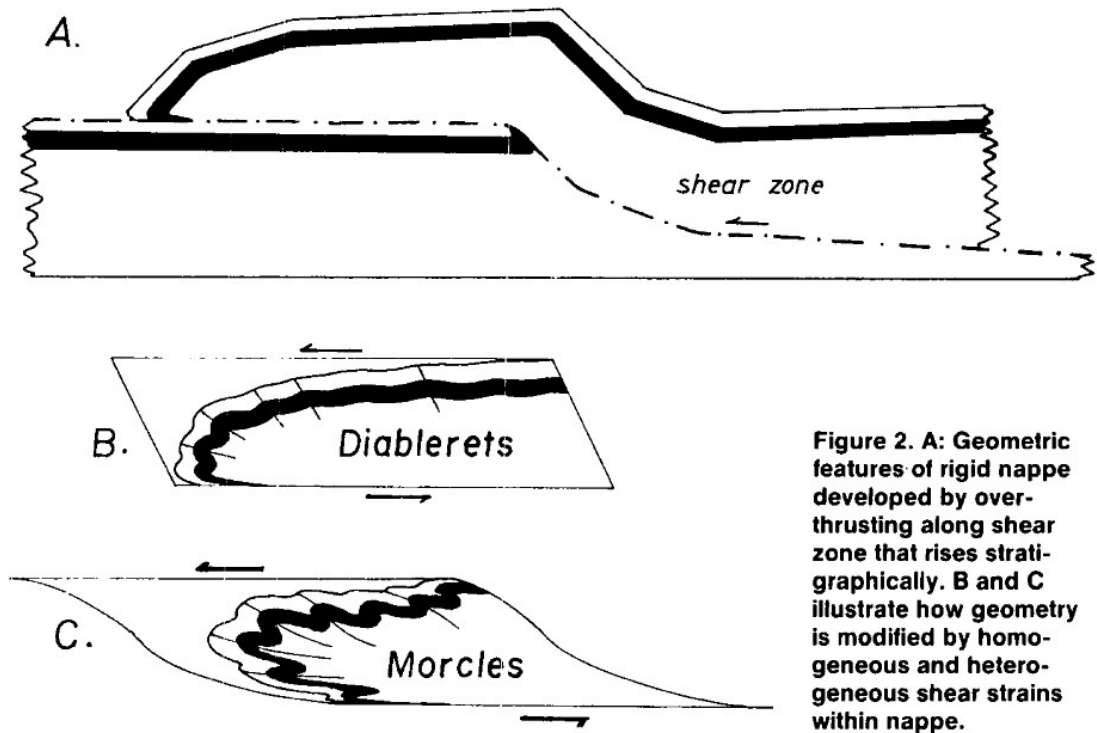


Figure 2. A: Geometric features of rigid nappe developed by overthrusting along shear zone that rises stratigraphically. **B and C** illustrate how geometry is modified by homogeneous and heterogeneous shear strains within nappe.

Figure 1.3: Model for the formation of the Morcles and Diablerets fold nappes presented by Ramsay et al. (1983).

Based on this model by Ramsay *et al.* (1983) Dietrich and Casey (1989) presented a tectonic model using large and small scale geometrical information of the Helvetic nappes. They used accurate profiles as well as the strain states and the metamorphism of the nappes. The model presented for the Diablerets nappe is based on the finite element method and uses a combination of simple shear and pure shear. The initial model configuration consists of an oblique layer of Urganian limestone in a shear zone. The results obtained by Dietrich and Casey (1989) are shown in figure 1.4.

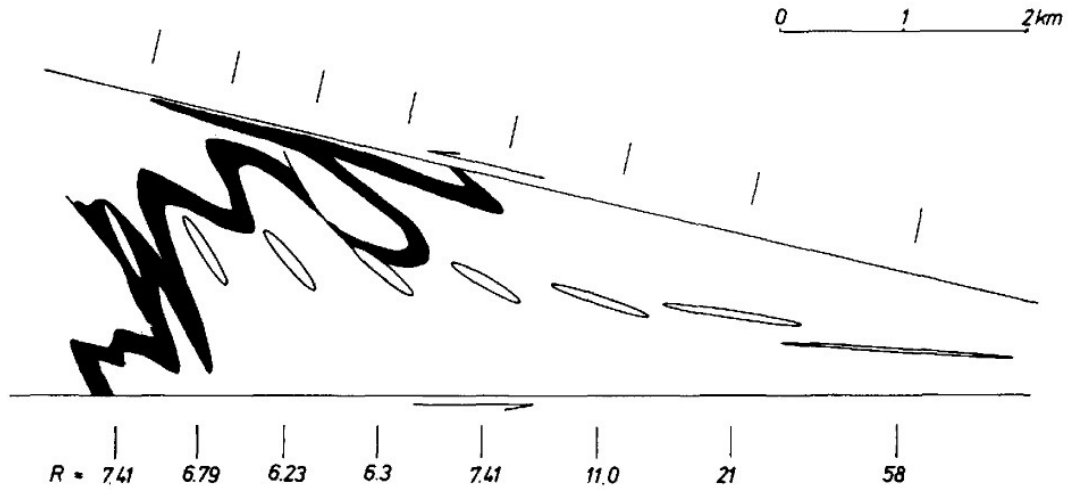


Figure 1.4: Model for the formation of the Diablerets nappe presented by Dietrich and Casey (1989).

Another model presented by Gillcrisp *et al.* (1987) describes the formation of the Helvetic fold nappes as basin inversions where sediment filled half grabens are compressed. Figure 1.5 shows a schematic sketch of the basement where first a graben is formed due to extension and after the basement is folded and overthrust due to compression.

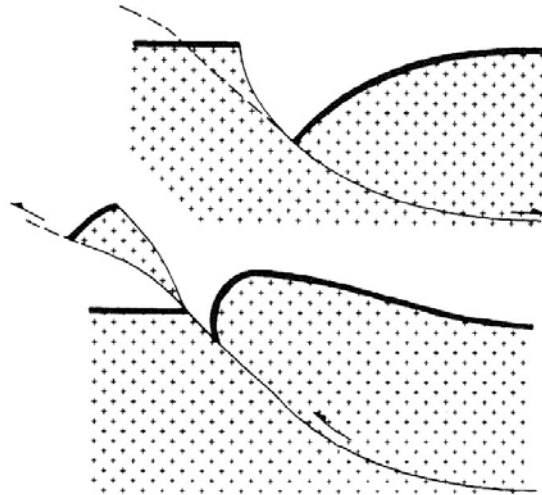


Figure 1.5: Basin inversion model presented by Gillcrisp *et al.* (1987).

Figure 1.6 shows the evolution of the Morcles nappe suggested by Gillcrist *et al.* (1987). The half graben is filled with Jurassic to Cretaceous sediments. The competent sedimentary layers are folded and sheared over the basement due to overall compression (Fig. 1.6b). Further shortening and the development of a thrust emplaced the fold on the Aiguilles-Rouges massif (Fig 1.6c).

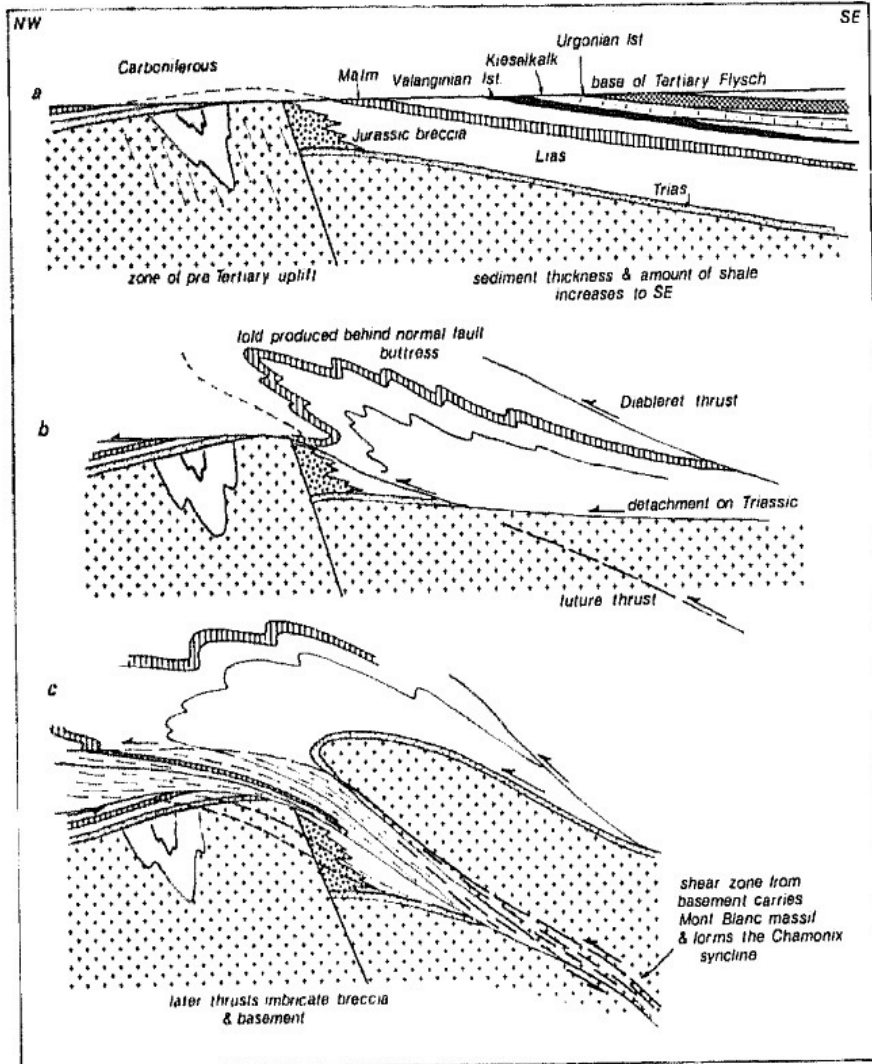


Figure 1.6: Evolution of the Morcles fold nappe suggested by Gillcrist *et al.* (1987). a) Geometry before thrust deformation. b) and c) Stages of thrust inversion.

The geometry and structures around the Rawil depression are well documented and described in detail (Argand, 1902-1911; Heim, 1921; Ramsay, 1981, 1989; Gasser and Mancktelow, 2010; Cardello, 2013). There are also few conceptual and kinematic models (e.g. Burkhard (1988)). The model presented by Burkhard (1988) assumes a curved thrust ramp in the basement which led to the the depression in the overthrust Helvetic nappes (Fig. 1.7). In contrast, Dietrich (1989) and Ramsay (1989) suggested that the Rawil depression formed due to changing thrusting directions. The change in thrusting direction from top to the N to top to the W in the early to late stages of the Alpine collision led to significant fold axis parallel extension and the formation of the axial Rawil depression as well as the culmination of the Aiguilles Rouges and Aar massifs.

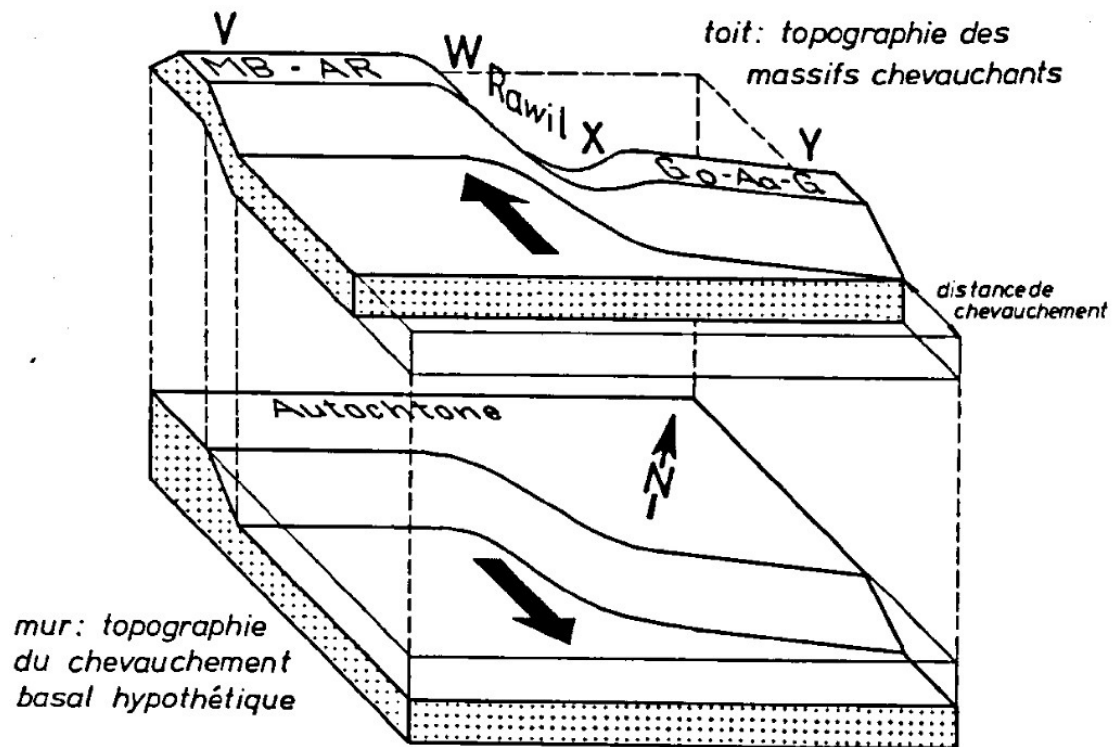


Figure 1.7: Model for the Rawil depression presented by Burkhard (1988). In order to have a good overview the upper part is lifted to see the structure of the basement below. The model assumes a curved thrust ramp in the basement which led to the depression in the basement and the Helvetic nappes above.

However, there are still no 3-D numerical studies which investigate the fundamental dynamics of the formation of the large-scale 3-D structure including the Morcles and Doldenhorn nappes

and the related Rawil depression. Such studies require a numerical algorithm that can accurately track material interfaces for large differences in material properties (e.g. between limestone and shale) and for large deformations. Further, the numerical algorithm should be able to accurately resolve geometrical instabilities, especially at the beginning of the deformation.

1.4. Thesis Organization

We use the Finite Element (FE) Method to simulate large strain deformation of power-law viscoelastic material. The simulations are applied to the formation of tectonic fold nappes as the Morcles and Doldenhorn nappe and the later formation of the Rawil depression as well as the simulation of 3-D necking during viscous slab detachment.

The numerical algorithm is described in chapter 2 which was submitted to Geochemistry, Geophysics, Geosystems. The 3-D algorithm PINK-3D is realized in Matlab (TheMathWorks) and a large part of it was written during this doctoral thesis. We present the numerical algorithm based on the finite element method (FEM) and apply it to investigate the 3-D large strain evolution of hydrodynamic instabilities, such as folding and necking. Simulating these instabilities, that are caused by sharp contrasts in mechanical strength, requires a numerical algorithm that can accurately resolve the initial low-amplitude material interfaces between model units with different strength (e.g. representing limestone and shale), and that can also accurately follow these interfaces during large strain deformation. Therefore, our FE code PINK-3D combines a deformable Lagrangian mesh with a contour-line technique in 3-D (i.e. material interfaces) and re-meshing. The algorithm is designed to simulate continuous 3-D deformation and employs a power-law viscoelastic rheology. The 3-D FE code is tested with various analytical solutions for the low-amplitude growth rates of folding, necking and Rayleigh-Taylor instabilities, and for stress fields around circular inclusions. The code is further applied to 3-D viscoelastic folding, to power-law viscous necking during slab detachment and to fold nappe formation with laterally varying initial geometry.

In chapter 3 we show the results of a few simulations of viscous necking during 3-D slab detachment, one of them with laterally varying initial geometry and compare the results with the 1-D analytical solution as well as with 2-D numerical results (Schmalholz, 2011). This chapter was written in collaboration with Thibault Duretz and is published in Geophysical Research Letters

(von Tscharnner *et al.*, 2014). Here, we study an idealized slab detachment configuration that focuses on the necking instability of lithospheric plates subjected to gravity. This study builds upon the 1-D and 2-D studies of Schmalholz (2011) and Duretz *et al.* (2012). Our aim is to better understand the deformation patterns that arise during purely mechanical 3-D necking, and to quantify the 3-D necking during slab detachment.

In the last chapter 4 we apply the 3-D algorithm PINK-3D to the formation of fold nappes and to the formation of the Rawil depression. Simulating fold nappes, we go into the today's geometrical and structural differences between the Morcles nappe in the western part of the study area and the more eastern Doldenhorn nappe. The differences are explained with the different thickness of the weak basal sediments deposited in the half grabens forming now the Morcles and Doldenhorn nappes. The formation of the Rawil depression which is believed to take place after the formation of the Helvetic nappe system is simulated using another model configuration which consist of orogen parallel extension and orogen perpendicular compression. The orogen perpendicular compression leads to the updoming of the external massifs whereas the orogen parallel extension leads to the formation of the axial Rawil depression. During the formation of the Rawil depression a graben which initially cuts through the basement acts as a weak zone.

1.5. Related work

This thesis is part of a research project on the formation of fold nappes and the related Rawil depression in Western Switzerland. The aims of this research project are to improve the understanding of (1) the dynamics of fold nappes in general and (2) the tectonic evolution of the fold nappes in the Western Swiss Alps. As a part of this research project Bauville *et al.* (2013) presented a one dimensional thermo-mechanical shear zone model applied to the Morcles fold nappe. The one dimensional shear zone model which considers a dislocation creep flow law with temperature dependent viscosity is further applied to several kilometer-scale shear zones worldwide in Bauville and Schmalholz (2013).

References

- Argand E., 1902-1911: **Coupes géologiques des Alpes occidentales.**, Matériaux pour la Carte Géologique de la Suisse n.s. 31
- Babeyko A., Sobolev S., Trumbull R., Oncken O. and Lavier L., 2002: **Numerical models of crustal scale convection and partial melting beneath the Altiplano-Puna plateau**, Earth Planetary Science Letters 199
- Baumgardner J., 1985: **Three-dimensional treatment of convective flow in the Earth's mantle**, Journal of Statistical Physics 39, 501–511
- Bauville A. and Schmalholz S., 2013: **Thermo-mechanical model for the finite strain gradient in kilometer-scale shear zones**, g 41, 567–570
- Bauville A., Epard J.-L. and Schmalholz S., 2013: **A simple thermo-mechanical shear model applied to the Morcles fold nappe (Western Alps)**, tectono 583, 76–87
- Berner H., Ramberg H. and Stephanson O., 1972: **Diapirism in theory and experiment**, Tectonophysics 15, 307–336
- Bird P., 1978: **Finite elements modelling of lithosphere deformation: The Zagros collision orogeny**, Tectonophysics 50, 307–336
- Burkhard M., 1988: **L'Helétique de la bordure occidentale du massif de l'Aar (évolution tectonique et métamorphique)**, Eclogae Geologicae Helveticae 81, 63–114
- Cadell H., 1890: **Experimental researches in mountain building**, Trans. Roy. Soc. Edinburgh 35
- Cardello G., 2013: **The Rawil depression**, Diss., ETH zurich, Nr. 21176
- Daigneres M., Fremond M. and Friaa A., 1978: **Modele de type Norton-Hoff generalise pour l'étude des déformations lithosphériques (exemple: la collision Himalayenne)**, Comptes Reudes Hébdomadaires des Seances de l'academie de Sciences 268B
- Daubree A., 1878: **Recherches expérimentales sur les cassures qui traversent l'écorce terrestre particulièrement celles qui sont connues sous les noms de joints et de failles**, Comptes rendus des séances de l'Académie des sciences 86

- Davy P. and Cobbold P., 1988: **Indentation tectonics in nature and experiments. 1. Experiments scaled for gravity**, Bull. Geol. Inst. Univ. Uppsala 14, 129–141
- Dietrich D., 1989: **Fold-axis parallel extension in an accurate fold-and-thrust belt: the case of the Helvetic nappes**, Tectonophysics 170, 183–212
- Dietrich D. and Casey M., 1989: **A new tectonic model for the Helvetic nappes**, Alpine Tectonics, Geological Society Special Publication 54, 47–63
- Duretz T., Schmalholz S. M. and Gerya T. V., 2012: **Dynamics of slab detachment**, Geochemistry Geophysics Geosystems 13, 17PP, doi:10.1029/2011GC004024
- Epard J.-L. and Escher A., 1996: **Transition from basement to cover: a geometric model**, Journal of Structural Geology 18, 333–548
- Escher A., Masson H. and Steck A., 1993: **Nappe geometry in the Western Swiss Alps**, Journal of Structural Geology 15, 501–509
- Escher B. and Kuenen P., 1929: **Experiments in connection with salt domes**, Leidsche Geologische Mededeelingen 3, 151–182
- Faugere E. and Brun J., 1984: **Modélisation expérimentale de la distension continentale**, Comptes-Rendus de l'Académie des Sciences pages 365–370
- Favre A., 1878: **Experiences sur les effets des refoulements ou écrasements lateraux en geologie**, Archives des sciences physiques et naturelles
- Fullsack P., 1995: **An arbitrary Lagrangian-Eulerian formulation for creeping flows and its application in tectonic models**, Geophys. J. Int. 120, 1–23
- Furrer H., 1938: **Geologische Untersuchungen in der Wildstrubelgruppe, Berner Oberland**, Mitt. Natf. Ges. Bern pages 35–177
- Gasser D. and Mancktelow N., 2010: **Brittle faulting in the Rawil depression: field observations from the Rezli fault zones, Helvetic nappes, Western Switzerland**, Swiss Journal of Geoscience 103, 15–32
- Gerya T., 2010: **Introduction to Numerical Geodynamic Modelling**, Cambridge University Press

- Gerya T. and Yuen D., 2003: **Characteristics-based marker-in-cell method with conservative finite-differences schemes for modeling geological flows with strongly variable transport properties**, *Physics of the Earth and Planetary Interiors* 140, 293–318
- Gerya T. and Yuen D., 2007: **Robust characteristics method for modelling multiphase visco-elasto-plastic thermo-mechanical problems**, *Physics of the Earth and Planetary Interiors* 163, 83–105
- Gillcrist R., Coward M. and Mugnier J.-L., 1987: **Structural inversion and its controls: examples from the Alpine foreland and the French Alps**, *Geodinamica Acta* (Paris) pages 5–34
- Grasemann B. and Schmalholz S. M., 2012: **Lateral fold growth and fold linkage**, *Geology* 40, 1039–1042
- Hall J., 1815: **On the revolutions of the Earth's surface**, *Transactions of the Royal Society of Edinburgh* 7, 139–212
- Heim A., 1921: **Geologie der Schweiz, Band II**, Tauchnitz Verlag Gmbh, Leipzig
- Herwegh M. and Pfiffner O., 2005: **Tectono-metamorphic evolution of nappe stack: A case study of the Swiss Alps.**, *Tectonophysics* 404, 55–76
- Houseman G., 1988: **The dependence of convection planform on mode of heating**, *Nature* 332, 346–349
- Hubbert M., 1937: **Theory of Scale Models as Applied to the Study of Geological Structures**, *Geological Society of America Bulletin* 48, 1459–1520
- Ismail-Zadeh A. and Tackley P., 2010: **Computational Methods for Geodynamics**, *Mathematical Geosciences*, Cambridge University Press
- Kaus B. and Podlatchikov Y., 2001: **Forward and Reverse Modeling of the Three-Dimensional Viscous Rayleigh-Taylor Instability**, *Geophysical Research Letters* 28, 11095–098
- Kaus B. and Schmalholz S., 2006: **3D finite amplitude folding: Implications for stress evolution during crustal and lithospheric deformation**, *Geophysical Research Letters* 33

- Kirschner D., Masson H. and Sharp Z., 1999: **Fluid migration through thrust faults in the Helvetic nappes (Western Swiss Alps)**, Contributions to Mineralogy and Petrology 136, 169–183
- Lechmann S., May D., Kaus B. and Schmalholz S., 2011: **Comparing thin-sheet models with 3-D multilayer models for continental collision**, Geophys. J. Int. 187, 10–33
- Lugeon M., 1914-1918: **Les Hautes calcaires entre la Lizerne et la Kandern: Wildhorn, Wildstrubel, Balmhorn et Torrenthorn: explication de la carte spéciale no. 60**, Matériaux pour la carte géologique de la Suisse. Nouvelle série 60
- Masson H., Herb R. and Steck A., 1980: **Helvetic Alps of Western Switzerland**, Geology of Switzerland, A Guide Book. Part B. Birkhaeuserverlag, Basel. pages 109–153
- Minear J. and Toksoz M., 1970: **Thermal regime of a downgoing slab and new global tectonics**, Journal of Geophysical Research 75, 1397–1419
- Moresi L., Dufour F. and Mühlhaus H.-B., 2003: **A Lagrangian integration point finite element method for large deformation modeling of viscoelastic geomaterials**, J. Comput. Phys. 184, 476–497
- Moresi L., Quenette S., Lemiale V., Meriaux C., Appelbe B. and Mühlhaus H.-B., 2007: **Computational approaches to studying non-linear dynamics of the crust and mantle**, Physics of the Earth and Planetary Interiors 163, 69–82
- Pfiffner A., 2009: **Geologie der Alpen**, Bern/Stuttgart/Wien:Haupt Verlag
- Pfiffner A., Lehner P., Heitzmann P., Mueller S. and Steck A., 1997: **Deep structure of the Swiss Alps: Results of NRP 20**, Birkhäuser Verlag, Basel, Boston, Berlin
- Pfiffner O., 1993: **The structure of the Helvetic nappes and its relation to the mechanical stratigraphy**, Journal of Structural Geology 15, 511–521
- Pfiffner O., 2011: **Structural Map of the Helvetic Zone of the Swiss Alps, including Vorarlberg (Austria) and Haute Savoie (France), 1:100000**, Geological Special Map 128. Explanatory notes.
- Popov A. and Sobolev S., 2008: **SLIM3D: A tool for three-dimensional thermomechanical modeling of lithospheric deformation with elasto-visco-plastic rheology**, Physics of the Earth and Planetary Interiors 171, 55–75

- Ramberg H., 1955: **Natural and experimental boudinage and pinch-and-swell structures**, *Journal of Geology* 63, 512–526
- Ramsay J. G., 1981: **Tectonics of the Helvetic Nappes**, Geological Society, London, Special Publications 9, 293–309
- Ramsay J. G., 1989: **Fold and fault geometry in the western Helvetic nappes of Switzerland and France and its implication for the evolution of the arc of the Western Alps**, Geological Society, London, Special Publications 45, 33–45
- Ramsay J. G., Casey M. and Kligfield R., 1983: **Role of shear in development of the Helvetic fold-thrust belt of Switzerland**, *Geology* 11, 439–442
- Schmalholz S. M., 2011: **A simple analytical solution for slab detachment**, *Earth Planetary Science Letters* 304, 45–54
- Schmalholz S. M., Podladchikov Y. Y. and Schmid D., 2001: **A spectral/finite difference method for simulating large deformations of heterogeneous, viscoelastic materials**, *Geophys. J. Int.* 145, 199–208
- Steck A., Bigioggero B., Piaz G. D., Escher A., Martinotti G. and Masson H., 1999: **Carte tectonique des Alpes de Suisse occidentale et des regions avoisinantes, 1:100000**, Carte geologique speciale n 123, Swiss National Hydrological and Geological Survey
- Thieulot C., 2011: **FANTOM: Two- and three-dimensional numerical modelling of creeping flows for the solution of geological problems**, *Physics of the Earth and Planetary Interiors* 188, 47–68
- Torrance K. and Turcotte D., 1971: **Thermal convection with large viscosity variations**, *J. Fluid Mech* 47, 113–125
- Turcotte D. and Schubert G., 2002: **Geodynamics**, Cambridge University Press, Cambridge
- van Keken P., S.D K., Schmeling H., Christensen U., Neumeister D. and Doin M.-P., 1997: **A comparison of methods for the modeling of thermomechanical convection**, *Journal of Geophysical Research* 102, 22477–22495
- von Tscharner M., Schmalholz S. and Duretz T., 2014: **Three-dimensional necking during viscous slab detachment**, *Geophysical Research Letters* 41, 4194–4200

Weinberg R. and Schmeling H., 1992: **Polydiapirs: Multiwavelength gravity structures**, Journal of Structural Geology 14, 425–436

Willis B., 1893: **Mechanisms of Appalachian structure**, U.S. Geol. Survey Ann. Rept. 13

Woidt W., 1978: **Finite element calculations applied to salt dome analysis**, Tectonophysics 50, 369–386

Zienkewicz O. C. and Cheung Y., 1967: **The Finite Element Method in Structural and Continuum Mechanics**, London, New York McGraw-Hill

2 A 3-D Lagrangian finite element algorithm with re-meshing for simulating large-strain hydrodynamic instabilities in power-law viscoelastic fluids

Abstract

We present a three-dimensional (3-D) numerical algorithm (PINK-3D) that is based on the finite element method. The algorithm is designed to simulate hydrodynamic instabilities in power-law viscoelastic fluids under gravity. These instabilities are caused by large and sharp contrasts in mechanical strength and/or density between different materials (e.g. folding, necking or Rayleigh-Taylor diapirism). The instabilities are controlled by the geometry of the material interfaces and the related intra-layer stress distribution when amplitudes of the material interfaces are still low. The presented algorithm combines a deformable Lagrangian mesh with re-meshing in order to accurately simulate the low-amplitude stages of the emerging instabilities, and also to simulate the large strain evolution of the structures emerging from these instabilities. The re-meshing is based on material interfaces that accurately track the boundaries between materials with strongly varying material properties (e.g. effective viscosity or power-law stress exponent). We describe here the main technical details of the 3-D algorithm. The accuracy of the 3-D algorithm is demonstrated with comparisons between the numerical results and 2-D and 3-D analytical solutions for folding, necking, Rayleigh-Taylor diapirism and circular inclusions in viscous medium. We also benchmark the 3-D algorithm with results of a different 2-D finite element algorithm to test the accuracy of the large strain results with re-meshing. Furthermore, two tests are presented that show the accuracy of the viscoelasticity implementation. PINK-3D is also used to study 3-D necking applied to lithospheric slab detachment, and 2-D and 3-D folding applied to fold nappe formation. In particular, we apply the 3-D code to quantify and visualize the evolution of the 3-D finite strain ellipsoid for the developing 3-D structures.

This chapter was accepted by
Geochemistry, Geophysics, Geosystems
co-authored by von Tscharnier M. and Schmalholz S. M.

2.1. Introduction

Many geological structures such as folds, boudins, mullions or domes which formed during the deformation of the Earth's crust and lithosphere have been caused by a contrast in mechanical strength and/or density between rock units (Johnson and Fletcher, 1994; Pollard and Fletcher, 2005; Ramsay, 1967). Therefore, these structures are often the result of a hydrodynamic instability, such as folding (buckling), necking or Rayleigh-Taylor diapirism (Pollard and Fletcher, 2005; Turcotte and Schubert, 2002). Many of these structures occur from the centimeter to the kilometer scale, and the related dominantly ductile deformation processes have a strong impact on the formation of, for example, fold-and-thrust belts, mountain ranges, extensional sedimentary basins or detached lithospheric slabs. Hence, a thorough quantitative understanding of the above mentioned instabilities is essential to better understand geodynamic processes.

The hydrodynamic instabilities that cause the above mentioned structures are relatively well studied theoretically with analytical and numerical methods in two dimensions (2-D) (Biot, 1961; Fletcher, 1974; Smith, 1977; Schmalholz *et al.*, 2008). For example, the mathematical analysis of low-amplitude Rayleigh-Taylor, necking and folding instabilities yields the growth rates of the amplitudes of sinusoidal (geometrical) perturbations on the material interfaces. These growth rates depend on the ratio of perturbation wavelength to layer thickness (i.e. geometry) and on the ratio of effective viscosities and densities (i.e. material properties) (Fletcher, 1974; Smith, 1977; Turcotte and Schubert, 2002). The strongest amplification of the interface occurs for a specific perturbation wavelength that is often termed the dominant wavelength (Biot, 1961). Structures that result from hydrodynamic instabilities are strongly controlled by this dominant wavelength. Analytical dominant wavelength solutions exist for various instabilities in 2-D and also in 3-D (Fletcher, 1991, 1995; Gosh, 1970; Kaus and Schmalholz, 2006; Muhlhaus *et al.*, 1998). Several studies showed that the deformation process is sensitive to the initial geometrical perturbation of the material interfaces and the related intra-layer stress distribution, and also that numerical solutions agree with analytical solutions only when the initial perturbation is small and well resolved numerically (Mancktelow, 1999; Schmalholz *et al.*, 2008). Generally, the analytical solutions are valid only for small amplitudes of the interface perturbations. Some approximate analytical solutions exist that are valid also for, for example, finite amplitude folding in 2-D (Adamuszek *et al.*, 2013; Schmalholz and Podladchikov, 2000; Schmalholz, 2006) and 3-D (Kaus and Schmalholz, 2006), or for finite amplitude necking in 2-D (Schmalholz *et al.*,

2008; Schmalholz, 2011). However, all the analytical solutions are valid only for relatively simple model configurations. Therefore, numerical solutions are essential to study the large amplitude (or large-strain) evolution of mechanical instabilities, and also to study the evolution of instabilities for more complex deformation scenarios (e.g. lateral fold propagation in 3-D; Grasemann and Schmalholz (2012); Schmid *et al.* (2008)). A thorough understanding of the large strain evolution of mechanical instabilities in rock is important, for example, to estimate the flow laws and material properties of rocks from the geometry of observed rock structures, such as folds and mullions (sometimes referred to as palaeo-rheology estimation; Kenis *et al.* (2004); Schmalholz and Podladchikov (2001)). Furthermore, accurate predictions of the finite strain, stress and pressure distribution on deformed material interfaces in 3-D are essential to quantify, for example, the fluid transfer between rock units or the fracture patterns in deformed rock units (Reber *et al.*, 2010).

Different numerical methods applied for geodynamic modelling with different rheologies have been presented in the last decades. These studies include 2-D models (Weinberg and Schmeling, 1992; Fullsack, 1995; van Keken *et al.*, 1997; Schmalholz *et al.*, 2001; Babeyko *et al.*, 2002; Gerya and Yuen, 2003; Moresi *et al.*, 2003; Gerya and Yuen, 2007) as well as 3-D models (Tackley *et al.*, 1993; Moresi *et al.*, 2007; Popov and Sobolev, 2008; Lechmann *et al.*, 2011; Thieulot, 2011). The algorithms that are presented in these studies are based on different methods such as the marker-in-cell finite difference (FD) method (Weinberg and Schmeling, 1992; Gerya and Yuen, 2007), an arbitrary Lagrangian Eulerian finite element method (ALE-FEM) (Fullsack, 1995; Popov and Sobolev, 2008), the finite element method with particles-in-cell (FEM-PIC) (Moresi *et al.*, 2003, 2007; Thielmann *et al.*, 2014) or a combined finite difference and finite element method (Babeyko *et al.*, 2002).

Here, we present a numerical algorithm based on the finite element method (FEM) and apply it to investigate the 3-D large strain evolution of hydrodynamic instabilities. Simulating these instabilities requires a numerical algorithm that can accurately resolve the initial low-amplitude material interfaces between model units with different strength (e.g. representing limestone and shale), and that can also accurately follow these interfaces during large strain deformation. Therefore, our FE code combines a deformable Lagrangian mesh with a contour-line technique in 3-D (i.e. material interfaces) and re-meshing. The algorithm PINK-3D is designed to simulate continuous 3-D deformation and employs a power-law viscoelastic rheology. The 3-D FE code is tested with various analytical solutions for the low-amplitude growth rates of folding,

necking and Rayleigh-Taylor instabilities, and for stress fields around circular inclusions. The 3-D code is also benchmarked with results of a different 2-D code, and tests are presented for the elasticity implementation. The code is further applied to 3-D viscoelastic folding, to power-law viscous necking during slab detachment and to fold nappe formation with laterally varying initial geometry.

2.2. Governing equations

The applied mathematical model is based on continuum mechanics. We assume that the ductile deformation of rocks can be described by the deformation of linear or power-law viscoelastic fluids. Continuum mechanics provides a system of partial differential equations that describes the deformation of materials. This system is solved here numerically with the FEM. The notation, meaning and units of the main quantities is given in Table 2.1. The governing equations describing the conservation of mass (i.e. continuity equation) and the conservation of linear momentum (i.e. force balance) for slow, incompressible flow in three dimensions with gravity acting in the vertical z -direction are:

$$\frac{\partial v_i}{\partial x_i} = 0 \quad (2.1)$$

$$\frac{\partial \sigma_{ij}}{\partial x_j} = \rho g_i \quad (2.2)$$

where $i = 1, 2, 3$ represent the three spatial directions, x_i are the two horizontal and the vertical Cartesian coordinates, v_i are the components of the three-dimensional velocity vector, $\partial/\partial x_i$ are the partial derivatives with respect to the x_i -direction, σ_{ij} are the components of the stress tensor, ρ is the density and g_i are the components of the gravitational acceleration vector ($\mathbf{g} = (0, 0, g)^T$; superscript T indicates the transpose of a vector, i.e. \mathbf{g} is a column vector). Repeated indices are summed according to the Einstein summation convention. The total stress tensor σ_{ij} is split into its deviatoric and mean parts:

$$\sigma_{ij} = -p\delta_{ij} + \tau_{ij} \quad (2.3)$$

where $p = -\sigma_{ii}/3$ is the pressure (i.e. mean stress), δ_{ij} is the Kronecker delta and τ_{ij} are the components of the deviatoric stress tensor (i.e. the stress deviation from the mean stress). The compliance relationship for the viscous rheology is defined as:

$$\frac{1}{2\eta_{eff}}\tau_{ij} = \dot{\epsilon}_{ij} \quad (2.4)$$

where η_{eff} is the effective viscosity and $\dot{\epsilon}_{ij}$ are the components of the strain rate tensor:

$$\dot{\epsilon}_{ij} = \frac{1}{2} \left(\frac{\partial v_i}{\partial x_j} + \frac{\partial v_j}{\partial x_i} \right) \quad (2.5)$$

For a power-law viscous fluid the effective viscosity is defined as:

$$\eta_{eff} = \eta E_{II}^{\frac{1}{n}-1} \quad (2.6)$$

where η is the viscosity coefficient, n is the power-law stress exponent and E_{II} is the second invariant of the tensor $\dot{\epsilon}_{ij}$:

$$E_{II}(\dot{\epsilon}_{ij}) = \sqrt{\frac{1}{2}\dot{\epsilon}_{ij}\dot{\epsilon}_{ij}} \quad (2.7)$$

Since the effective viscosity is dependent on E_{II} and hence on v_i , the rheological equation becomes non-linear. The non-linearity is treated with Picard-iterations which are described further below in section 2.3.3. For the viscoelastic formulation equation (2.4) is extended with an elastic part. It is assumed that the viscoelastic deformation is also incompressible. In the Maxwell model an elastic element and a viscous element are connected in series. Therefore, the strain rate tensor components are the sum of elastic strain rates, $\dot{\epsilon}_{ij}^e$, and viscous strain rates, $\dot{\epsilon}_{ij}^v$, and the compliance relation for the viscoelastic deviatoric strain rate is:

$$\dot{\varepsilon}_{ij}^e + \dot{\varepsilon}_{ij}^v = \frac{1}{2G} \overset{\circ}{\tau}_{ij} + \frac{1}{2\eta_{eff}} \tau_{ij} = \dot{\varepsilon}_{ij} \quad (2.8)$$

where G is the elastic shear modulus and $\overset{\circ}{\tau}_{ij}$ are the Jaumann derivatives (objective time derivative) of the deviatoric stress tensor components (see definition further below). The effective viscosity of a power-law fluid is only dependent on viscous strain rates but not on strain rates resulting from an elastic deformation. Therefore, to calculate the effective viscosity for a power-law viscoelastic fluid a strain rate invariant must be used that only depends on viscous strain rates. The effective viscosity for the viscoelastic model is hence defined different than for the viscous model:

$$\eta_{eff} = \eta E_{IIv}^{\frac{1}{n}-1} \quad (2.9)$$

where E_{IIv} is the second invariant of the viscous component of the strain rate tensor, that is, E_{IIv} is a function of $\dot{\varepsilon}_{ij} - \dot{\varepsilon}_{ij}^e$ or $\dot{\varepsilon}_{ij}^v$. E_{IIv} is defined as:

$$E_{IIv} = \frac{\tau_{II}}{2\eta_{eff}} \quad (2.10)$$

where τ_{II} is the second invariant of the deviatoric stress tensor:

$$\tau_{II} = \sqrt{\frac{1}{2} \tau_{ij} \tau_{ij}} \quad (2.11)$$

The calculation of the stress tensor components τ_{ij} is explained further below in equation (2.18). Since E_{IIv} is dependent on the effective viscosity, the rheological equation is also non-linear. This non-linearity is also treated with Picard-iterations. We used different formulas to calculate the second invariant of the strain rate tensor (equations 2.7 and 2.10), because for the viscous model the second invariant can be calculated directly from the resulting strain rates and it is not necessary to calculate first the stresses. For the viscoelastic model, it is necessary to calculate the second strain rate invariant from the stresses.

The Jaumann derivatives (e.g. Altenbach (2012)) are defined as:

$$\dot{\tau}_{ij} = \frac{D\tau_{ij}}{Dt} + \tau_{ik}W_{kj} - W_{ik}\tau_{kj} \quad (2.12)$$

where D/Dt is the material derivative, t is the time and W_{ij} is the spin tensor:

$$W_{ij} = \frac{1}{2} \left(\frac{\partial v_i}{\partial x_j} - \frac{\partial v_j}{\partial x_i} \right) \quad (2.13)$$

For an infinitely high value for G the rheological equation (2.8) reduces to the viscous equation (2.4) (i.e. $1/2G$ tends to zero). To obtain an effectively viscous behaviour for the viscoelastic model we use values of G that are 10 orders of magnitude larger than the viscosity of the corresponding material. In the numerical algorithm we use an if-else-condition to run simulations either for viscoelastic or viscous fluids. We further assume that the material parameters do not change with time.

Symbol	Meaning	Unit
σ_{ij}	stress tensor components	Pa
τ_{ij}, τ_{ij}^k	deviatoric stress tensor components	Pa
τ_{II}	second invariant of deviatoric stress tensor	Pa
$\mathbf{x}, \tilde{\mathbf{x}}, x_i$	Cartesian coordinates	m
ξ_i	local coordinates within the element	m
\mathbf{v}, v_i	velocity, velocity in x_i -direction	$m.s^{-1}$
ρ	density	$kg.m^{-3}$
\mathbf{g}, g_z	gravity	ms^{-2}
η_{eff}	effective viscosity	$Pa.s$
η	viscosity coefficient	$Pa.s^{1/n}$
$\dot{\epsilon}_{ij}$	strain rate tensor components	s^{-1}
E_{II}, E_{IIv}	second invariant of the strain rate tensor	s^{-1}
n	power-law stress exponent	
G	elastic shear modulus	Pa
$\dot{\nu}_{ij}$	Jaumann derivatives	$Pa.s^{-1}$
C_{ij}	Jaumann correction terms due to elasticity	$Pa.s^{-1}$
Δt	time step	s
K	incompressibility or penalty parameter	Pa
W_{ij}	components of the spin tensor	s^{-1}
δ_{ij}	Kronecker delta	
N_v^k, \mathbf{N}_v	velocity shape functions	
N_p^k, \mathbf{N}_p	pressure shape functions	

Table 2.1: Nomenclature, notation, meaning and units of the used quantities.

2.3. Numerical Method

PINK-3D is written in MATLAB (TheMathWorks) using the FEM. The MATLAB code is available online as supplementary material. Here, we summarize the main features of the numerical algorithm.

2.3.1. Temporal discretisation

The mass balance equation can be written as:

$$\nabla^T \cdot \mathbf{v} = 0 \quad (2.14)$$

where ∇ is the Nabla operator and $\mathbf{v} = (v_x, v_y, v_z)^T$ is the velocity vector (the subscripts x, y and z are used here instead of indices 1, 2 and 3, respectively). The incompressibility (i.e. conservation of mass) is not directly implemented in the FE algorithm. The mass balance equation is modified to:

$$\frac{Dp}{Dt} = -K(\nabla^T \cdot \mathbf{v}) \quad (2.15)$$

where K is the incompressibility or the penalty parameter. The material derivative of the pressure is approximated with the finite difference method (FD method):

$$\frac{Dp}{Dt} \approx \frac{p^{k+1} - p^k}{\Delta t} = -K(\nabla^T \cdot \mathbf{v}) \quad (2.16)$$

where p^k and p^{k+1} are the pressures for the time t and $t + \Delta t$, respectively and Δt is the time increment. The time in equation (2.15) and equation (2.16) is an "artificial time" used only for preconditioning. The partial time derivative of the deviatoric stress tensor is also defined using the FD method:

$$\frac{D\tau_{ij}}{Dt} \approx \frac{\tau_{ij}^{k+1} - \tau_{ij}^k}{\Delta t} \quad (2.17)$$

where τ_{ij}^k and τ_{ij}^{k+1} are the components of the deviatoric stress tensor for the time t and $t + \Delta t$, respectively. We use a Lagrangian method and therefore do not have to consider the advective terms.

In order to implement the rheological equation into the algorithm, equation (2.4) and equation (2.8) are solved for τ_{ij} . This is trivial for the power-law viscous rheology and leads to $\tau_{ij} = 2\eta_{eff}\dot{\epsilon}_{ij}$. In the viscoelastic case we use the FD derivative approximation for $D\tau_{ij}/Dt$ and resolve the equation for τ_{ij}^{k+1} :

$$\tau_{ij}^{k+1} = 2\mu \dot{\epsilon}_{ij} + S(\tau_{ij}^k - \Delta t C_{ij}) \quad (2.18)$$

$$\mu = \frac{1}{\frac{1}{G\Delta t} + \frac{1}{\eta_{eff}}} \quad (2.19)$$

$$S = \frac{1}{1 + \frac{G\Delta t}{\eta_{eff}}} \quad (2.20)$$

$$C_{ij} = \tau_{ik}^k W_{kj} - W_{ik} \tau_{kj}^k \quad (2.21)$$

Equation (2.18) reduces to the viscous flow law when $G \rightarrow \infty$ ($\mu \rightarrow \eta_{eff}$ and $S \rightarrow 0$) and to the elastic one for $\eta_{eff} \rightarrow \infty$ ($\mu \rightarrow G\Delta t$ and $S \rightarrow 1$).

2.3.2. Spatial discretisation

We use the FEM because with this method we are able to follow the initial geometrical perturbations with the FE mesh. In the applied FE algorithm we use a structured hexahedral mesh with tri-quadratic shape functions for the velocity (Q2), and piece-wise discontinuous linear shape functions for the pressure (P1) (Bathe, 1996) (see appendix 2.8). The advantage of the FEM and the hexahedral elements is the uniform data structure and the possibility to locally generate a finer mesh (sometimes referred to as ‘‘Swiss cross’’). The derivations of the finite element discretization of the governing equations is presented in several textbooks (Bathe, 1990; Zienkewicz and Taylor, 2000). The finite element approximation is given by:

$$\mathbf{v}(\mathbf{x}) \approx \sum_k N_v^k(\mathbf{x}) \tilde{\mathbf{v}}_k \quad (2.22)$$

$$\mathbf{p}(\mathbf{x}) \approx \sum_k N_p^k(\mathbf{x}) \tilde{\mathbf{p}}_k \quad (2.23)$$

where $\mathbf{v}(\mathbf{x})$ and $\mathbf{p}(\mathbf{x})$ are the velocities and the pressure, respectively, $N_v^k(\mathbf{x})$ and $N_p^k(\mathbf{x})$ are the velocity and pressure shape functions, where k is the node index and $\tilde{\mathbf{v}}_k$ and $\tilde{\mathbf{p}}_k$ are the velocities and the pressure at the nodes, respectively. The shape functions are given in Bathe (1996). A summary of the finite element discretization, the weak form, the matrix assembly and the Voigt notation is given in appendix 2.8.

2.3.3. Non-linear solver

We introduce a penalty term in the continuity equation and solve for each time step the penalised system by applying a Richardson iteration to the reduced velocity Schur complement system (Dabrowski *et al.*, 2008). For this we use an incompressibility or penalty parameter of $K = 10^{12}$ Pa and an initial guess for the pressure of $p^0 = 0$. The stopping condition is reached when the maximum divergence of the dimensionless velocity is smaller than 10^{-10} . The non-linearities due to a power-law viscosity are treated with Picard iterations. For each time step the viscosities are calculated iteratively. In the case of a viscoelastic rheology the initial guess for the stress is $\tau_{ij}^0 = 0$. The stopping condition is reached when the velocity error, which is defined as the maximum relative difference between the new velocity and the velocity of the previous iteration step, is smaller than 10^{-5} .

The time step Δt is chosen so that the convergence criteria is fulfilled within the first time steps within 5 Picard iteration steps. The total number of Picard iterations is limited to 10 because for some occasional time steps it is possible that the convergence criterion is just not reached. The accuracy of the applied iteration scheme was tested for low-amplitude diapirism, necking, large-strain power-law folding and slab detachment with re-meshing (see section ??).

An overview of the algorithm is given as a flow chart in the appendix (figure 2.1).

2.3.4. Interface tracking

Within our 3-D numerical model, we represent all material interfaces (e.g. between mechanically strong and weak units) as iso-surfaces that are described by a set of interface points. The interface points form a regular grid with a resolution that is 3 to 10 times higher than the one of the FE mesh, depending on the model configuration. Interface points can be located within

a FE and it is necessary to calculate the corresponding local coordinates. To calculate the local coordinates of an interface point it is necessary to determine this element that contains the interface point. We use a regular hexahedral FE mesh and calculate the local coordinates for each interface point only once for the initial configuration or directly after re-meshing. For the initial configuration or directly after re-meshing all vertical lines in the FE mesh are straight, and it is straight forward to find the element that contains the interface point using the global coordinates of the element nodes. The global coordinates of the interface points are known and to calculate the local coordinates of the interface points we use the FE approximation:

$$\mathbf{x} \approx \sum_k N_v^k(\xi) \tilde{\mathbf{x}} \quad (2.24)$$

where \mathbf{x} and ξ are vectors containing the global and local coordinates of the interface point, respectively, and $\tilde{\mathbf{x}}$ are the global coordinates of the elements nodes. Since we use tri-quadratic shape functions for the velocity this is a non-linear system of equations which we solve with Newton-Raphson iterations. Therefore, we define the following function for which we want to find the zeros:

$$\mathbf{F}(\xi) = \mathbf{x} - \sum_k N_v^k(\xi) \tilde{\mathbf{x}} \quad (2.25)$$

i.e. we search for ξ such that $\mathbf{F}(\xi) = 0$. $\mathbf{F}(\xi)$ can be split in three functions with respect to the three cartesian directions in space:

$$\mathbf{F}(\xi) = \begin{pmatrix} F_1(\xi) \\ F_2(\xi) \\ F_3(\xi) \end{pmatrix} = \begin{pmatrix} x - \sum_k N_v^k(\xi) \tilde{x} \\ y - \sum_k N_v^k(\xi) \tilde{y} \\ z - \sum_k N_v^k(\xi) \tilde{z} \end{pmatrix} \quad (2.26)$$

The Newton-Raphson iteration uses the Jacobian \mathbf{J} of the function $\mathbf{F}(\xi^{ip})$ to iteratively find the zeros:

$$\xi_{i+1} = \xi_i - \mathbf{J}^{-1} \mathbf{F}(\xi_i) \quad (2.27)$$

where i and $i + 1$ are the iteration steps and the Jacobian is defined using the split version of the function $\mathbf{F}(\xi)$:

$$J_{ij} = \frac{\partial F_i}{\partial \xi_j} \quad (2.28)$$

where ξ_j are the local coordinates of the interface point. The iteration is done until the relative change of the local coordinates (L₂-Norm)

$$R = \frac{\|\mathbf{J}^{-1}\mathbf{F}(\xi_i)\|_2}{\|\xi_i\|_2} \quad (2.29)$$

is smaller than 1e-3. The initial guess for the local coordinates is $\xi_0 = (0,0,0)$ which is the center of the element.

The FE mesh is deformed during the simulations and after each time step the element nodes are moved with the calculated velocities (explicit Euler step):

$$\mathbf{x}^{k+1} = \mathbf{x}^k + \mathbf{v}\Delta t \quad (2.30)$$

where \mathbf{x}^{k+1} and \mathbf{x}^k are the new and old coordinates of the element nodes, respectively, and k and $k + 1$ are the time steps. The global coordinates of the interface points can be determined by the element shape functions using equation (2.24). There is hence no need to interpolate the velocities to the interface points in order to move the material interfaces. The global coordinates of the interface points are updated during the Lagrangian deformation of the FE mesh whereas the local coordinates remain constant (see Poliakov and Podladchikov (1992) for details). The interface points are "frozen" within the deforming elements. During the simulations it was not necessary to resample the material interfaces.

2.3.5. Re-meshing

During the deformation the elements get distorted and thus the FE mesh quality degenerates. At each re-meshing step a new structured FE mesh is generated. Depending on the geometry the new mesh is generated using the material interfaces to define areas with higher resolution. In a first step three vectors containing x -, y - and z -coordinates of the FE nodes are defined. Using these three vectors the mesh is generated in 3-D. If we use a free surface the initial z -vector is defined using the mean height of the model. The columns with vertical nodal coordinates are then stretched or shortened to the actual height corresponding to each horizontal coordinate. The new height is interpolated using the coordinates of the top surface just before the re-meshing.

The material interfaces can cross individual elements. The material phase (material properties) for each quadrature point is defined using a self-made algorithm which finds all quadrature points which are within the volume of a specific material phase defined by the material interfaces. The algorithm determines all intersections of the material interface with a vertical line located at the horizontal coordinates of the corresponding quadrature point. The material interface is defined as a set of interface points which are initially laid out on a regular grid. Therefore, the material interfaces can be divided in triangles connecting three neighbouring interface points. First, the triangles are projected to the horizontal plane with $z=0$. Then we search for all triangles that contain the projection of the quadrature point on the same horizontal plane. Next we determine the actual height of the determined triangle at the horizontal position of the corresponding quadrature point. We are hence able to determine whether the quadrature point is located above or below a triangle of the material interface and consequently whether the quadrature point is located inside or outside the volume which is defined by a material interface. During the re-meshing the new local coordinates of the material interfaces are determined as described in section 2.3.4.

Initially, the faces of the FEs conform to the initial material interfaces (whenever possible) and can hence resolve accurately any small initial geometrical perturbation on the material interfaces. However, once re-meshing has occurred the material interfaces will intersect the FEs. This intersection leads to a sharp contrast in material properties inside these elements (Fig. 2.1). The FE algorithm PINK-3D hence combines a numerical contour-line technique in 3-D and a deformable Lagrangian mesh with re-meshing, similar to the 2-D FE code described by Poliakov and Podladchikov (1992). After the re-meshing the FE mesh is deformed again in a Lagrangian

way until the next re-meshing. An inclusion test described in a following section shows that the nodal velocities are accurate also when material interfaces cross the FE. Therefore, the element nodes (and hence the material interfaces) are moved with accurate velocities during the entire large strain deformation. We did not use a specific metric to determine if re-meshing is necessary for all the different simulations. Each simulation was run from the beginning until the time step for which the mesh became too distorted (i.e. the solver would crash). This number of time steps (different for the different simulations) was then chosen as the constant re-meshing interval.

Further, we did not yet implement an interpolation of the stored elastic stresses between the old and new meshes. Therefore, the viscoelastic simulations were used without re-meshing. In the case of single-layer folding it was possible to run the simulations without re-meshing up to very high amplitudes where the limbs of the single-layer fold are almost vertical and parallel (see section 2.5.1).

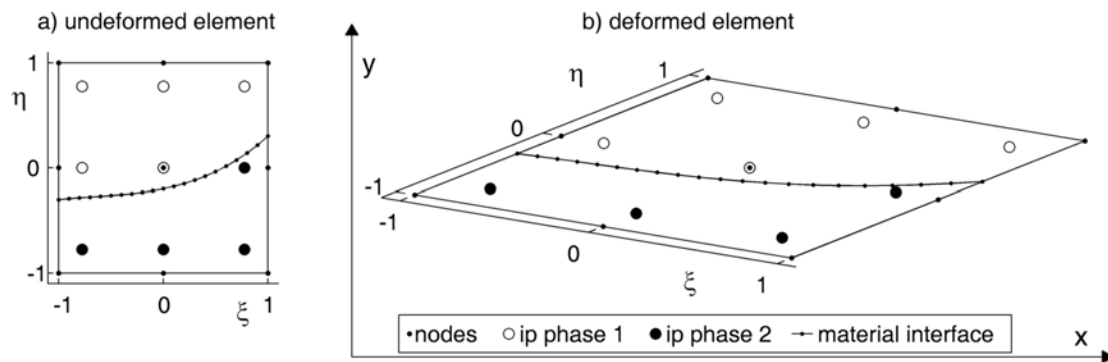


Figure 2.1: 2-D sketch of a nine-node finite element with nine integration points. a) undeformed reference geometry in local coordinate system (ξ and η) and deformed geometry in global coordinate system (x and y). Local coordinates are also displayed. A material interface with contour points crosses the element and separates the integration points which belong to material phase 1 from the integration points which belong to material phase 2. During the deformation the contour points on the material interface keep their local coordinates and are deformed accurately together with the element.

2.4. Benchmark

The 3-D numerical algorithm PINK-3D has been tested with 2-D analytical solutions for Rayleigh-Taylor diapirism, folding and necking of power-law viscous layers, and with 3-D ana-

lytical solutions for folding and Rayleigh-Taylor diapirism in linear viscous (Newtonian) fluids. The results from the 3-D code have also been compared with the 2-D analytical solution for a viscous inclusion under pure shear for the case of material interfaces that cross a rectangular FE mesh (referred to here as viscous inclusion test). Furthermore, results from the 3-D code have been compared with results from 2-D FE simulations for large strain Rayleigh-Taylor diapirism and power-law viscous folding to test the re-meshing technique during large strain deformation (referred to here as re-meshing test). In the following sections we only present the results for the viscous inclusion and the re-meshing test, and all other test results and the applied analytical solutions are described in appendix 2.9.

2.4.1. Viscous inclusion test - convergence test

In order to test the numerical results for a material interface that crosses through individual rectangular FEs we use the analytical solution for a two-dimensional viscous inclusion under pure shear (Schmid, 2003). A similar inclusion test is presented by ?. The inclusion has a linear viscosity that is 1000 times larger than the linear viscosity of the surrounding matrix. The results are presented in figures 2.2-2.4, where we show the spatial distribution of numerically calculated pressure and velocity magnitudes (Fig. 2.2a and b), the spatial distribution of the error in pressure and velocity magnitudes on the integration points and on the nodal points, respectively (Fig. 2.2c and d). The total error in pressure and velocity magnitudes integrated over the whole model domain versus the nodal FE resolution and the number of integration points per element is displayed in figure 2.3. The material interfaces that cross FEs are responsible for numerical errors in the pressure and velocity magnitude. However, the numerical solutions for the velocity magnitude and pressure are relatively smooth, and the total error in pressure and velocity magnitudes (e_p^{tot} and e_v^{tot} , see Appendix 2.9 for the definition) decreases with increasing numerical resolution (Fig. 2.3a and b). In a log-log plot the pressure error decreases with increasing resolution with a slope of approximately 0.5, and the velocity error with a slope of approximately 2. If the viscosity structure is smooth, or discontinuous but aligned with the element faces, the theoretical lower bounds on the order of accuracy (in the L_2 norm) are 2 and 3 for the pressure error and the velocity error, respectively (Elman *et al.*, 2005). Our results are consistent with previous numerical simulations which utilised FEs that possessed discontinuous inter-element viscosity structures (Kronbichler *et al.*, 2012; Thielmann *et al.*, 2014). Increasing the number of integration points per element (higher order quadrature) causes a slightly larger error in pressure

and velocity magnitudes (Fig. 2.3c and d). The likely reason for this error increase is that numerical Gauss quadrature assumes that the function to integrate is a polynomial, and therefore higher order quadrature tries to fit a higher order polynomial through the discontinuous function across the material interface. However, discontinuous functions are not accurately described by high order polynomials (e.g. Gibbs phenomena). Hence, increasing the polynomial order will increase the interpolation error as the polynomials at the discontinuity tend to overshoot and undershoot the correct function (Fig. 2.4). Therefore, the slightly larger errors due to using higher order quadrature are expected. Increasing the number of integration points in the elements does hence not increase the accuracy of the numerical solution, but could be of interest to spatially better resolve and visualize the velocity and pressure field around the interface.

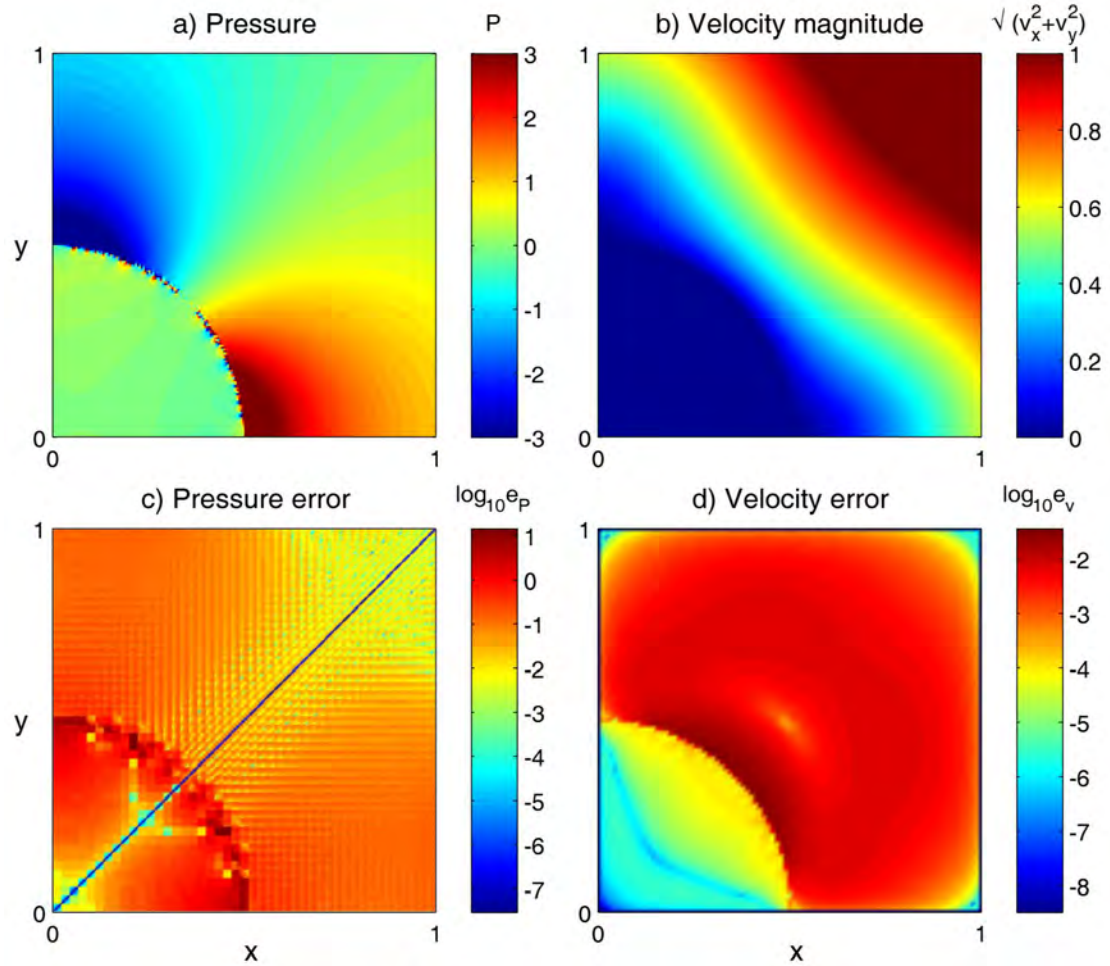


Figure 2.2: Results for a viscous inclusion in a viscous matrix under pure shear. The origin of the circular inclusion with a radius of $r = 0.5$ is located at $(0,0)$. We use dimensionless viscosities of $\eta_1 = 10^3$ and $\eta_2 = 1$ for the inclusion and the surrounding material, respectively. a) and b) Spatial pressure and velocity distribution within and around the viscous inclusion. c) and d) Spatial distribution of the error in pressure and velocity, respectively.

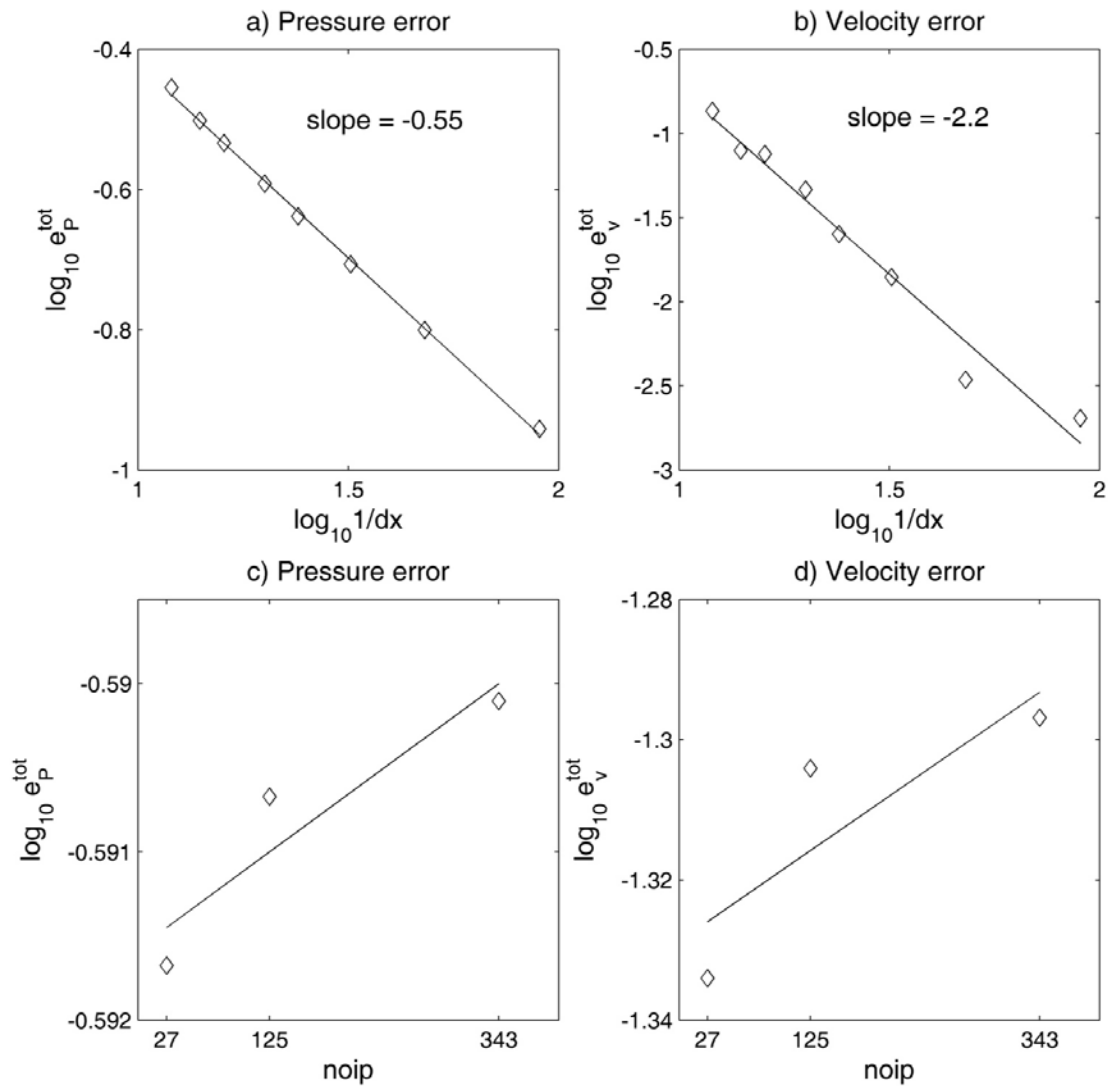


Figure 2.3: Convergence test for a viscous inclusion in a viscous matrix under pure shear. Integrated error in pressure and velocity over the model domain versus the nodal FE resolution (a and b) and versus the number of integration points per element (c and d). We use either $27 = 3^3$, $125 = 5^3$ or $343 = 7^3$ integration points.

Figure 2.4 shows the pressure and the velocity magnitudes along a section through the inclusion model using different numbers of integration points per element. The pressure shows a sharp discontinuity at the inclusion boundary. The numerical results deviate from the analytical solution

where the higher order quadrature shows a higher divergence around the pressure discontinuity. In contrast, the total velocity is smooth, accurate and independent on the number of quadrature points per element.

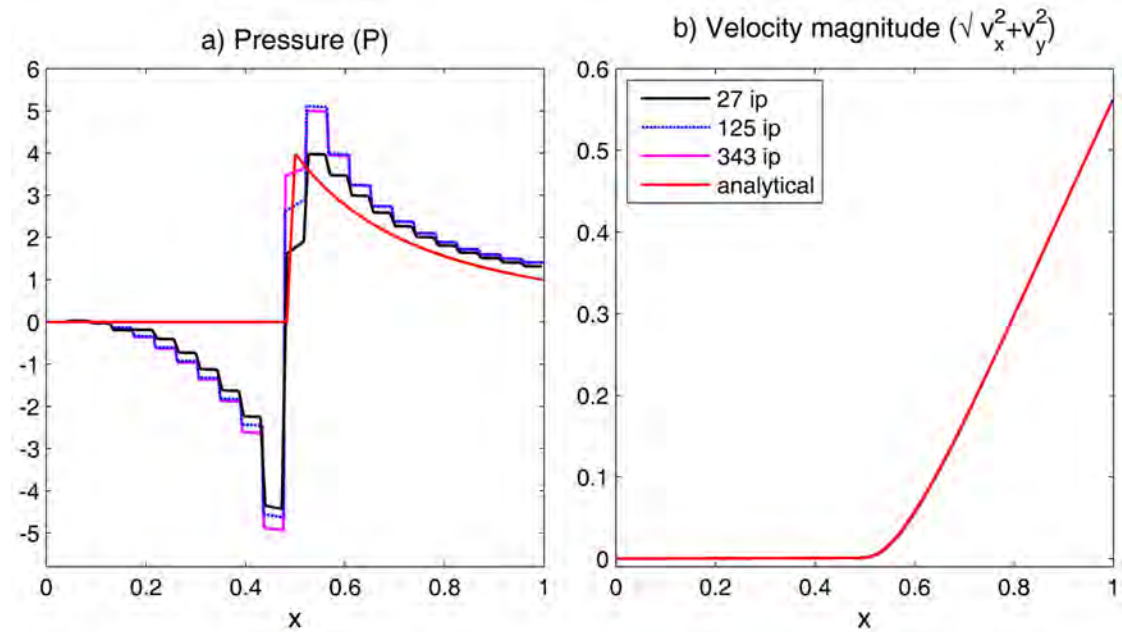


Figure 2.4: Pressure and velocity along a section through the inclusion model for $y = 0$ for the analytical solution and the 3-D results using different numbers of integration points per element.

2.4.2. Re-meshing test

For large strain folding and diapirism the 3-D code has been benchmarked with the results of a 2-D FE code (see Burg and Schmalholz (2008); Schmalholz *et al.* (2008); Schmalholz (2011) for details). For these benchmarks the 3-D code was applied with only one FE in the third, lateral direction (i.e. orthogonal to the coordinate directions of the 2-D simulation). For Rayleigh-Taylor diapirism and single-layer folding 2-D and 3-D cylindrical simulations were performed with the same initial geometry, material parameters and boundary conditions, but with different re-meshing scenarios (Table 4.1). For example, for the first simulation of the Rayleigh-Taylor diapirism (RT_01) the first re-meshing was performed after 40 time steps and after that at every tenth time step.

Rayleigh-Taylor instability		
simulation	first re-meshing	re-meshing step
RT_01	40	10
RT_02	20	10
RT_03	3	3
RT_04	1	1
Power-law single-layer folding		
simulation	first re-meshing	re-meshing step
SF_01	20	10
SF_03	3	3
SF_04	1	1

Table 2.2: Re-meshing parameters used in the high-amplitude simulations in order to compare 2-D results with our 3-D FE code with re-meshing.

Therefore, the simulation is Lagrangian with a deforming mesh until the 40th time step, at which the re-meshing generates a new rectangular mesh in which the material interface crosses individual FEs. Figure 2.5 shows the amplitude to wavelength ratio, A/λ , calculated for the 2-D and 3-D numerical results versus the time steps for power-law viscous single-layer folding and Rayleigh-Taylor diapirism. In the case of single-layer folding we used an initial effective viscosity contrast of $R = \eta_L/\eta_M = 100$, and power-law stress exponents of $n_L = 5$ and $n_M = 3$ for the layer and matrix, respectively. The dimensionless initial perturbation amplitude is $A_0 = 0.04$, the dimensionless layer thickness is $H = 1$ (with the dimensional layer thickness being the characteristic length scale), the dimensionless model width is $\lambda = 11.8$ (dominant wavelength) and the total dimensionless model height is $H_{Model} = 11$. The boundary conditions are free slip for the left and bottom boundary ($x = 0, z = 0$), pure shear shortening for the right boundary ($x = \lambda$) and the top boundary ($z = H_{Model}$) is a free surface. For the non-dimensionalization the layer thickness H , the matrix viscosity η_M and the background strain rate were taken as characteristic length, viscosity and strain rate, respectively. For the Rayleigh-Taylor instability we used a density difference of $\Delta\rho = \rho_2 - \rho_1 = 1000$, a contrast of linear viscosities of $R = \eta_2/\eta_1 = 10$, an initial perturbation amplitude of $A_0 = 0.005$, a layer thickness of $H = 1$, a total model height of $2H = 2$ and a model width of $\lambda = 2.56$ (dominant wavelength). The boundary conditions are free slip for the vertical boundaries ($x = 0, x = \lambda$) and no slip for the horizontal boundaries ($z = 0, z = 2H$). For the non-dimensionalization we used the layer thickness H and the viscosity η_1 as characteristic length and viscosity. The model configuration and the material properties

are shown in the appendix in figure 2.1a and 2.1b for the Rayleigh-Taylor instability and for the single-layer folding, respectively. The numerical resolution (number of elements in every direction) used for the 3-D cylindrical simulations in the re-meshing test was $24 \times 1 \times 28$ and $37 \times 1 \times 28$ for the single-layer folding and the Rayleigh-Taylor instability, respectively. In both cases the solid black lines represent the 2-D solution whereas the different markers represent the 3-D results with different re-meshing scenarios (Fig. 2.5). The black markers denote the time step where the re-meshing was performed.

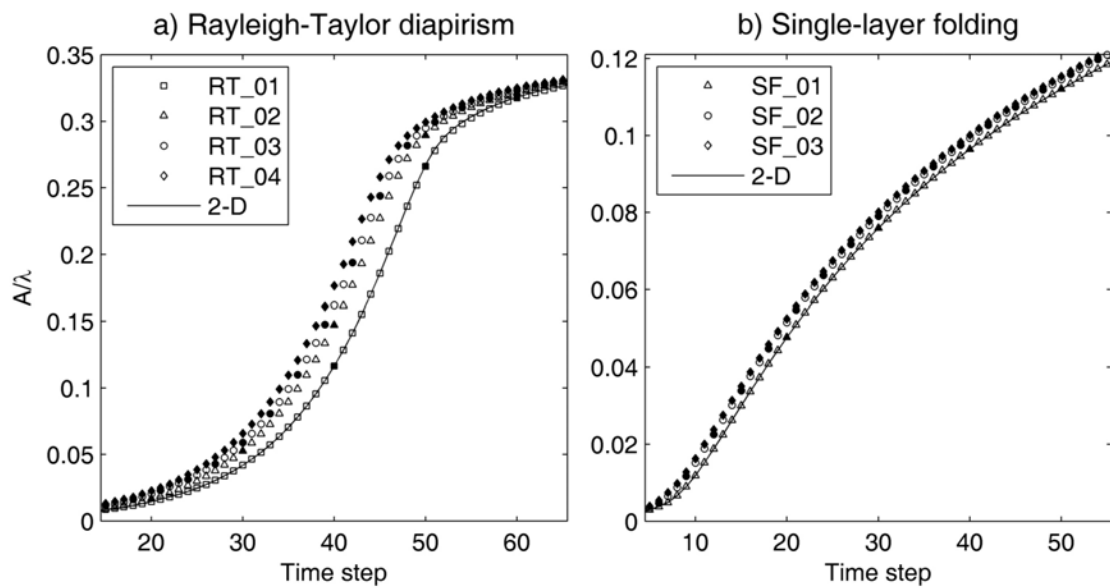


Figure 2.5: Finite amplitude results of the two-dimensional and different three-dimensional FE simulations for cylindrical Rayleigh-Taylor diapirism (a) and cylindrical single layer folding (b). In both cases the solid black lines represent the 2-D solution whereas the different markers represent the 3-D results. The black markers denote the time step where the re-meshing was performed.

If the first re-meshing in the 3-D simulations is performed too early, then the error (deviation of 3-D from 2-D solution) becomes larger, especially, in the case of the Rayleigh-Taylor diapirism. However, this error is highly dependent on the initial perturbation amplitude, the resolution of the FE mesh and the time step. Therefore, it is very important to carefully choose the time step of the first re-meshing. The first re-meshing should be generally performed when the exponential amplification starts to slow down, but before the FE mesh becomes unsatisfactory. In other words, the first re-meshing should be done as late as possible. If the re-meshing is performed

after each time step the method would be similar to the FEM using a particle-in-cell scheme (FE-PIC, for example Thielmann *et al.* (2014)).

2.5. Simulations

2.5.1. Single-layer viscoelastic folding

Folds are common structures in the Earth's deformed lithosphere and occur from the millimeter (crenulation cleavage) to the hundreds of kilometer (lithospheric folds) scale. Folds usually result from a layer-parallel compression of a mechanically layered system for a variety of rheologies (e.g. linear viscous, power-law viscous, elastic or viscoelastic) (Biot, 1961; Fletcher, 1974; Schmalholz and Podladchikov, 1999; Smith, 1977). Viscoelasticity is likely important during the folding of the continental and oceanic crust (McAdoo and Sandwell, 1985; Schmalholz and Podladchikov, 2001; Schmalholz *et al.*, 2002). Schmalholz and Podladchikov (1999) showed that the dominant wavelength ratio $R_\lambda = \lambda_{dv}/\lambda_{de}$ controls viscoelastic folding, where $\lambda_{dv} = 6^{-1/3}(\eta_L/\eta_M)^{1/3}$ and $\lambda_{de} = (G_L/P_0)^{1/2}$ are the viscous and elastic dominant wavelength, respectively. η_L , η_M , G_L and P_0 are the viscosity of the layer, the viscosity of the matrix, the shear modulus of the layer and the layer parallel stress, respectively. There is a transition from viscous to elastic dominated folding around $R_\lambda = 1$.

To test the algorithm PINK-3D for 3-D viscoelastic folding we use a 3-D model configuration with an initial sinusoidal perturbation as described for the folding benchmark in appendix 2.9. All model dimensions and material parameters are given in dimensionless numbers, where the non-dimensionalization was done using the layer thickness H , the matrix viscosity η_M and the background strain rate as characteristic length, viscosity and strain rate, respectively. Two simulations were performed: One for viscous folding with $\eta_L = 500$ and $\eta_M = 1$, and one for viscoelastic folding using a dominant wavelength ratio of $R_\lambda = 1$ (viscoelastic layer in viscous matrix) with $\eta_L = 500$, $\eta_M = 1$, $G_L = 8220$ and $G_M = 10^{10}$. The boundary conditions are pure shear shortening in the two horizontal directions (x- and y- direction) and pure shear extension in the vertical direction (z-direction) with a strain rate ratio of $R_{\dot{\epsilon}} = \dot{\epsilon}_x/\dot{\epsilon}_z = 0.75$. The model domain is given by $\Omega = [0, 14] \times [0, 27] \times [0, 21]$, the layer thickness is $H = 1$ and the layer is vertically located in the middle of the model as shown in appendix 2.9 figure 2.1 e. The value

for G_M is chosen unrealistically high to make the viscoelastic matrix effectively viscous. The results of these simulations using a numerical resolution of $14 \times 27 \times 26$ are shown in figure 2.6.

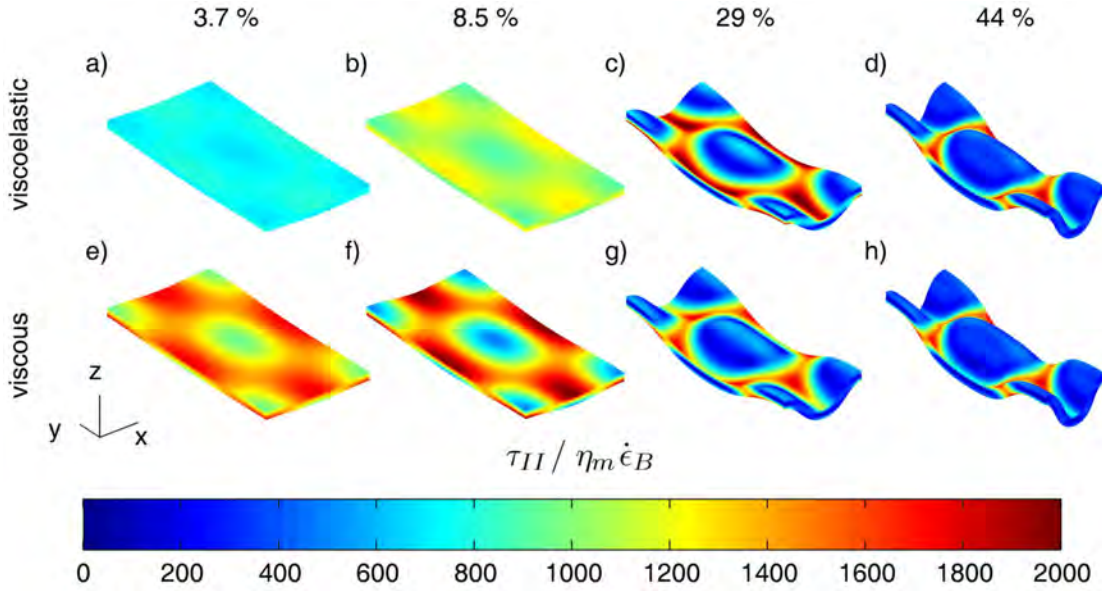


Figure 2.6: Results for 3-D single-layer folding. a) to d) show results for a viscoelastic layer and e) to h) for a linear viscous layer (see text for details) for different amounts of bulk shortening in the x-direction (numbers in %). The color indicates the second invariant of the stress tensor of the layer on the top layer interface. The stress is normalized by the product of the matrix viscosity η_M and the background strain rate $\dot{\epsilon}_B$.

The colors on the layer surface for 3.7, 8.5, 29 and 44% bulk shortening in the x-direction indicate the dimensionless second invariant of the deviatoric stress tensor. Both simulations were performed using a Lagrangian FE mesh without re-meshing. The second invariant of the stress tensor is plotted on the layer interface by using the interpolation points which lie inside the layer just below the interface. In both cases the stresses within the single-layer are smooth. For viscoelastic single-layer folding a stress build up occurs during the initial stages of folding whereas the viscous layer exhibits the viscous stress from the onset of the deformation. To quantify the deformation we show in figure 2.7 the finite strain and the normalized strain rate invariant ($E_{II}/\dot{\epsilon}_B$) on the layer surface for 8.6, 29, 45 and 59% bulk shortening in the x-direction. The colors on the material interface indicate the dimensionless second invariant of the strain rate tensor. The circles have an initial dimensionless diameter of $d/H = 1$ and are deformed using interpo-

lated nodal velocities. These deformed circles allow us to visualize the directions of maximum extension and shortening on the deformed surface. The correct implementation of elasticity has been successfully tested by two benchmarks which are described in the appendix.

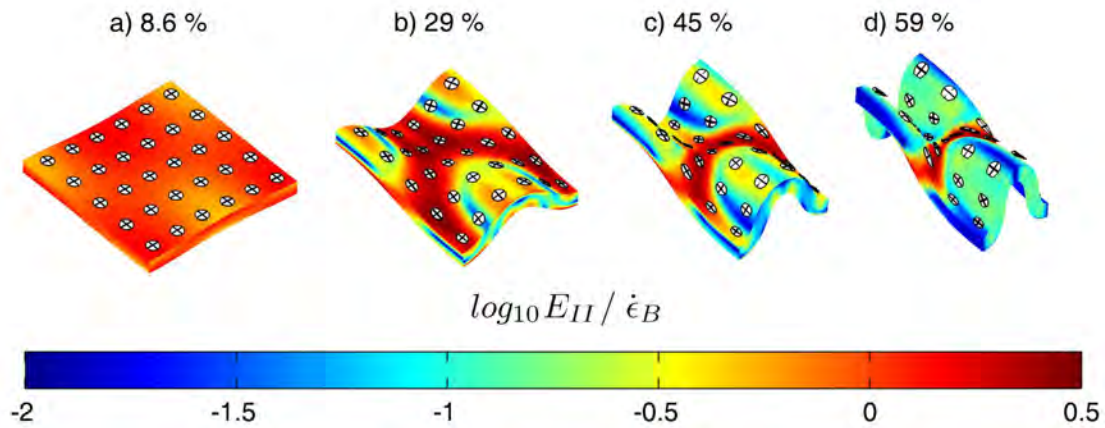


Figure 2.7: Deformed circles on the layer-matrix interface for 8.6, 29, 45 and 59% bulk shortening in x-direction for a viscoelastic layer in a viscous matrix. The initial circles are deformed using interpolated nodal velocities. The color on the material interface indicates the dimensionless second invariant of the strain rate tensor.

2.5.2. Necking during slab detachment

Necking occurs when a stiff layer with non-linear viscous rheology and its weak matrix are extended in layer-parallel direction or shortened in layer-normal direction (Kidan and Cosgrove, 1996; Ramberg, 1955; Smith, 1977). Various geological structures on different scales are likely (at least to some extent) the result of necking (e.g. pinch-and-swell structure, extensional basins, detached/thinned slabs) (Heuret and Lallemand, 2005; Schmalholz, 2011; Tamaki and Honza, 1991). A necking instability occurs only in layers that exhibit a non-linear viscous rheology, for example power-law viscous (Smith, 1977).

As an example for necking we show cylindrical and full 3-D simulations for detaching slabs. Slab detachment implies that the negative buoyancy of a subducting slab can be sufficiently large to trigger the detachment of slab portions and has been the focus of few numerical studies (Burkett and Billen, 2011; Capitanio and Replumaz, 2013; van Hunen and Allen, 2011; von Tscharnier *et al.*, 2014).

We present here 2-D (cylindrical 3-D) and 3-D simulations for the necking of a detaching slab.

Cylindrical necking of a detaching slab

To test the accuracy of the 3-D algorithm PINK-3D, a 3-D cylindrical simulation with only one element in the lateral direction was performed and compared with the results of a 2-D simulation (Schmalholz, 2011). The results of the 2-D simulations have been successfully benchmarked with results of several other algorithms (Thieulot *et al.*, 2014). The model domain is a rectangular box and consists of a vertically oriented rectangular layer (mimicking the slab) of power-law viscous fluid which is attached to an overlying horizontal layer with identical material properties (mimicking the non-subducted lithosphere). The rest of the model is filled by linear viscous fluid (mimicking the mantle). The boundary conditions are free slip at all boundaries. The model configuration used for the cylindrical slab detachment simulations is given in Schmalholz (2011). We use a density difference of $\Delta\rho = 150 \text{ kg.m}^{-3}$, a viscosity coefficient of $\eta_0^s = 2.37 \times 10^{11} \text{ Pa.s}^{1/n}$ and a power-law stress exponent of $n^s = 4$ for the slab and a viscosity coefficient of $\eta_0^m = 10^{21} \text{ Pa.s}$ and a power-law stress exponent of $n^m = 1$ (i.e. linear viscous flow) for the mantle. The model dimensions are given by 500km x 35km x 670km. The layer thickness is 80 km. The numerical resolution for the cylindrical 3-D simulation was 19 x 1 x 31 where the mesh is horizontally and vertically finer around the detaching slab (ca. 4.5km around the slab and 17.5 km node spacing elsewhere). The resolution in x- and y- direction is the same as we use for the full 3-D simulations. The geometric evolution and the distribution of effective viscosity for the 2-D and cylindrical 3-D results are given in figure 2.8. The effective viscosity distribution and the slab geometry agree between the 2-D and cylindrical 3-D simulations. In Figure 2.9 we also compare the evolution of minimal slab thickness and maximal slab length with time, and the results of the 2-D and 3-D algorithms also agree. Therefore, the applied 3-D resolution is sufficient to yield accurate results.

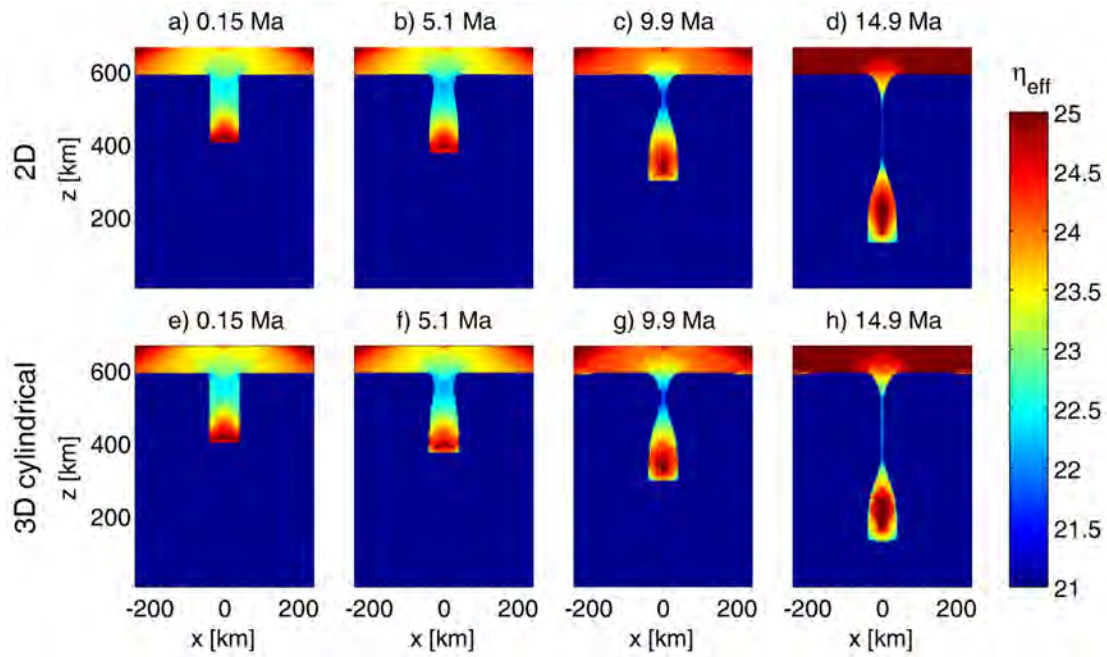


Figure 2.8: Comparison of the results of a 2-D simulation (a-d) with the results of a lower-resolution 3-D cylindrical simulation (e-h) for different times (in Ma). For both models we use a density difference of $\Delta\rho = 150\text{kg.m}^{-1}$, a viscosity coefficient of $\eta_0 = 2.37 \times 10^{11}\text{Pa.s}^{1/n}$ and a power-law stress exponent of $n = 4$ for the layer, a viscosity coefficient of $\eta_0 = 10^{21}\text{Pa.s}$ and a power-law stress exponent of $n = 1$ (i.e. linear viscous flow) for the matrix. The colors show the distribution of the effective viscosity $\log_{10}\eta_{\text{eff}}$ in Pa.s. 2-D and 3-D results agree well.

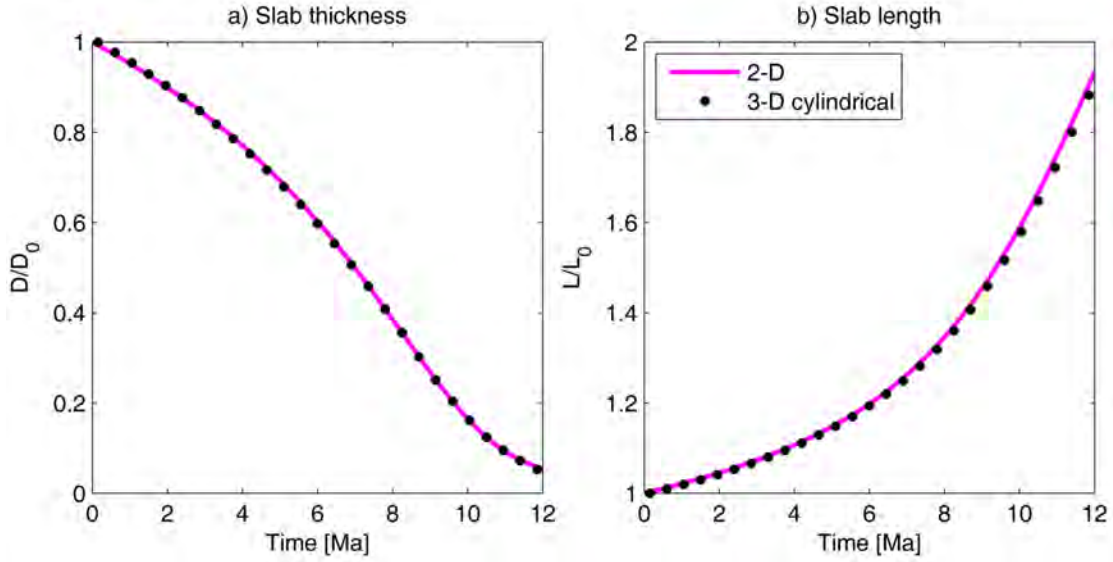


Figure 2.9: Comparison of the time evolution of a) the dimensionless slab thickness and b) the dimensionless slab length resulting from a 2-D simulation and from a 3-D cylindrical simulation. The slab thickness, D , and slab length, L , are normalized by their initial values (D_0 and L_0 , respectively).

3-D necking of a detaching slab

For the 3-D simulation the dimensions of the model box are 250 km x 280 km x 670 km. The overlying lithosphere has a thickness of 80 km whereas the slab has a thickness of 40 km in x- and y-direction assuming that only one symmetric quarter of the 3-D simulation is considered whereby the symmetry planes are perpendicular to the x- and y-direction and cut the slab in four identical parts (i.e. true slab thickness is 80 km in both horizontal directions). The slab has an initial length of 187.5 km. We use a density difference of $\Delta\rho = 150 \text{ kg.m}^{-3}$, a viscosity coefficient of $\eta_0^s = 2.37 \times 10^{11} \text{ Pa.s}^{1/n}$ and a power-law stress exponent of $n^s = 4$ for the layer and a viscosity coefficient of $\eta_0^m = 10^{21} \text{ Pa.s}$ and a power-law stress exponent of $n^m = 1$ (i.e. linear viscous flow) for the matrix.

Figure 2.10 shows the 3-D geometric evolution where the colors on the material interface indicate the effective viscosity within the slab. The thinning is localized at the top of the slab due to the occurrence of a necking instability in both horizontal directions. The effective viscosity of the slab is reduced the strongest where it is thinned.

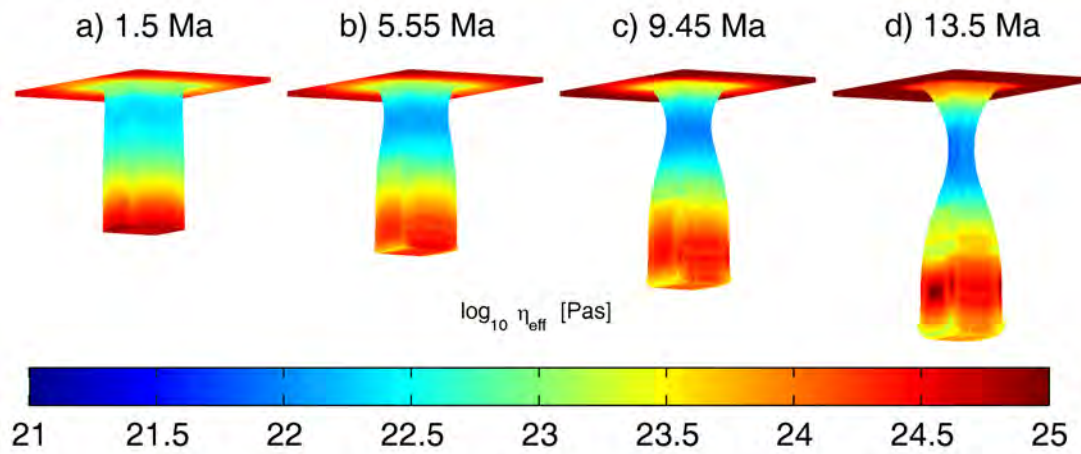


Figure 2.10: Evolution of the 3-D geometry of a detaching slab after 1.5, 5.55, 9.45 and 13.5 Ma. The colors on the slab surface indicate the effective viscosity of the slab at its surface.

Figure 2.11 shows the distribution of the second invariant of strain rate tensor on the material interface after 1.5, 5.55, 9.45 and 13.5 Ma in time as well as deformed circles with an initial diameter of $d = 12$ km. The circles were deformed using interpolated nodal velocities.

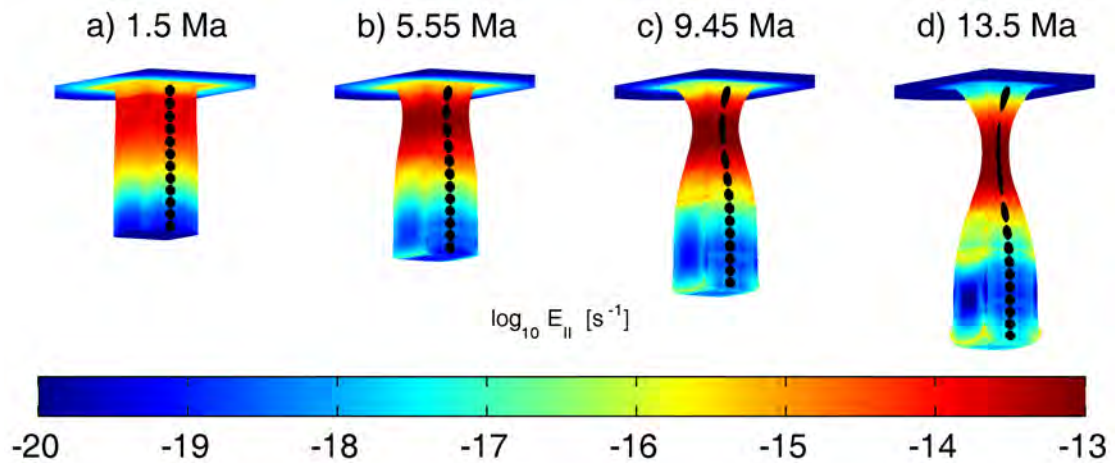


Figure 2.11: Evolution of the 3-D geometry of a detaching slab after 1.5, 5.55, 9.45 and 13.5 Ma. The colors on the slab surface indicate the second invariant of the strain rate tensor. The deformed circles on the slab surface indicate finite strain. The circles had initially a diameter of 12 km and have been deformed with the interpolated nodal velocities.

2.5.3. Fold nappe formation

Fold nappes are recumbent folds with amplitudes usually exceeding 10 km, and they have been formed presumably by ductile shearing (Bauville *et al.*, 2013; Dietrich and Casey, 1989; Epard and Escher, 1996; Ramsay *et al.*, 1983). Fold nappes often exhibit a constant sense of shearing and a non-linear increase of shear strain from their normal to their overturned limb. The Morcles nappe is a typical fold nappe, and is located in the Helvetic nappe system of the Western Swiss Alps. The Morcles nappe is a result of layer-parallel contraction and shearing (Ramsay, 1981). It has been deformed together with its underlying crystalline basement (the Mont Blanc massif). The crystalline basement also exhibits a significant amount of ductile deformation (Escher *et al.*, 1993). The sediments forming the Morcles nappes can be to first order separated into mechanically strong carbonates and mechanically weak shale-rich units (Pfiffner, 1993). Several geological studies suggest that the sediments that now form the Morcles nappe have been deposited during the Mesozoic in a half graben that was generated due to extension during the formation of the Alpine Tethys (Epard, 1990). During the compression and shortening the massive limestones were folded, which generated buckle-folds in the limestones especially in the normal limb. During the shortening the basement deformed to a large extent by ductile deformation and formed a mullion structure.

The Morcles nappe in the western part of Switzerland is tectonically separated by the Rawil depression from the more eastern Doldenhorn nappe, which is also a fold nappe but with significantly more localized deformation at its base (Steck *et al.*, 1999). A possible explanation for this stronger localization is that the weak basal sediments in the half graben deposits forming now the Doldenhorn nappe have been thinner than the sediments in the half graben deposits forming the Morcles nappe (Pfiffner, 2011). There are (to the best of our knowledge) no 3-D numerical simulations that investigated the dynamics of fold nappe formation and combined basement-cover deformation with a laterally varying half graben thickness. We study first the formation of fold nappes during half graben shortening with a 3-D cylindrical simulation and then with a 3-D simulation with laterally varying half graben thickness.

Cylindrical fold nappe formation

All geometrical and material parameters are given in dimensionless numbers using the thickness of the competent sedimentary layers H , the matrix viscosity η_M and background strain rate $\dot{\epsilon}_B$ as characteristic parameters. The model configuration for the cylindrical simulation consists of a half graben that is formed by material with a viscosity of $\eta_B = 200$ and a power-law stress exponent of $n = 1$ which mimics the basement. The half graben is filled with layers of different effective viscosity which mimic the sediments. The competent layers have a viscosity coefficient of $\eta_L = 100$ and a power-law stress exponent of $n_L = 3$. The surrounding material (matrix) has a viscosity of $\eta_M = 1$ and a power-law stress exponent of $n_M = 3$. The mechanically strong and weak layers represent limestones and shales, respectively. The model box has an initial length of $L_x = 100$ and a total height of $H_{Model} = 17$ whereas the thickness of each of the competent sedimentary layers is $H = 1$ and the maximal thickness of the half graben is $D = 4$. The cylindrical model consists of only one element in the third direction that is parallel to the cylindrical axis. The boundary conditions are free slip on the bottom, the left, the front and the back boundary ($z = 0, x = 0, y = 0, y = L_y$, where L_y is the model width in y-direction). Boundary velocities are prescribed at the right boundary ($x = L_x$) and at the top boundary ($z = H_{Model}$) to generate horizontal pure shear shortening and vertical extension. The layers are initially perfectly horizontal and folding initiates around the contact between layers and basement. With our numerical method we can accurately follow the layer geometry with the Lagrangian mesh during the initial stages of folding. This is important because during this initial stage the folding instability is strongest and the fold wavelength is selected. In contrast, the material interface that defines the bottom of the half graben crosses the individual finite elements because this interface does not develop an instability (Fig. 2.12a and c). The re-meshing is performed as soon as the fold amplitude of the competent sedimentary layer has significantly grown. Figure 2.12 shows the distribution of effective viscosity and the FE mesh (elements) for two simulations with different numerical resolution for the last time step before re-meshing (Fig. 2.12a and c) and the first time step after re-meshing (Fig. 2.12b and d). The numerical resolution is $62 \times 1 \times 22$ and $180 \times 1 \times 37$ for the low and high resolution simulation, respectively. The resolution is locally increased in x-direction around the contact point of the competent sedimentary layers with the basement and in z-direction around the competent layers to accurately resolve the initial folding process. The distribution of the effective viscosity in the layer for the time step before re-meshing is smooth and indicates the hinges and limbs of the developing folds, that is, the fold

wavelength has been selected. For the time step after re-meshing the low resolution simulation shows a less smooth viscosity distribution, especially inside the competent sedimentary layers (Fig. 2.12b).

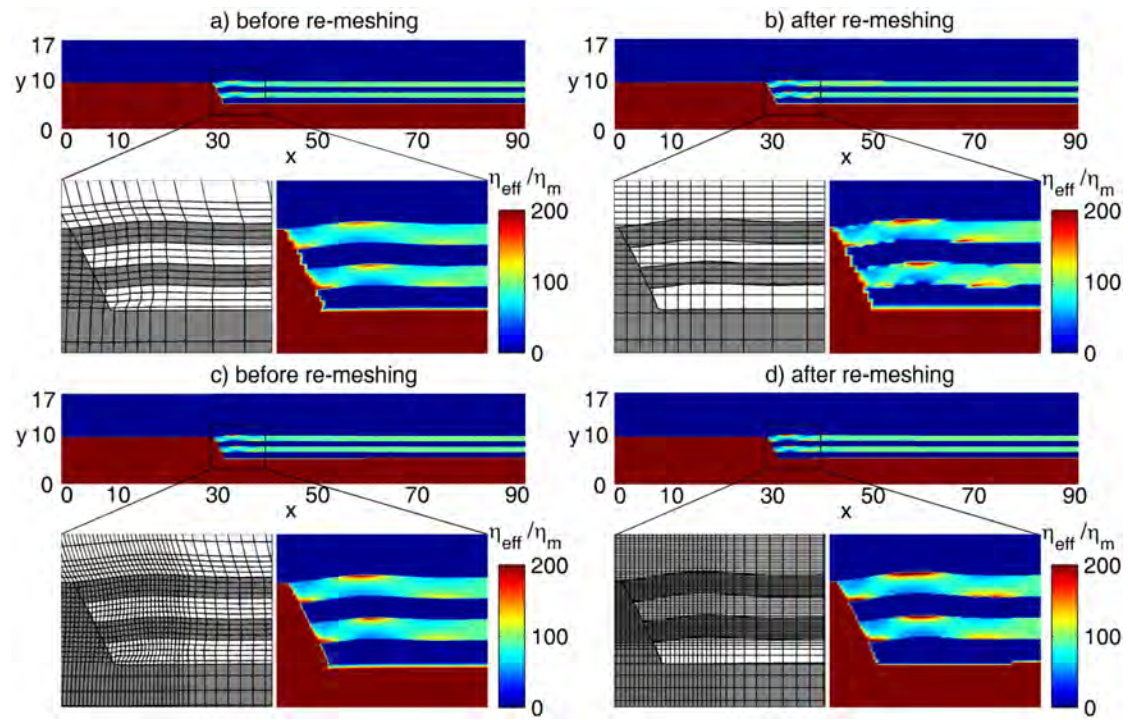


Figure 2.12: Numerical results of two 3-D cylindrical simulations for the fold nappe model configuration (see text) before and after re-meshing. The two layers have a power-law viscous rheology. The colors indicate the distribution of the dimensionless effective viscosity. A zoom into the FE mesh and into the effective viscosity distribution is displayed for two simulations with different resolution (a and c). The results are displayed for each simulation just before re-meshing (a and c) and directly after re-meshing (b and d).

Figure 2.13 shows the geometrical evolution of the fold nappe for 13, 22 and 49 % bulk shortening. The colors indicate the distribution of the second invariant of stress tensor that is given in dimensionless form and has been normalized by the product of the matrix viscosity η_M and the background strain rate $\dot{\epsilon}_B$. Figure 2.13d shows a zoom of the fold nappe geometry after 49% bulk shortening and the direction of the longest axis of the finite strain ellipsoids (which is frequently similar to the orientation of the schistosity). Due to the layer parallel compression

the competent sedimentary layers are first buckled and then sheared over the basement to form a recumbent fold nappe with an overturned limb.

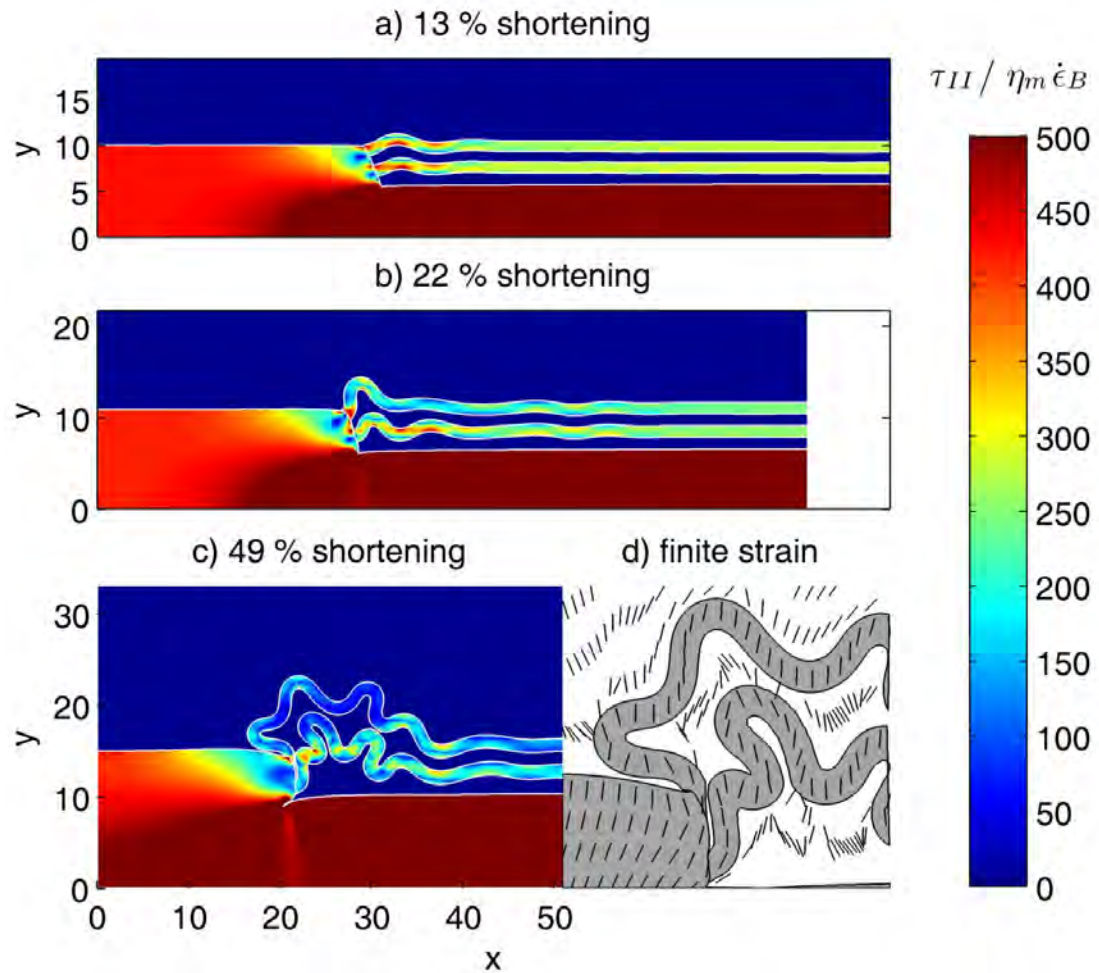


Figure 2.13: Geometrical evolution for large-strain fold nappe formation for 13, 22 and 49% bulk shortening (a-c). Results have been calculated with the 3-D code with only one FE in the third dimension. The colors indicate the second invariant of the stress tensor (normalized by the product of matrix viscosity η_M and background strain rate $\dot{\epsilon}_B$). The competent sedimentary layers are first buckled and then sheared over the basement to form a recumbent fold nappe. d) Zoom into the fold nappe geometry after 49% bulk shortening. The black lines indicate the direction (not magnitude) of the longest axis of the finite strain ellipsoid.

Fold nappe formation with laterally varying half graben thickness

In order to study fold nappe formation with laterally varying half graben thickness, a 3-D model was configured in which the thickness of the competent layers is constant laterally, but the thickness of the weak sediments below the layers was varying laterally. This configuration represents sedimentary layers that rest in a half graben with laterally varying total thickness. The dimensionless size of the model box is $100 \times 75 \times 25$ where the thickness of one competent layer is 1. The dimensionless viscosity of the basement, the competent layers and the matrix are $\eta_B = 200$, $\eta_L = 100$ and $\eta_M = 1$, respectively. All materials are characterized by linear viscous flow ($n = 1$). The half graben depth varies from 3.2 to 12.8. The boundary conditions generate shortening in the x -direction, extension in the z -direction and no deformation in the y -direction. Free slip applies to all boundaries that do not move. The numerical resolution is initially $38 \times 47 \times 10$ where the FE mesh is locally refined around the point of contact between the basement and the competent sedimentary layers and the deepest point of the half graben in x -direction and around the competent layers in z -direction. Similar as for the cylindrical simulations we follow the initial layer geometry with the FE mesh to accurately resolve the low amplitude folding, whereas the material interface between the basement and the matrix crosses individual elements. The results are given in figure 2.14 where the colors on the sides represent the second invariant of stress tensor for the basement and the competent layers and the finite strain is visualised by the blue ellipsoids for the top competent layer for 31% and 44% shortening in x -direction. The finite strain ellipsoids display the strain field and are calculated from the numerically computed velocity field using a tensor for the incremental deformation gradient and the Cauchy-Green tensor to determine the principal strain axes as described for the 2-D case by Frehner and Schmalholz (2006). For both amounts of shortening three different views of the model are given. The whole model is shown in figure 2.14a and d, in the subplots b and e the model was cut perpendicular to the y -direction at $y = 30$ and for the subplots c and f the model was cut perpendicular to the x -direction at $x = 39$ and was rotated. During the shortening in the x -direction the competent sedimentary layers are sheared over the basement and form a fold nappe with an overturned limb and a high amplitude where the initial half graben was initially deepest. Towards the shallower half graben the fold amplitude decreases. In the same time as the formation of the fold takes place the material interface between the basement and the matrix forms a cusbate-lobate structure (mullion). The stress in the basement is highest where the tip of the cusbate-lobate structure is located.

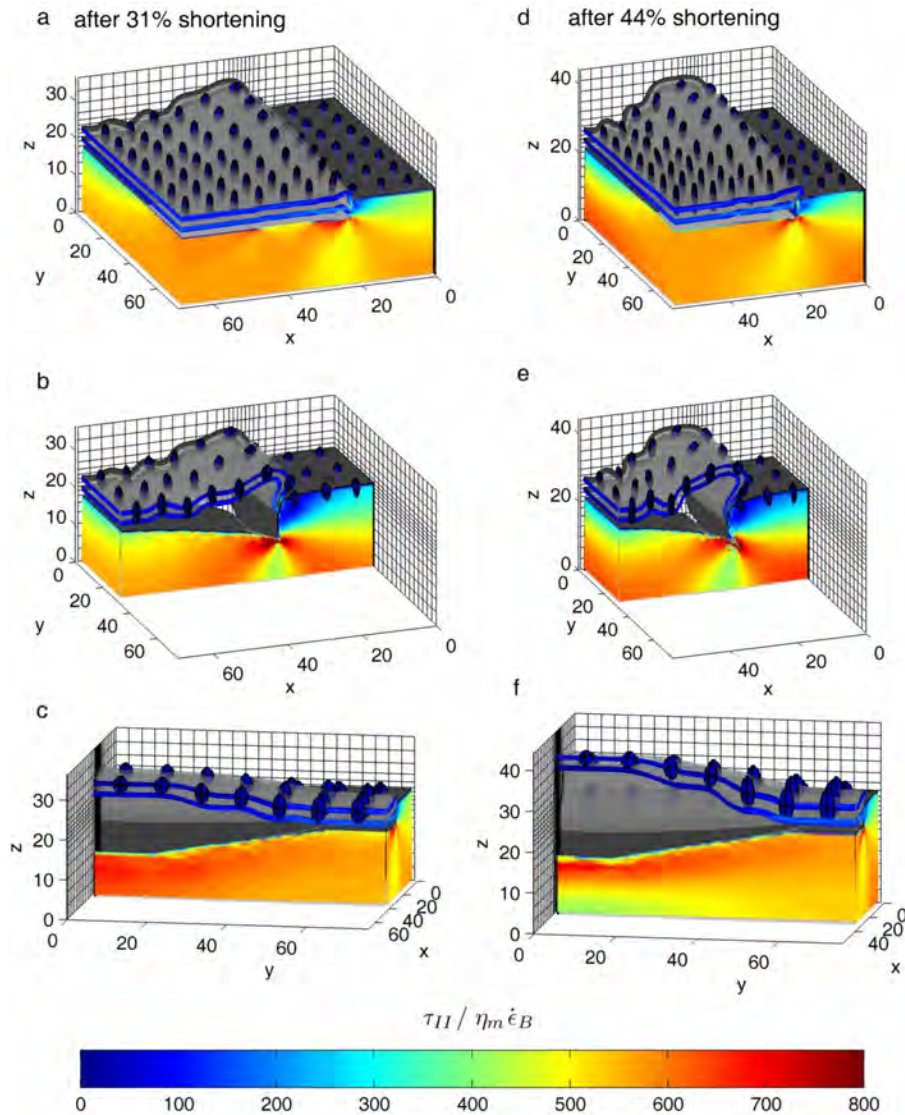


Figure 2.14: Results for the 3-D fold nappe simulation for 31% shortening in x -direction (a-c) and 44% shortening in x -direction (d-f). The fold nappe geometry, the finite strain ellipsoids and the second stress invariant, τ_{II} , within the basement and the sedimentary layers are represented by the grey surface, the blue ellipsoids and the colors, respectively. τ_{II} is normalized by the product of matrix viscosity η_M and background strain rate $\dot{\epsilon}_B$. Subplots a) and d) show the full model whereas the subplots b) and e), and c) and f) represent the model which is cut perpendicular to the x - and y -direction, respectively.

Figure 2.15 shows deformed circles on the layer-matrix and basement-matrix interface after 54% bulk shortening in x-direction. The circles have an initial dimensionless diameter of $d/H = 2$ and are deformed using interpolated nodal velocities. The colors indicate the dimensionless topography of the material interfaces. Figure 2.15 shows a significant lateral variation in geometry and strain that is caused by the initial lateral variation of the half graben thickness. The fold axis of the fold nappe is not horizontal and straight, but undulates and also plunges towards the side with the initially shallower half graben because there the topography of the fold nappe is smaller.

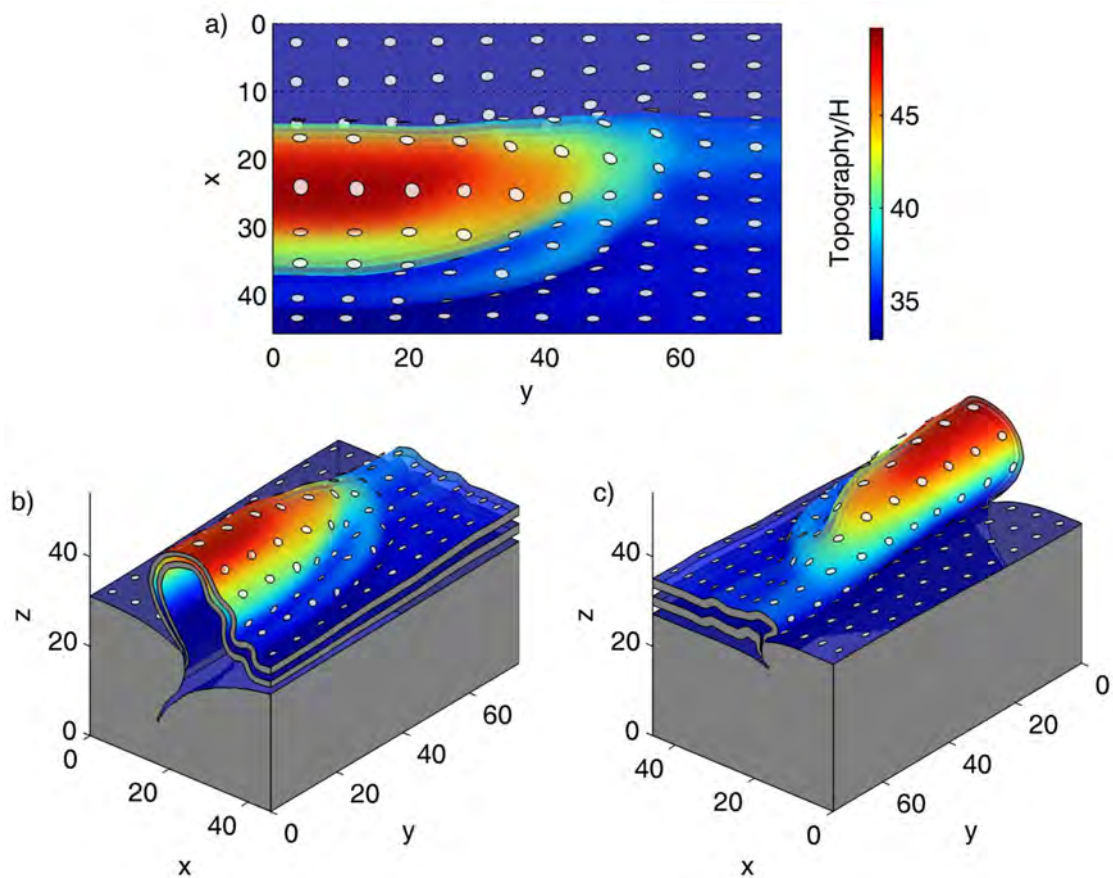


Figure 2.15: Deformed circles on the layer-matrix and basement-matrix interface indicate finite strain after 54% bulk shortening of the fold nappe simulation. The initial circles have been deformed with the interpolated nodal velocities. The colors on the material interface indicate the dimensionless topography of the material interfaces (normalised by layer thickness H).

2.6. Discussion

We showed that the presented algorithm PINK-3D with a deformable Lagrangian mesh can accurately resolve small geometrical perturbations on material interfaces and reproduce the analytical solutions for several hydrodynamic instabilities (appendix Fig 2.2 and 2.3). Furthermore, during large strain deformation the coordinates of the material interface that cross individual elements are deformed together with the deforming Lagrangian FE mesh, and the material interface deformation is therefore consistent with the applied numerical FE approximation. It is hence not necessary to interpolate nodal velocities on the interface coordinates in order to advect the interface coordinates. Moreover, the velocities around material interfaces with strongly varying viscosities are accurate also if the interfaces cross individual finite elements (Fig. 2.3). Because of the before mentioned features, the presented numerical algorithm is suitable to simulate structures that emerge from hydrodynamic instabilities, and also to model the large strain deformation of these structures. During the low-amplitude stages of the instability the material interfaces are accurately resolved and followed by a Lagrangian FE mesh, because during the low-amplitude stage the deformation is most sensitive to the interface geometry and intra-layer stress distribution. The high-amplitude stages are less sensitive to interface geometry and large strain deformation is simulated with re-meshing. The numerical movement of the material interface and nodal coordinates can be made more accurate, if higher order time integration schemes are applied, such as Runge-Kutta.

With PINK-3D it is possible to use model configurations in which some material interfaces cross individual elements of the initial FE mesh whereas other material interfaces follow exactly the initial FE mesh. This feature is useful for the presented fold nappe simulations in which the more stable basement-sediment interface was crossing individual elements and the unstable (due to buckling) layer boundaries followed exactly the FE mesh in order to accurately resolve the initial stages of buckling (Fig. 2.14).

The re-meshing test which was performed with different re-meshing scenarios for Rayleigh-Taylor diapirism and power-law viscous single-layer folding has shown the importance of an initial Lagrangian mesh to accurately follow the initial geometrical perturbations on the material interfaces. The test further shows the importance of the choice for the first re-meshing time step that should be performed not until the amplitude of the material interface is significant, that is, not until the wavelength of the emerging structure has been selected (Fig. 2.5). Our method

is suitable to model the low-amplitude instabilities accurately and the resolution required for a certain accuracy is presumably considerably smaller than the required resolution for an Eulerian FEM in combination with a particle-in-cell scheme (FE-PIC) (Moresi *et al.*, 2007; Thielmann *et al.*, 2014).

The presented 3-D results show that the applied algorithm yields smooth stress fields in folded material for viscous and viscoelastic fluids (Fig. 2.6). Furthermore, the algorithm provides smooth viscosity fields within a material after several re-meshing steps (Fig. 2.8). Hence, the presented algorithm PINK-3D is useful, if certain quantities such as stress, strain or viscosity have to be calculated on deformed 3-D surfaces.

Since PINK-3D is written in Matlab (i.e. the algorithm is not in parallel) other numerical algorithms may be much faster. Therefore, it may be of interest to translate the presented FE algorithm to an other programming language as for example C++ or Fortran. Until now, we did not implement any interpolation of the stored elastic stress between the old and new mesh. Therefore, the elastic or viscoelastic model can currently only be used without re-meshing.

The numerical algorithm is currently not optimised for memory usage and computational speed. The advantage of the algorithm is that it can be run on a standard workstation with MATLAB without the need of installing any additional libraries. Installing the MATLAB-related sparse package (<http://faculty.cse.tamu.edu/davis/suitesparse.html>) allows using several faster functions (e.g. sparse or cholmod). The MATLAB-based code PINK-3D is available online as supplementary material. The available code is configured to calculate the growth rate for 3-D single-layer folding (see appendix B, Fig. 2.3).

2.7. Conclusions

The presented 3-D FE algorithm PINK-3D combines a deformable Lagrangian mesh and a material interface technique with re-meshing, and can handle a power-law viscoelastic rheology. The algorithm is suitable to model structures that emerge due to hydrodynamic instabilities caused by large and sharp contrasts in mechanical strength and density between different rock units. The Lagrangian formulation is suitable to accurately resolve the small geometrical perturbations

of the material interfaces that control the instabilities, and the re-meshing is suitable to simulate the large-strain evolution of the structures which emerge from these instabilities.

The code has been successfully tested with various 2-D and 3-D analytical solutions for hydrodynamical instabilities such as 2-D Rayleigh-Taylor diapirism, power-law viscous single-layer folding and necking, 3-D Rayleigh Taylor diapirism and 3-D single-layer folding. A comparison with a 2-D analytical solution for a compressed viscous inclusion shows that the numerical velocities are accurate also for the case when material interfaces cross individual elements. The comparison also showed that increasing the number of integration points in elements that are crossed by a material interface does not increase the numerical accuracy.

The presented algorithm PINK-3D is especially suitable to exactly follow material interfaces in 3-D for large strains, because (i) the interface-points on the material interface are accurately moved together with the deforming Lagrangian finite element mesh, and (ii) the numerically calculated velocities are accurate also for elements that include integration points with strongly varying material properties, that is, for elements that are crossed by material interfaces after re-meshing.

The 3-D code is particularly useful to quantify and visualize quantities such as stress, strain rate, effective viscosity or finite strain on deformed material interfaces. Finite strain can be visualised either by finite strain ellipsoids or by passively deformed initial circles on the material interfaces. Such quantification of finite strain is useful to better understand the 3-D evolution of processes such as necking and folding which control to a large extent the evolution of geodynamic processes such as slab detachment or fold nappe formation. In nature, these processes often exhibit a significant 3-D deformation and the resulting structures often exhibit a complicated 3-D geometry. Hence, 3-D numerical models are required to better understand these processes and interpret the observed 3-D data and geometry.

2.8. Appendix A: Numerical methodology

The governing equations are rearranged using some suitable organized matrices and vectors:

$$\nabla^T \cdot \mathbf{v} = 0 \quad (2.31)$$

$$\mathbf{B}^T \boldsymbol{\tau}^{k+1} = \mathbf{F}_G \quad (2.32)$$

$$\boldsymbol{\tau}^{k+1} = -p\mathbf{m} + \mathbf{D}\dot{\boldsymbol{\epsilon}} + S(\boldsymbol{\tau}^k + \Delta t\mathbf{C}) \quad (2.33)$$

$$\dot{\boldsymbol{\epsilon}} = \mathbf{B}\mathbf{v} \quad (2.34)$$

where $\boldsymbol{\tau}^k$, $\boldsymbol{\tau}^{k+1}$, ∇ , \mathbf{v} , $\dot{\boldsymbol{\epsilon}}$ and \mathbf{C} are vectors containing the components of the symmetric deviatoric stress tensor from the old and current time step (indicated by k and $k+1$), the Nabla operator, the velocity vector, a vector containing the components of the symmetric strain rate tensor and a vector containing the Jaumann correction terms. $\boldsymbol{\tau}^k$, ∇ , \mathbf{v} , $\dot{\boldsymbol{\epsilon}}$, \mathbf{m} , \mathbf{F}_G , \mathbf{B} , \mathbf{D} and \mathbf{C} are defined using the Voigt notation as:

$$\boldsymbol{\tau}^k = \begin{pmatrix} \tau_{xx}^k \\ \tau_{yy}^k \\ \tau_{zz}^k \\ \tau_{xy}^k \\ \tau_{yz}^k \\ \tau_{xz}^k \end{pmatrix}, \nabla = \begin{pmatrix} \frac{\partial}{\partial x} \\ \frac{\partial}{\partial y} \\ \frac{\partial}{\partial z} \end{pmatrix}, \mathbf{v} = \begin{pmatrix} v_x \\ v_y \\ v_z \end{pmatrix}, \dot{\boldsymbol{\epsilon}} = \begin{pmatrix} \dot{\epsilon}_{xx} \\ \dot{\epsilon}_{yy} \\ \dot{\epsilon}_{zz} \\ \dot{\epsilon}_{xy} \\ \dot{\epsilon}_{yz} \\ \dot{\epsilon}_{xz} \end{pmatrix}, \mathbf{m} = \begin{pmatrix} 1 \\ 1 \\ 1 \\ 0 \\ 0 \\ 0 \end{pmatrix}, \mathbf{F}_G = \begin{pmatrix} 0 \\ 0 \\ \rho g_z \end{pmatrix} \quad (2.35)$$

$$\mathbf{B} = \begin{pmatrix} \frac{\partial}{\partial x} & 0 & 0 \\ 0 & \frac{\partial}{\partial y} & 0 \\ 0 & 0 & \frac{\partial}{\partial z} \\ \frac{\partial}{\partial y} & \frac{\partial}{\partial x} & 0 \\ 0 & \frac{\partial}{\partial z} & \frac{\partial}{\partial y} \\ \frac{\partial}{\partial z} & 0 & \frac{\partial}{\partial x} \end{pmatrix}, \mathbf{D} = \eta_{eff} \begin{pmatrix} \frac{4}{3} & \frac{-2}{3} & \frac{-2}{3} & 0 & 0 & 0 \\ \frac{-2}{3} & \frac{4}{3} & \frac{-2}{3} & 0 & 0 & 0 \\ \frac{-2}{3} & \frac{-2}{3} & \frac{4}{3} & 0 & 0 & 0 \\ 0 & 0 & 0 & 1 & 0 & 0 \\ 0 & 0 & 0 & 0 & 1 & 0 \\ 0 & 0 & 0 & 0 & 0 & 1 \end{pmatrix}, \mathbf{C} = \begin{pmatrix} C_{xx} \\ C_{yy} \\ C_{zz} \\ C_{xy} \\ C_{yz} \\ C_{xz} \end{pmatrix} \quad (2.36)$$

Combining the equations (2.31) to (2.34) the stress and strain rate vector can be eliminated. This leads to the mixed velocity-pressure formulation for power-law viscoelastic flow:

$$\mathbf{B}^T \mathbf{D} \mathbf{B} \mathbf{v} + \mathbf{B}^T S \tau^k - \mathbf{B}^T S \Delta t \mathbf{C} - \mathbf{B}^T \mathbf{m} p = \mathbf{F}_G \quad (2.37)$$

The incompressibility is not directly implemented in the finite element code. Therefore, the incompressibility equation or mass balance equation is changed to:

$$\frac{Dp}{Dt} = \frac{p^{k+1} - p^k}{\Delta t} = -K(\nabla^T \cdot \mathbf{v}) \quad (2.38)$$

assuming a compressible material and a converging solution towards an incompressible material. The incompressibility is reintroduced into the model during the Richardson iterations. Therefore, we end up with four equations to solve for four unknowns (three components of the velocity vector and the pressure). Now the equations are discretized using the FE method and 27-node hexahedral Q2P1 elements with linear discontinuous shape functions for pressure and quadratic shape functions for velocities (Bathe, 1996).

In the first step of the discretization of equation (2.37) the velocity shape functions are applied as weighting functions (Galerkin approach). At the same time the integration over the whole FE is carried out to get the weighted residual formulation:

$$\int_{\Omega} \mathbf{N}_v^T \mathbf{B}^T \mathbf{D} \mathbf{B} \mathbf{v} dV - \int_{\Omega} \mathbf{N}_v^T \mathbf{B}^T \mathbf{m} p^{k+1} dV = \int_{\Omega} \mathbf{N}_v^T \mathbf{F}_G dV - \int_{\Omega} \mathbf{N}_v^T \mathbf{B}^T S \tau^k dV + \int_{\Omega} \mathbf{N}_v^T \mathbf{B}^T S \Delta t \mathbf{C} dV \quad (2.39)$$

At this point the physical values \mathbf{v} and p^{k+1} are approximated within the FEs. The FE approximation which is given in equation (2.22) and equation (2.23) can be written using vectors:

$$\mathbf{v} = \mathbf{N}_v \tilde{\mathbf{v}} \quad (2.40)$$

$$p^{k+1} = \mathbf{N}_p \tilde{\mathbf{p}}^{k+1} \quad (2.41)$$

where \mathbf{N}_v and \mathbf{N}_p are vectors containing the velocity and pressure shape functions, respectively, $\tilde{\mathbf{v}} = (v_{x1}, v_{y1}, v_{z1}, v_{x2}, v_{y2}, \dots, v_{z27})^T$ contains the velocities at each of the 27 nodes of the element and $\tilde{\mathbf{p}}^{k+1} = (p_1, p_2, p_3, p_4)^T$ contains the pressure value as well as three slopes of the linear dependency on the position in three dimensional space. \mathbf{N}_v and \mathbf{N}_p are defined as:

$$\mathbf{N}_v = \begin{bmatrix} N_{v1} & 0 & 0 & N_{v2} & 0 & 0 & \dots & N_{v27} & 0 & 0 \\ 0 & N_{v1} & 0 & 0 & N_{v2} & 0 & \dots & 0 & N_{v27} & 0 \\ 0 & 0 & N_{v1} & 0 & 0 & N_{v2} & \dots & 0 & 0 & N_{v27} \end{bmatrix} \quad (2.42)$$

$$\mathbf{N}_p = \begin{bmatrix} N_{p1} & N_{p2} & N_{p3} & N_{p4} \end{bmatrix} \quad (2.43)$$

The finite element approximation is substituted in equation (2.39), where the vectors $\tilde{\mathbf{v}}$ and $\tilde{\mathbf{p}}^{k+1}$ are not incorporated into the integration because they are independent on the x -, y - and z -position:

$$\int_{\Omega} \mathbf{N}_v^T \mathbf{B}^T \mathbf{D} \mathbf{B} \mathbf{N}_v dV \tilde{\mathbf{v}} - \int_{\Omega} \mathbf{N}_v^T \mathbf{B}^T \mathbf{m} \mathbf{N}_p dV \tilde{\mathbf{p}}^{k+1} = \int_{\Omega} \mathbf{N}_v^T \mathbf{F}_G dV - \int_{\Omega} \mathbf{N}_v^T \mathbf{B}^T S \tau^k dV + \int_{\Omega} \mathbf{N}_v^T \mathbf{B}^T S \Delta t \mathbf{C} dV \quad (2.44)$$

This can be written as:

$$\int_{\Omega} \tilde{\mathbf{B}}^T \mathbf{D} \tilde{\mathbf{B}} dV \tilde{\mathbf{v}} - \int_{\Omega} \tilde{\mathbf{B}}^T \mathbf{m} \mathbf{N}_p dV \tilde{\mathbf{p}}^{k+1} = \int_{\Omega} \mathbf{N}_v^T \mathbf{F}_G dV - \int_{\Omega} \tilde{\mathbf{B}}^T S \tau^k dV + \int_{\Omega} \tilde{\mathbf{B}}^T S \Delta t \mathbf{C} dV \quad (2.45)$$

where $\tilde{\mathbf{B}} = \mathbf{B} \mathbf{N}_v$ and $\tilde{\mathbf{B}}^T = \mathbf{N}_v^T \mathbf{B}^T$.

The same discretisation can be done for the incompressibility equation (2.16) which is first rearranged as:

$$p^{k+1} + K\Delta t \mathbf{m}^T \mathbf{B} \mathbf{v} = p^k \quad (2.46)$$

where the Nabla operator is expressed as $\nabla = \mathbf{B}^T \mathbf{m}$. The pressure shape functions are applied as weighting functions and the integration over the whole element is carried out:

$$\int_{\Omega} \mathbf{N}_p^T p^{k+1} dV + K\Delta t \int_{\Omega} \mathbf{N}_p^T \mathbf{m}^T \mathbf{B} \mathbf{v} dV = \int_{\Omega} \mathbf{N}_p^T p^k dV \quad (2.47)$$

Now, the velocities and the pressure are approximated within the FE with the FE approximation:

$$\int_{\Omega} \mathbf{N}_p^T \mathbf{N}_p dV \tilde{\mathbf{p}}^{k+1} + K\Delta t \int_{\Omega} \mathbf{N}_p^T \mathbf{m}^T \mathbf{B} \mathbf{N}_v dV \tilde{\mathbf{v}} = \int_{\Omega} \mathbf{N}_p^T \mathbf{N}_p dV \tilde{\mathbf{p}}^k \quad (2.48)$$

Equation (2.45) and equation (2.48) can be written in a more compact matrix notation:

$$\begin{bmatrix} \mathbf{K} & \mathbf{Q} \\ -K\Delta t \mathbf{Q}^T & \mathbf{M} \end{bmatrix} \begin{pmatrix} \tilde{\mathbf{v}} \\ \tilde{\mathbf{p}}^{k+1} \end{pmatrix} = \begin{pmatrix} \tilde{\mathbf{F}}_G \\ \mathbf{M} \tilde{\mathbf{p}}^k \end{pmatrix} \quad (2.49)$$

$$\mathbf{K} = \int_{\Omega} \tilde{\mathbf{B}}^T \mathbf{D} \tilde{\mathbf{B}} dV \quad (2.50)$$

$$\mathbf{Q} = - \int_{\Omega} \tilde{\mathbf{B}}^T \mathbf{m} \mathbf{N}_p dV \quad (2.51)$$

$$\mathbf{M} = \int_{\Omega} \mathbf{N}_p^T \mathbf{N}_p dV \quad (2.52)$$

$$\tilde{\mathbf{F}}_G = \int_{\Omega} \mathbf{N}_v^T \mathbf{F}_G dV - \int_{\Omega} \tilde{\mathbf{B}}^T S \tau^k dV + \int_{\Omega} \tilde{\mathbf{B}}^T S \Delta t \mathbf{C} dV \quad (2.53)$$

where round brackets denote vectors containing the nodal values of the respective variables. The integrations are performed numerically using either 27 (3^3), 125 (5^3) or 343 (7^3) integration points per element. Using discontinuous pressure shape functions allows the elimination of the pressure at the element level. The elimination leads to a system containing only the velocity unknowns:

$$\begin{aligned} \mathbf{L}\tilde{\mathbf{v}} &= \mathbf{F}_G - \mathbf{Q}\tilde{\mathbf{p}}^k \\ \mathbf{L} &= \mathbf{K} + K\Delta t \mathbf{Q}\mathbf{M}^{-1}\mathbf{Q}^T \end{aligned} \quad (2.54)$$

The values of $\tilde{\mathbf{p}}^{k+1}$ are computed during the Richardson iteration that is applied to the reduced velocity Schur complement system (Dabrowski *et al.*, 2008). The Richardson iteration is the innermost loop, nested within the power-law Piccard iteration loop. During the time-stepping stress and strain rate tensor components, pressure, effective viscosities, velocities and finite strain are calculated and saved for later visualization in the post-processing.

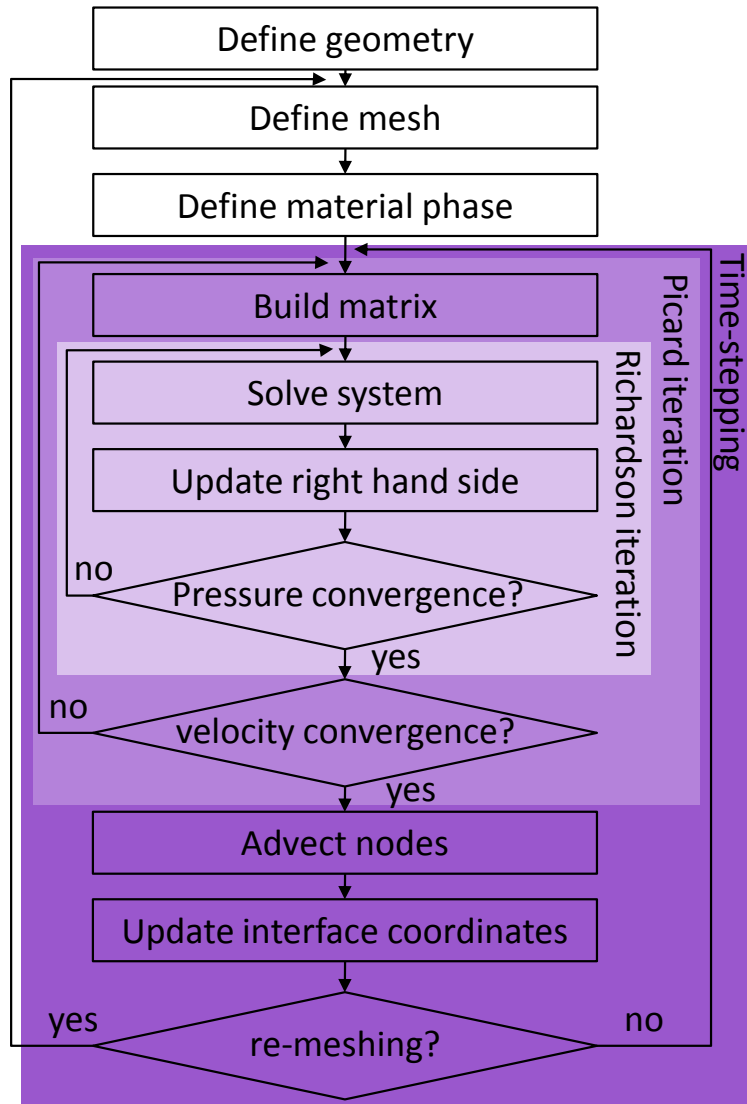


Figure 2.1: Structure of the algorithm PINK-3D.

2.9. Appendix B: Benchmarks

The 3-D numerical code has been benchmarked against various 2-D and 3-D analytical solutions and against 2-D numerical FE solutions. The 2-D FE code without gravity is described in detail

in Schmalholz *et al.* (2008) and the implementation of gravity was done as described in Burg and Schmalholz (2008). The 2-D and 3-D analytical solutions for Rayleigh-Taylor diapirism, folding and necking yield mathematical formulas for the growth rate, α , of the amplitude of geometrical perturbations of material interfaces. To compare the analytical growth rates with numerical solutions, the growth rates are calculated from the numerical results using the equation:

$$\alpha = \frac{\log \frac{A}{A_0}}{dt} \quad (2.55)$$

where A_0 and A are the initial amplitude and the numerically calculated amplitude of the numerical material interface, respectively, after one numerical time step dt . To compare the 3-D numerical results with the 2-D analytical solution and the 2-D FE solutions we use a cylindrical model configuration with only one element in the third direction (along the cylindrical axis).

2.9.1. 2-D Rayleigh-Taylor instability

In order to check the correctness of the 3-D FE code regarding gravity, the code was tested versus the 2-D analytical solution in Turcotte and Schubert (2002) for the amplitude growth rate of the Rayleigh-Taylor instability. The Rayleigh-Taylor instability describes the buoyant upwelling of relatively light material. A diapir is formed as the lighter material rises into the heavier overlying material. The analytical growth rate is given by:

$$\alpha = \frac{\Delta\rho g H \left(\frac{\lambda}{2\pi H}\right)^2 \tanh\frac{2\pi H}{\lambda} - \frac{1}{\sinh\frac{2\pi H}{\lambda} \cosh\frac{2\pi H}{\lambda}}}{4\eta \left(\frac{\lambda}{2\pi H} + \frac{1}{\sinh\frac{2\pi H}{\lambda} \cosh\frac{2\pi H}{\lambda}}\right)} \quad (2.56)$$

where λ is the wavelength of the initial sinusoidal layer perturbation, $\Delta\rho$ is the density difference, g is the gravity, b is the layer thickness and η is the viscosity. The model configuration used for the benchmark versus the analytical solution is shown in figure 2.1a. The benchmark was performed with a viscosity of $\eta = 1$ for both materials, a density difference of $\Delta\rho = 10$, a layer thickness of $H = 1$, an initial layer perturbation amplitude of $A_0 = 1.25 \times 10^{-4}$ and a varying wavelength. All parameters are given in dimensionless numbers, where the non-

dimensionalization was done taking the layer thickness H and the viscosity η as characteristic length and viscosity, respectively.

For the comparison with the 2-D FE solution (re-meshing test) we used a viscosity contrast of $R_\eta = \eta_2/\eta_1 = 10$, a density difference of $\Delta\rho = 1000$ and a power-law stress exponent of $n = 1$ (i.e. linear viscous flow) for both materials. The model dimensions are given by $H = 1$ and $\lambda = 2.56$ and we use an initial sinusoidal perturbation of $A_0 = 0.005$. The boundary conditions are free slip for all vertical boundaries and no slip for the horizontal boundaries. The model is entirely driven by gravity. The comparison of the numerical results with the analytical solution is given in figure 2.2a and shows a good agreement between the 3-D algorithm and the analytical solution.

2.9.2. 2-D folding and necking

To test the 3-D FE code for instabilities in power-law viscous flow the analytical solution for 2-D single-layer power-law folding and necking by Fletcher (1974) is used (see also Schmalholz *et al.* (2008)):

$$\alpha = -Sgn(\bar{D}_{xx}) + \frac{2n_L \left(1 - \frac{1}{R_\eta}\right) Sgn(\bar{D}_{xx})}{-1 + Q^2 \pm \sqrt{n_L - 1} \frac{(1+Q)^2 e^{ak} - (1-Q)^2 e^{-ak}}{2 \sin bk}} \quad (2.57)$$

$$R_\eta = \frac{\eta_L}{\eta_M}, q = \frac{1}{R_\eta} \sqrt{\frac{n_L}{n_M}}, a = \sqrt{1 - \frac{1}{n_L}}, k = \frac{2\pi H}{\lambda} \quad (2.58)$$

$$Sgn(\bar{D}_{xx}) = \begin{cases} 1 & , extension \\ -1 & , shortening \end{cases} \quad (2.59)$$

where η_L and η_M and n_L and n_M are the layer and matrix viscosity and power-law stress exponents, respectively. H is the layer thickness and λ is the wavelength of the initial sinusoidal layer perturbation. The positive sign in the denominator applies to a pinch-and-swell perturbation (necking) and the negative sign to a fold component. The equation for the analytical solution can, therefore, be used for all single-layer instabilities (Smith, 1977).

The model configurations used for the benchmark versus the analytical solution for folding and necking are given in figure 2.1b and c, respectively. For the benchmark with the 2-D analytical solution for single-layer power-law folding we use a viscosity contrast of $R_\eta = \eta_L/\eta_M = 50$ and power-law stress exponents of $n_L = 5$ and $n_M = 3$ for the layer and the matrix material, respectively. The layer thickness is given by $H = 1$, the total model height is $H_{Model} = 23.4$, the initial layer perturbation amplitude is $A_0 = 0.001$ and the wavelength λ is varied. The boundary conditions are free slip for the left ($x = 0$) and bottom ($y = 0$) boundary and pure shear shortening and pure shear extension for the right ($x = \lambda$) and top ($y = H_{Model}$) boundary, respectively (Fig. 2.1b). For the necking benchmark we use a viscosity contrast of $R_\eta = \eta_L/\eta_M = 20$ and power-law stress exponents of $n_L = 10$ and $n_M = 3$ for the layer and the matrix material, respectively. The layer thickness is given by $H = 1$, the total model height is $H_{Model} = 17$, the initial layer perturbation amplitude is $A_0 = 0.001$ and the wavelength λ is varied. The boundary conditions are free slip for the left ($x = 0$) and bottom ($y = 0$) boundary and pure shear extension and pure shear shortening for the right ($x = \lambda$) and top ($y = H_{Model}$) boundary, respectively (Fig. 2.1c). The benchmark results for cylindrical folding and necking versus the analytical solution are given in figure 2.2b and c, respectively. The numerical results agree with analytical solution.

For the comparison of 3-D cylindrical single-layer folding with the 2-D FE results (re-meshing test) we use a viscosity contrast of $R_\eta = \eta_l/\eta_M = 100$ and power-law stress exponents of $n_L = 5$ and $n_M = 3$ for the layer and matrix material, respectively. The layer thickness is given by $H = 1$, the total model height is $H_{Model} = 19$, the initial layer perturbation amplitude is $A_0 = 0.05$ and the wavelength is $\lambda = 11.8$, which is the dominant wavelength for the given material parameters.

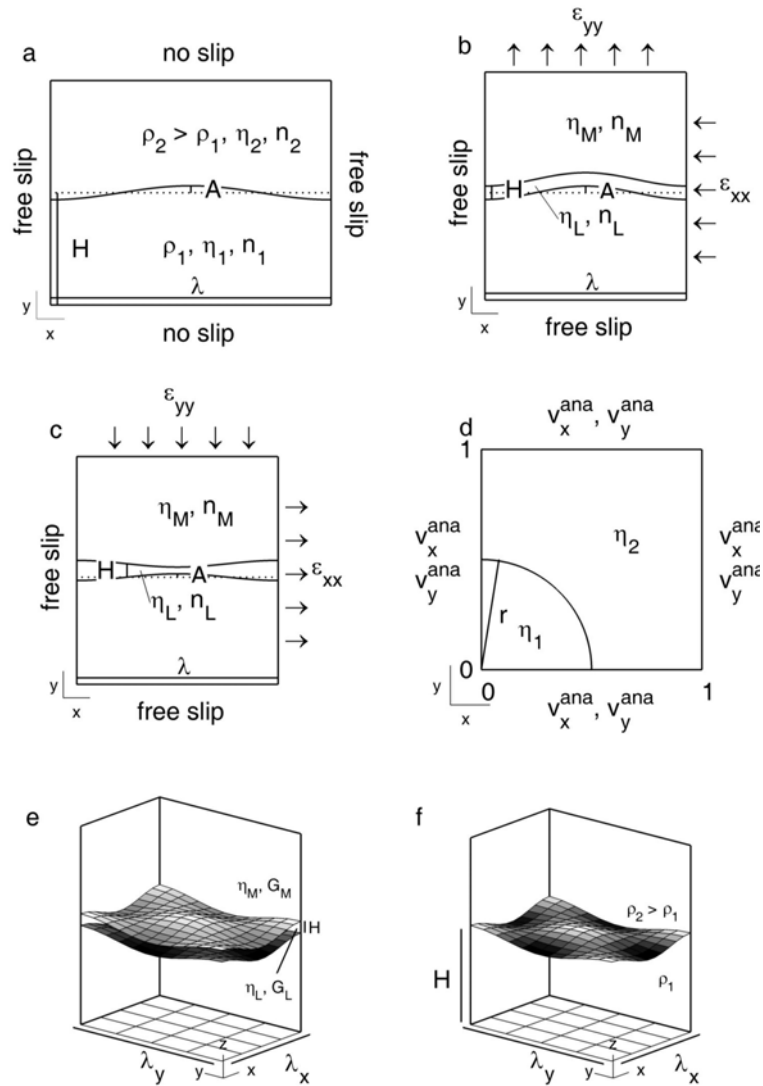


Figure 2.1: a) Model configuration for cylindrical Rayleigh-Taylor instability. b) Model configuration for cylindrical power-law single-layer folding. c) Model configuration for cylindrical power-law single-layer necking. d) Model configuration for the viscous inclusion test. e) Model configuration for 3-D single-layer folding. The boundary conditions are free slip for the $x = 0$, $y = 0$ and $z = 0$ boundaries whereas we use prescribed velocities for pure shear shortening for the two vertical boundaries and pure shear extension for the top boundary with $R_{\dot{\epsilon}} = 0.75$. f) Model configuration for 3-D Rayleigh-Taylor instability. The boundary conditions are free slip for all vertical boundaries and no-slip for the top and bottom boundary. The deformation is entirely driven by gravity.

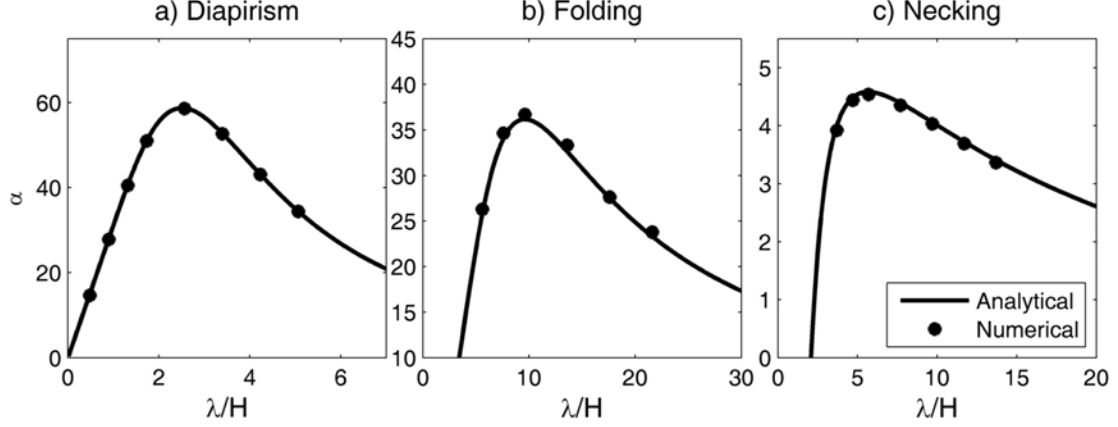


Figure 2.2: The dispersion relation for Rayleigh-Taylor diapirism (a), power-law single-layer folding (b) and power-law necking (c). The dimensionless growth rate of the initial sinusoidal layer perturbation α , is plotted versus the ratio of wavelength to layer thickness, λ/H (see text for details). The dots have been numerically calculated with the code PINK-3D for the cylindrical cases and agree well with the analytical solutions (lines).

2.9.3. 3-D single-layer folding

The 3-D FE algorithm PINK-3D has been benchmarked against the 3-D analytical thick-plate solution for single-layer folding. Fletcher (1991) showed that mechanically strong layer of thickness H with a normal-mode initial perturbation of $A(x, y) = \pm H/2 + A_0 \cos k_x x \cos k_y y$ grows exponentially with time:

$$A(x, y, t) = A_0 e^{\alpha t} \quad (2.60)$$

where A_0 is the amplitude of the initial sinusoidal layer perturbation and α is the growth rate:

$$\frac{\alpha}{-\dot{\epsilon}_z} = \frac{q}{2} \left(\frac{k_x^2}{k^2} (R_{\dot{\epsilon}} - 1) - \frac{k_y^2}{k^2} R_{\dot{\epsilon}} - 1 \right) \quad (2.61)$$

$$q = \frac{-4(1 - R_{\eta}^{-1})k}{2k(1 - R_{\eta}^{-2}) - (1 - R_{\eta}^{-1})^2 e^k + (1 - R_{\eta}^{-1})^2 e^{-k}} \quad (2.62)$$

$$k = \sqrt{k_x^2 + k_y^2}, R_{\dot{\epsilon}} = \frac{-\dot{\epsilon}_x}{\dot{\epsilon}_z}, R_\eta = \frac{\eta_L}{\eta_M} \quad (2.63)$$

where k is the total wave-number, k_x and k_y are the wave-numbers in x- and y-direction, respectively, $R_{\dot{\epsilon}}$ is the normalized strain rate of the basic-state flow in x-direction (compression positiv) and $R_\eta = \eta_L/\eta_M$ is the viscosity ratio of the layer material relative to the matrix material. The model configuration used for the benchmark versus the 3-D analytical solution is given in figure 2.1 e. The boundary conditions are free slip for the boundaries $x=0$, $y=0$ and $z=0$ and prescribed pure shear shortening in the horizontal directions for $x = \lambda_x$ and $y = \lambda_y$ and pure shear extension in the vertical direction for $z = H_{Model}$ with $R_{\dot{\epsilon}} = -\dot{\epsilon}_x/\dot{\epsilon}_z = 0.75$. We use a viscosity contrast of $R_\eta = \eta_L/\eta_M = 50$, a layer thickness of $H = 1$, a total model height of $H_{Model} = 21$ and an initial amplitude of $A_0 = 0.001$. The wavelength in x- and y-direction λ_x and λ_y are varied. All model parameters are given in dimensionless numbers using the layer thickness H , the matrix viscosity η_M and the strain rate of the basic-state flow $\dot{\epsilon}_B$ as characteristic parameters. Figure 2.3a shows the dispersion relation for 3-D single -layer folding versus the wavelength to layer thickness ratio in x- and y-direction. The subplots figure 2.3b and c show the dispersion relation for a fixed wavelength to layer thickness ratio of $\lambda_y/H = 27$ in y-direction and $\lambda_x = 13.5$ in x-direction, respectively. The numerical results agree with the analytical solution.

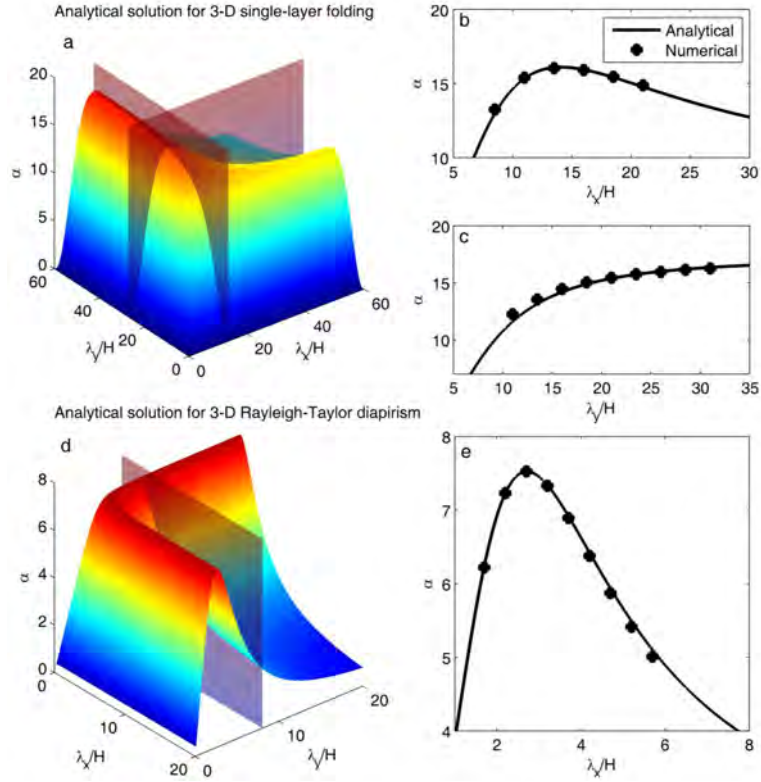


Figure 2.3: (a-c) Dispersion relation for 3-D Newtonian single-layer folding (see text for details). a) Surface plot for the 3-D analytical solution. b) Section through the 3-D solution for $\lambda_y/H = 27$. c) Section through the 3-D solution for $\lambda_x/H = 13.5$. Analytical (lines) and numerical (PINK-3D, dots) growth rates agree well. (d-e) Dispersion relation for 3-D Rayleigh-Taylor instability (see text for details). d) Surface plot for the 3-D analytical solution. e) The numerical simulations were performed along a section for $\lambda_y/H = 8$. Analytical (lines) and numerical (PINK-3D, dots) growth rates agree well.

2.9.4. 3-D Rayleigh-Taylor instability

Our 3-D FE algorithm PINK-3D was further tested versus an analytical solution for 3-D Rayleigh-Taylor instability. The amplitude growth rate for a given sinusoidal initial perturbation on the material interface can be analytically calculated using a linear stability analysis (Conrad and Molnar, 1997; Kaus and Podlatchikov, 2001; Ribe, 1998; Turcotte and Schubert, 2002).

The initial sinusoidal layer perturbation and the analytical solution are given as follows:

$$A(x, y) = A_0 \cos k_x x \cos k_y y \quad (2.64)$$

$$\alpha = \frac{Hg\Delta\rho}{4\eta} \frac{(k^2 + 2)e^{-k} - e^{-2k} - 1}{k(-2e^{-k} + e^{-2k} - 1)} \quad (2.65)$$

$$k = \sqrt{k_x^2 + k_y^2}, k_x = \frac{2\pi H}{\lambda_x}, k_y = \frac{2\pi H}{\lambda_y} \quad (2.66)$$

where A_0 is the initial amplitude, k_x and k_y are the wave number in x- and y-direction, respectively, α is the analytical growth rate, H is the layer thickness. The model thickness is divided in two by the material interface so that the total model thickness is $H_{Model} = 2H$, g is the gravity, $\Delta\rho = \rho_2 - \rho_1$ is the density difference between the upper and lower fluid, η is the viscosity for both materials (iso-viscous) and λ_x and λ_y are the wavelength of the initial perturbation in x- and y-direction, respectively. Note that the 2-D analytical solution (e.g. Turcotte and Schubert (2002)) is included as a special case if $k_y = 0$.

The model configuration for the 3-D Rayleigh-Taylor simulations is shown in figure 2.1f. For the benchmark we use a density difference of $\Delta\rho = 10$, a viscosity of $\eta = 1$ for both material, a layer thickness of $H = 1$, a total model height of $H_{Model} = 2H = 2$ and an initial layer perturbation amplitude of $A_0 = 0.001$. All model parameters were made dimensionless using the layer thickness H , the viscosity η and the background strain rate $\dot{\epsilon}_B$ as characteristic parameters. The wavelength in x-direction is varied whereas the wavelength in y-direction $\lambda_y/H = 8$. The boundary conditions are free slip for all vertical boundaries ($x = 0$, $x = \lambda_x$, $y = 0$ and $y = \lambda_y$) and no slip for the top and bottom boundaries ($z = 0$ and $z = H_{Model}$). The deformation is entirely driven by gravity. Figure 2.3d shows the dispersion relation for 3-D Rayleigh-Taylor instability. The 3-D analytical growth rate surface α is plotted versus the ratio of initial wavelength to layer thickness in both horizontal directions, that is λ_x/H and λ_y/H . Subplot 2.3e shows the dispersion relation for a fixed wavelength to layer thickness ratio in y-direction of $\lambda_y/H = 8$ which is similar to a fixed wavelength to layer thickness ratio in x-direction of $\lambda_x/H = 8$ due to symmetry. The numerical results show good agreement with the analytical solution.

2.9.5. Elasticity - elastic beam and elastic simple shear

In order to test the elasticity implementation in the 3-D FE algorithm PINK-3D, we chose two model configurations. The first is a cylindrical elastic beam in a viscous matrix under gravity. The model box has the dimensions of $10 \times 0.25 \times 10$. The elastic beam which is vertically located in the middle of the model box has a thickness of $H = 1$ and a length of $L = 5$. The viscosity is $\eta_m = 1$ and $\eta_b = 10^{13}$ for the matrix and the beam, respectively. The elastic shear modulus is $G_m = 10^{10}$ and $G_b = 10^3$ for the matrix and beam, respectively, and the density difference is $\rho_b - \rho_m = 300$. These parameters provide a beam that is effectively elastic and a matrix that is effectively viscous. All model dimensions and material parameters are given in dimensionless numbers using the thickness of the beam H , the matrix viscosity and the background strain rate as characteristic parameters. The boundary conditions are free slip for all boundaries. The results of this simulation are shown in figure 2.4 where the colors indicate the second invariant of the stress tensor. The elastic beam is deflected downward under vertical gravity (Fig. 2.4b). When the gravity is turned off, the beam deflects upwards due to the stored elastic energy and recovers the original rectangular shape which is stress free (Fig. 2.4c). A similar test is given in Gerya (2010). The test shows the reversible elastic deformation. The elastic beam recovers its original rectangular shape and stress state when the applied load is removed.

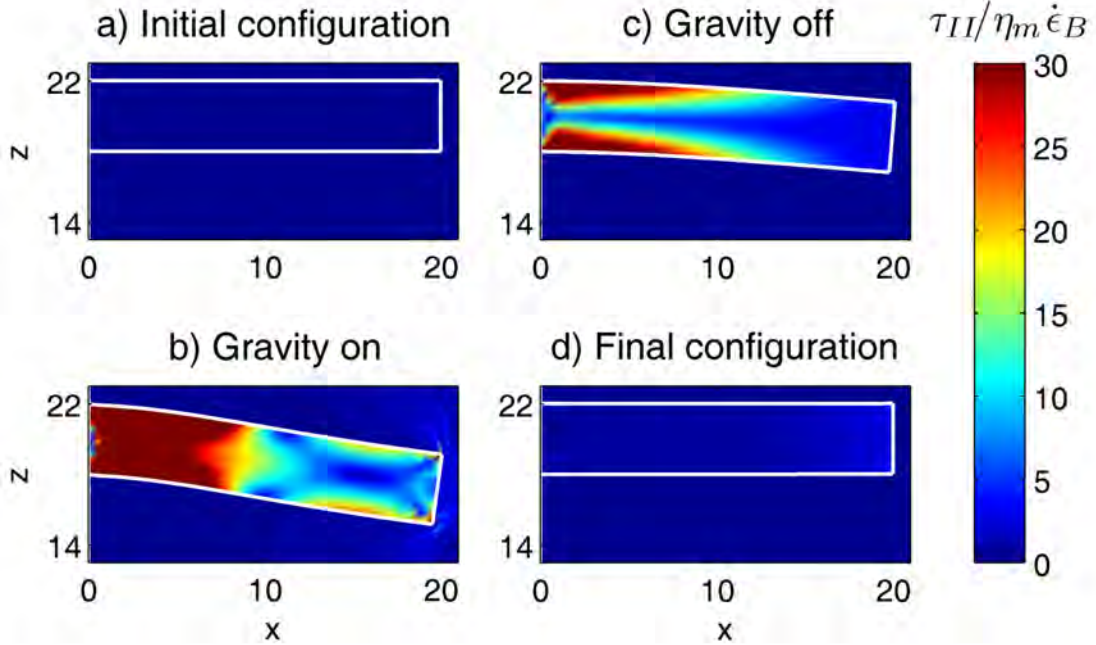


Figure 2.4: Reversible deformation of an elastic beam in a viscous matrix under gravity. a) Unstressed initial configuration (gravity off). b) Deformation of the elastic beam under gravity. c) Gravity is turned off. d) The elastic beam recovers the original rectangular shape with zero stress. Colors indicate the second invariant of the stress tensor τ_{II} .

The second model configuration uses a homogeneous cube with the dimensions $1 \times 1 \times 1$ which is deformed by simple shear. The bottom boundary is fixed (i.e. the boundary condition is no slip), the velocities on the top surface are prescribed in x -direction to generate simple shear and the top boundary is fixed in z -direction. The boundary conditions are free slip for two vertical boundaries ($y=0$ and $y=1$) and the two remaining vertical boundaries ($x=0$ and $x=1$) are free. The viscosity and the elastic shear modulus are $\eta = 10^{10}$ and $G = 1$, respectively. All model dimensions and material parameters are given in dimensionless numbers using the model length, the elastic shear modulus and the background strain rate as characteristic parameters. The results for two simulations, one with Jaumann correction and one without Jaumann correction, are given in figure 2.5 where the colors indicate the second invariant of the stress tensor. The results with the Jaumann correction show a homogeneous distribution of stress (Fig. 2.5 a-d) whereas the distribution of the second invariant of the stress tensor is inhomogeneous without the Jaumann correction and the simulation "crashes" for high strain (Fig. 2.5 e-h).

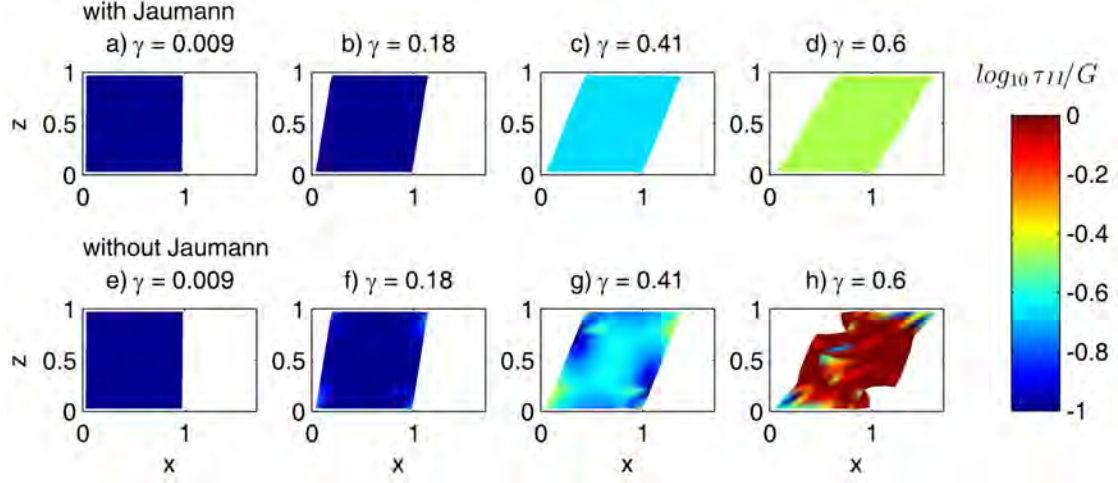


Figure 2.5: Deformation of a homogeneous cube under simple shear with Jaumann correction (a-d) and without Jaumann correction (e-h) for different amounts of bulk shear strain γ (i.e. ratio of maximal horizontal displacement to model thickness). The colors indicate the second invariant of the stress tensor τ_{II} . Without the Jaumann corrections, the stress distribution becomes inhomogeneous and the simulation crashes for high strain.

2.9.6. Viscous inclusion test - convergence test

In order to test and measure the numerical properties for an Eulerian mesh (material interface cross the individual FEs) we use the analytical solution for a 2-D viscous inclusion in pure shear (Schmid, 2003). The model domain of the viscous inclusion test is given by $\Omega = [0, 1] \times [0, 1]$. The origin of the circular viscous inclusion with a radius of $r = 0.5$ is located at $(0, 0)$. This means that we simulate only one quarter of the inclusion since the model is symmetric (figure 2.1d). The viscosity within the inclusion is defined as $\eta_1 = 10^3$ whereas the viscosity of the surrounding material is $\eta_2 = 1$. Along the model boundaries we prescribe the velocities v_x and v_y based on the analytical solution. All parameters are dimensionless using the viscosity of the matrix η_2 , the model width W and the background strain rate $\dot{\epsilon}_B$ as characteristic parameters. The model is entirely driven by the Dirichlet boundary conditions. To model the 2-D viscous inclusion we use a 3-D model with a cylindrical model configuration and only one element in the third direction (along the cylindrical axis). The pressure and velocity errors were computed for each integration point using the analytical solution to verify the results of the 3-D cylindrical simulation. To calculate the velocity and pressure errors we use L2-norms:

$$e_p = \int_{\Omega} (p - p^{ana})^2 dV \quad (2.67)$$

$$e_v = \int_{\Omega} (v_x - v_x^{ana})^2 + (v_y - v_y^{ana})^2 dV \quad (2.68)$$

$$e_p^{tot} = \sqrt{\sum_{element} e_p} \quad (2.69)$$

$$e_v^{tot} = \sqrt{\sum_{element} e_v} \quad (2.70)$$

Where e_p and e_v are the pressure error and the velocity error integrated over the element using the analytical pressure and velocity, p^{ana} and v^{ana} , respectively given by Schmid (2003) and e_p^{tot} and e_v^{tot} are the total error integrated over the entire model domain. The results of the inclusion test are shown in figures 2.2-2.4.

Acknowledgements

The data presented in this paper are the result of forward numerical simulations (see Sec. 2 and 3 and appendix). This work was supported by SNF grant no. 200021_131897 and the University of Lausanne. Thibault Duretz, Yuri Podladchikov and Dave May provided practical help with programming and with setting up the benchmark models and simulations. Many discussions with them are greatly acknowledged. Further, we thank Dave May and an anonymous reviewer for their helpful comments.

References

Adamuszek M., Schmid D. W. and Dabrowski M., 2013: **Theoretical analysis of large amplitude folding of a single viscous layer**, *Journal of Structural Geology* 48, 137–152

- Altenbach H., 2012: **Kontinuumsmechanik**, Springer Vieweg
- Babeyko A., Sobolev S., Trumbull R., Oncken O. and Lavier L., 2002: **Numerical models of crustal scale convection and partial melting beneath the Altiplano-Puna plateau**, Earth Planetary Science Letters 199
- Bathe K.-J., 1990: **Finite-Elemente-Methoden: Matrizen und lineare Algebra, die Methode der finiten Elemente, Lösung von Gleichgewichtsbedingungen**, Springer Verlag, Berlin, Heidelberg, New York
- Bathe K.-J., 1996: **Finite Element Procedures**, Prentice hall, Inc., New Jersey
- Bauville A., Epard J.-L. and Schmalholz S., 2013: **A simple thermo-mechanical shear model applied to the Morcles fold nappe (Western Alps)**, tectono 583, 76–87
- Biot M. A., 1961: **Theory of Folding of Stratified Viscoelastic Media and Its Implications in Tectonics and Orogenesis**, Geol. Soc. Am. Bull. 72, 1595–1620
- Burg J. and Schmalholz S., 2008: **Viscous heating allows thrusting to overcome crustal-scale buckling: numerical investigation with application to the Himalayan syntaxes**, Earth Planetary Science Letters 274
- Burkett E. R. and Billen M. I., 2011: **Three-dimensionality of slab detachment due to ridge-trench collision: Laterally simultaneous boudinage versus tear propagation**, Geochemistry Geophysics Geosystems 11, 189–203
- Capitanio F. and Replumaz A., 2013: **Subduction and slab breakoff controls on Asian Indentation tectonics and Himalayan Western Syntaxis formation**, Geochemistry Geophysics Geosystems doi:10.1002/ggge.20171
- Conrad C. and Molnar P., 1997: **The growth of Rayleigh-Taylor-type instabilities in the lithosphere for various rheological and density structures**, Geophys. J. Int. 129, 95–112
- Dabrowski M., Krotkiewski M. and Schmid D. W., 2008: **MILAMIN: MATLAB-based finite element method solver for large problems**, Geochemistry Geophysics Geosystems 4
- Dietrich D. and Casey M., 1989: **A new tectonic model for the Helvetic nappes**, Alpine Tectonics, Geological Society Special Publication 54, 47–63

- Elman H., Silvester D. and Wathen A., 2005: **Finite Elements and Fast Iterative solvers: With Applications in Incompressible Fluid Dynamics**, Numerical Mathematics and Scientific Computation, OUP Oxford
- Epard J.-L., 1990: **La Nappe de Morcles au Sud-Ouest du Mont-Blanc**, Mem. Geol. Lausanne page 165 pp.
- Epard J.-L. and Escher A., 1996: **Transition from basement to cover: a geometric model**, Journal of Structural Geology 18, 333–548
- Escher A., Masson H. and Steck A., 1993: **Nappe geometry in the Western Swiss Alps**, Journal of Structural Geology 15, 501–509
- Fletcher R. C., 1974: **Wavelength selection in the folding of a single layer with power-law rheology**, American Journal of Science 274, 1029–1043
- Fletcher R. C., 1991: **Three-dimensional folding of an embedded viscous layer in pure shear**, Journal of Structural Geology 13, 87–96
- Fletcher R. C., 1995: **Three-dimensional folding and necking of power-law layers: are folds cylindrical, and, if so, do we understand why?**, Tectonophysics 247, 65–83
- Frehner M. and Schmalholz S. M., 2006: **Numerical simulations of parasitic folding in multilayers**, Journal of Structural Geology 28, 1647–1657
- Fullsack P., 1995: **An arbitrary Lagrangian-Eulerian formulation for creeping flows and its application in tectonic models**, Geophys. J. Int. 120, 1–23
- Gerya T., 2010: **Introduction to Numerical Geodynamic Modelling**, Cambridge University Press
- Gerya T. and Yuen D., 2003: **Characteristics-based marker-in-cell method with conservative finite-differences schemes for modeling geological flows with strongly variable transport properties**, Physics of the Earth and Planetary Interiors 140, 293–318
- Gerya T. and Yuen D., 2007: **Robust characteristics method for modelling multiphase visco-elasto-plastic thermo-mechanical problems**, Physics of the Earth and Planetary Interiors 163, 83–105

- Gosh S., 1970: **A theoretical study of intersecting fold patterns**, *Tectonophysics* 9, 559–569
- Grasemann B. and Schmalholz S. M., 2012: **Lateral fold growth and fold linkage**, *Geology* 40, 1039–1042
- Heuret A. and Lallemand S., 2005: **Plate motions and back-arc deformation**, *Physics of the Earth and Planetary Interiors* 149, 31–51
- Johnson A. and Fletcher R., 1994: **Folding of viscous layers: Mechanical analysis and Interpretation of Structures in Deformed Rock**, Columbia University Press
- Kaus B. and Podlatchikov Y., 2001: **Forward and Reverse Modeling of the Three-Dimensional Viscous Rayleigh-Taylor Instability**, *Geophysical Research Letters* 28, 11095–098
- Kaus B. and Schmalholz S., 2006: **3D finite amplitude folding: Implications for stress evolution during crustal and lithospheric deformation**, *Geophysical Research Letters* 33
- Kenis I., Urai J., van der Zee W. and Sintubin M., 2004: **Mullions in the High-Ardenne Slate Belt (Belgium): numerical model and parameter sensitivity analysis**, *Journal of Structural Geology* 26, 1677–1692
- Kidan T. and Cosgrove J., 1996: **The deformation of multilayers by layer-normal compression; An experimental investigation**, *Journal of Structural Geology* 18, 461–474
- Kronbichler M., Heister T. and Bangerth W., 2012: **High accuracy mantle convection simulation through modern numerical methods**, *Geophys. J. Int.* 191, 12–29
- Lechmann S., May D., Kaus B. and Schmalholz S., 2011: **Comparing thin-sheet models with 3-D multilayer models for continental collision**, *Geophys. J. Int.* 187, 10–33
- Mancktelow N. S., 1999: **Finite-element modelling of single layer folding in elasto-viscous materials: the effect of initial perturbation geometry**, *Journal of Structural Geology* 21, 161–177
- McAdoo D. and Sandwell D., 1985: **Folding of oceanic lithosphere**, *Journal of Geophysical Research* 90, 8563–8569

- Moresi L., Dufour F. and Mühlhaus H.-B., 2003: **A Lagrangian integration point finite element method for large deformation modeling of viscoelastic geomaterials**, *J. Comput. Phys.* 184, 476–497
- Moresi L., Quenette S., Lemiale V., Meriaux C., Appelbe B. and Mühlhaus H.-B., 2007: **Computational approaches to studying non-linear dynamics of the crust and mantle**, *Physics of the Earth and Planetary Interiors* 163, 69–82
- Mühlhaus H.-B., Sakaguchi H. and Hobbs B., 1998: **Evolution of three-dimensional folds for a non-Newtonian plate in a viscous medium**, *Proc. R. Soc. Lond. A* 454, 3121–3143
- Pfiffner O., 1993: **The structure of the Helvetic nappes and its relation to the mechanical stratigraphy**, *Journal of Structural Geology* 15, 511–521
- Pfiffner O., 2011: **Structural Map of the Helvetic Zone of the Swiss Alps, including Vorarlberg (Austria) and Haute Savoie (France), 1:100000**, Geological Special Map 128. Explanatory notes.
- Poliakov A. and Podladchikov Y., 1992: **Diapirism and topography**, *Geophys. J. Int.* 109, 553–564
- Pollard D. and Fletcher R., 2005: **Fundamentals of Structural Geology**, Cambridge University Press
- Popov A. and Sobolev S., 2008: **SLIM3D: A tool for three-dimensional thermomechanical modeling of lithospheric deformation with elasto-visco-plastic rheology**, *Physics of the Earth and Planetary Interiors* 171, 55–75
- Ramberg H., 1955: **Natural and experimental boudinage and pinch-and-swell structures**, *Journal of Geology* 63, 512–526
- Ramsay J. G., 1967: **Folding and fracturing of rocks**, McGraw-Hill, New York, N.Y.
- Ramsay J. G., 1981: **Tectonics of the Helvetic Nappes**, Geological Society, London, Special Publications 9, 293–309
- Ramsay J. G., Casey M. and Kligfield R., 1983: **Role of shear in development of the Helvetic fold-thrust belt of Switzerland**, *Geology* 11, 439–442

- Reber J., Schmalholz S. and Burg J.-B., 2010: **Stress orientation and fracturing during three-dimensional buckling: Numerical simulation and application to chocolate-tablet structures in folded turbidites, SW Portugal**, *Tectonophysics* 493, 187–195
- Ribe N., 1998: **Spouting and planform selection in the Rayleigh-Taylor instability of miscible viscous fluids**, *J. Fluid. Mech.* 377, 27–45
- Schmalholz S. M., 2006: **Scaled amplification equation: A key to the folding history of buckled viscous single-layers**, *Tectonophysics* 419, 41–53
- Schmalholz S. M., 2011: **A simple analytical solution for slab detachment**, *Earth Planetary Science Letters* 304, 45–54
- Schmalholz S. M. and Podladchikov Y. Y., 1999: **Buckling versus folding: Importance of viscoelasticity**, *Geophysical Research Letters* 26, 2641–2644
- Schmalholz S. M. and Podladchikov Y. Y., 2000: **Finite amplitude folding: transition from exponential to layer length controlled growth**, *Earth Planetary Science Letters* 181, 619–633
- Schmalholz S. M. and Podladchikov Y. Y., 2001: **Strain and competence contrast estimation from fold shape**, *Tectonophysics* 340, 195–213
- Schmalholz S. M., Podladchikov Y. Y. and Schmid D., 2001: **A spectral/finite difference method for simulating large deformations of heterogeneous, viscoelastic materials**, *Geophys. J. Int.* 145, 199–208
- Schmalholz S. M., Podladchikov Y. Y. and Burg J.-B., 2002: **Control of folding by gravity and matrix thickness: Implications for large-scale folding**, *Journal of Geophysical Research* 107
- Schmalholz S. M., Schmid D. and Fletcher R., 2008: **Evolution of pinch-and-swell structures in a power-law layer**, *Journal of Structural Geology* 30, 649–663
- Schmid D., 2003: **Analytical solutions for deformable elliptical inclusions in general shear**, *Geophys. J. Int.* 155, 269–288
- Schmid D., Dabrowski M. and Krotkiewski M., 2008: **Evolution of large amplitude 3D fold patterns: A FEM study**, *Physics of the Earth and Planetary Interiors* 171, 400–108

- Smith R. B., 1977: **Formation of folds, boudinage, and mullions in non-Newtonian materials**, Geological Society of America Bulletin 88, 312–320
- Steck A., Bigioggero B., Piaz G. D., Escher A., Martinotti G. and Masson H., 1999: **Carte tectonique des Alpes de Suisse occidentale et des regions avoisinantes, 1:100000**, Carte geologique speciale n 123, Swiss National Hydrological and Geological Survey
- Tackley P., Stevenson D., Glatzmaier G. and Schubert G., 1993: **Effects of an endothermic phase transition at 670 km depth in a spherical model of convection in the Earth's mantle**, Nature 361
- Tamaki K. and Honza E., 1991: **Global tectonics and formation of marginal basins: Rose of western Pacific**, Episodes 14
- Thielmann M., May D. and Kaus B., 2014: **Discretization Errors in the Hybrid Finite Element Particle-in-cell Method**, Pure and Applied Geophysics pages 1–20, doi:{10.1007/s00024-014-0808-9}
- Thieulot C., 2011: **FANTOM: Two- and three-dimensional numerical modelling of creeping flows for the solution of geological problems**, Physics of the Earth and Planetary Interiors 188, 47–68
- Thieulot C., Glerum A., Hillebrand B., Schmalholz S., Spackman W. and Torsvik T., 2014: **A two- and three-dimensional numerical modelling benchmark of slab detachment**, Geophysical Research Abstracts, EGU2014-8395, EGU General Assembly 2014 16
- Turcotte D. and Schubert G., 2002: **Geodynamics**, Cambridge University Press, Cambridge
- van Hunen J. and Allen M. B., 2011: **Continental collision and slab break-off: A comparison of 3-D numerical models with observations**, Earth Planetary Science Letters 302, 27–37
- van Keken P., S.D K., Schmeling H., Christensen U., Neumeister D. and Doin M.-P., 1997: **A comparison of methods for the modeling of thermomechanical convection**, Journal of Geophysical Research 102, 22477–22495
- von Tscharner M., Schmalholz S. and Duretz T., 2014: **Three-dimensional necking during viscous slab detachment**, Geophysical Research Letters 41, 4194–4200

Weinberg R. and Schmeling H., 1992: **Polydiapirs: Multiwavelength gravity structures**, Journal of Structural Geology 14, 425–436

Zienkewicz O. C. and Taylor R., 2000: **The Finite Element Method**, Butterworth-Heinemann

3 Three-dimensional necking during viscous slab detachment

Abstract

Key points: slab detachment, slab breakoff, 3-D mechanical modelling, subduction processes

We study the three-dimensional (3-D) deformation during detachment of a lithospheric slab with simple numerical models using the finite element method. An initially vertical layer of power-law viscous fluid mimics the slab, and is surrounded by a linear or power-law viscous fluid representing asthenospheric mantle. We quantify the impact of slab size and shape (symmetric/asymmetric) on slab detachment, and identify two processes that control the lateral (i.e. along trench) slab deformation: (1) the horizontal deflection of the lateral, vertical slab sides (> 100 km with velocities up to 16 mm/yr), and (2) the propagation of localized thinning (necking) inside the slab (with velocities > 9 cm/yr). The lateral propagation velocity is approximately constant during slab detachment. Larger slabs (here wider than approximately 300 km) detach with rates similar to those predicted by 2-D models whereas smaller slabs detach slower. Implications for geodynamic processes and interpretations of seismic tomography are discussed.

Index terms: 8170, 8120, 8122, 8162, 4445

This chapter was published in
Geophysical Research Letters 41 (2014)
co-authored by von Tscharnier M., Duretz T. and Schmalholz S. M.

3.1. Introduction

Slab detachment (or breakoff) implies that the negative buoyancy of subducting slabs can be sufficiently large to trigger the detachment of slab portions. Detachment hence regulates the magnitude of the slab pull force and the occurrence of such event has consequences on both lithospheric and asthenospheric dynamics. For this reason, slab detachment has been proposed to explain a variety of geological phenomena relative to convergent margins such as exhumation of metamorphic rocks (Andersen *et al.*, 1991; Kohn and Parkinson, 2002), topographic uplift (Rogers *et al.*, 2002; Morley and Back, 2008), variations in plate kinematics (Austermann *et al.*, 2011), or plutonism/volcanism (Davies and von Blanckenburg, 1995; Ferrari, 2004). The slab detachment model entails the existence of mechanical discontinuities in subducted plates, which was first hypothesized to explain discontinuous seismicity patterns observed within slabs (Isacks and Molnar, 1969; Chatelain *et al.*, 1993). Seismic tomography of the mantle allowed for the detection of potentially detached slab fragments (Wortel and Spakman, 1992; Widiyantoro and van der Hilst, 1996; van der Meer *et al.*, 2010; Lippitsch *et al.*, 2003; Replumaz *et al.*, 2010), and further suggested that slabs can exhibit complex deformation patterns (Sperner *et al.*, 2001; Rosenbaum *et al.*, 2008; Nolet, 2009; Faccenna *et al.*, 2011). The interpretation of tomographic images and application of the slab detachment model to observed geological phenomena requires a thorough understanding and quantification of three-dimensional (3-D) deformation during slab detachment. However, 3-D slab detachment has until now be the focus of few numerical modeling studies (Burkett and Billen, 2011; van Hunen and Allen, 2011; Capitanio and Replumaz, 2013; Li *et al.*, 2013; Duretz *et al.*, 2014), which investigated complex rheologies and initial plate configurations. In contrast, we study here an idealized slab detachment configuration that focuses on the necking instability of lithospheric plates subjected to gravity. This study builds upon the 1-D and 2-D studies of Schmalholz (2011) and Duretz *et al.* (2012). Our aim is to better understand the deformation patterns that arise during purely mechanical 3-D necking, and to quantify the 3-D necking during slab detachment.

3.2. Numerical Model

The 3-D viscous flow is described by the conservation of momentum and mass for an incompressible, highly viscous fluid driven by gravity (often referred to as Stokes equations). The

flow law is either linear or power-law viscous where for the latter the effective viscosity is controlled by the second invariant of the strain rate tensor and the power-law stress exponent, n (see Schmalholz and Schmid (2012) for a 2-D version of the applied equations). The system of governing equations is solved numerically with the finite element method (FEM). In the applied finite element algorithm a mixed velocity-pressure formulation utilising a structured hexahedral mesh employing tri-quadratic shape functions for velocity (Q2) and piece-wise discontinuous linear shape functions for pressure (P1) (Bathe, 1996) is used.

In the continuity equation we introduce a penalty term and solve the penalised system by applying a Richardson iteration to the reduced velocity Schur complement system (Dabrowski *et al.*, 2008). Non-linearities inherent to the power-law rheology are treated with Picard iterations.

The Stokes problem is solved on a structured hexahedral finite element mesh. The mesh is Lagrangian and thus the nodal coordinates are advected at each time step using the fluid velocity (explicit Euler step). We use a deformable Lagrangian mesh because the necking instability is strongly sensitive to small geometrical variations of the material interface (here the slab/mantle interface) during the initial stages of necking (e.g. Schmalholz *et al.* (2008)), and the deformable mesh (that initially conforms to the slab/mantle interface) can accurately follow and resolve these small geometrical variations. Throughout the deformation of the slab, elements get distorted and thus the mesh quality degenerates. At each re-meshing step, a new structured finite element mesh is generated. Within our 3-D numerical model, we represent all material-interfaces (e.g. between the mantle and the slab) with a set of marker points. The marker points are Lagrangian, and during the deformation their coordinates are calculated with the velocity shape functions that are used for the coordinate transformation in the isoparametric finite elements. Once re-meshing has occurred the material interface will intersect the element interiors. We use the material-interface to define the material phase (material properties) on each quadrature point. For a vertical line located at the horizontal coordinates of the quadrature point we determine all intersections with the material-interface. Using the vertical coordinates of these intersection points we are able to determine whether the quadrature point is located inside or outside the volume which is defined by the material-interface. The first re-meshing in the simulations is performed as late as possible so that during the initial stages of the necking instability the Lagrangian mesh can accurately resolve the slab/mantle interface. After the first re-meshing the following re-meshings are performed in regular intervals.

The model domain is a rectangular box and consists of a vertically-oriented rectangular layer of power-law viscous fluid (the slab) which is attached to a 80 km thick horizontal layer with identical material parameters (non-subducted lithosphere, Fig. 3.1). The rest of the model is filled by a linear viscous or power-law viscous fluid representing surrounding asthenospheric mantle that deforms by diffusion or dislocation creep, respectively. For the majority of the simulations the boundary conditions are free slip on all sides. We only performed one simulation with a free surface at the top boundary in order to investigate the impact of a free surface on the results. The model domain is always 670 km high and 250 km wide (in direction orthogonal to the trench, x-direction, Fig. 3.1).

The slabs are initially always 40 km thick assuming that only one symmetric half of the 3-D simulation is modeled whereby the symmetry-plane is vertical and parallel to the longest slab dimension (y-direction or along-trench direction, Fig.3.1), and cuts the slab in two identical parts (i.e. true slab thickness is 80 km). Simulations with an initial slab width (along-trench direction, y-direction, Fig. 3.1) of 80, 320 and 800 km have been performed with an initial slab length (height) of 187.5 km (labelled sym. 80, sym. 320 and sym. 800 in Fig. 3.3). For these simulations the mantle adjacent to the lateral slab sides was $W_M = 100$ km on each side (Fig. 3.1). Therefore, the total width of the model box W_{tot} is varying. A simulation with an initial slab width of 320 km has been also performed with a mantle width of $W_M = 300$ km to quantify the impact of varying mantle width on the results (labelled sym. 320 large in Fig. 3.3). Also, a simulation with an asymmetric slab of 800 km width and a mantle width adjacent to the lateral slab sides of $W_M = 100$ km on each side has been performed (Fig. 3.1b).

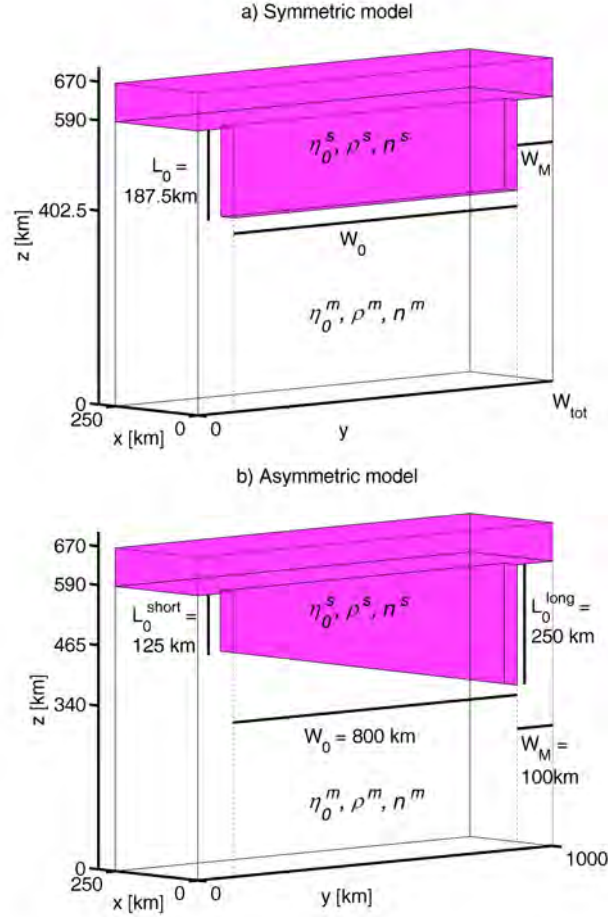


Figure 3.1: Symmetric (a) and asymmetric (b) model configuration. In the symmetric case we use an initial vertical slab length of $L_0 = 187.5$ km whereas the initial slab length for the asymmetric simulation varies such that the total slab volume is identical to the symmetric slab with an initial slab width of $W_0 = 800$ km. The vertical layer has a thickness of 80 km whereas the layer is vertically halved to 40 km due to symmetry considerations. For all simulations we use a density difference of $\Delta\rho = 150 \text{ kg.m}^{-3}$ ($\rho^s = 3150 \text{ kg.m}^{-3}$ and $\rho^m = 3000 \text{ kg.m}^{-3}$), a reference viscosity of $\eta_0^s = 2.37 \times 10^{11} \text{ Pa.s}^{1/n}$ and a power-law stress exponent of $n^s = 4$ for the slab and a reference viscosity of $\eta_0^m = 10^{21} \text{ Pa.s}$ and a power-law stress exponent of $n^m = 1$ (i.e. linear viscous flow) or a reference viscosity of $\eta_0^m = 4.65 \times 10^{10} \text{ Pa.s}^{1/n}$ and a power-law stress exponent of $n^m = 3$ for the mantle.

The initial, different slab lengths have been chosen in such a way that the slab volume and buoyancy of the symmetric slab with 800 km is identical to the one of the asymmetric slab. For the simulation with a slab width of 80 km we use an adaptive mesh, which has a resolution (i.e. nodal spacing) of about 3 km within the slab (x- and z-direction) and a resolution of 10 km elsewhere (x-, y- and z-direction). For all other simulations we use a resolution of 4.5 km within the slab and a resolution of 17 km elsewhere. The geometry and the material properties are given in figure 3.1 and its caption. For all simulations we use a density difference of $\Delta\rho = 150 \text{ kg.m}^{-3}$, reference viscosity of $\eta_0^s = 2.37 \times 10^{11} \text{ Pa.s}^{1/n}$ and a power-law stress exponent of $n^s = 4$ for the slab. A reference viscosity of $\eta_0^m = 10^{21} \text{ Pa.s}$ and a power-law stress exponent of $n^m = 1$ (i.e. linear viscous flow) is used for the mantle. Additionally, two simulations with a power-law viscous mantle were performed using a reference viscosity of $\eta_0^m = 4.65 \times 10^{10} \text{ Pa.s}^{1/n}$ and a power-law stress exponent of $n^m = 3$, where one of the simulations was performed with a free surface (labelled sym. 320, $n^m = 3$, sym 320 and $n^m = 3$, free in Fig. 3.3). The viscosity formulation is described in more details in Schmalholz (2011), and the resulting effective viscosities have typical values corresponding to olivine rheology in both the lithospheric slab and the surrounding mantle. In order to quantify the impact of a 3-D configuration on the deformation, we also ran corresponding 2-D numerical simulations using the same set of model parameters (i.e. model configuration, initial slab thickness and height, viscosity and density difference).

3.3. Results

Figure 3.2 shows the 3-D geometric evolution of an initially symmetric and asymmetric slab of 800 km width. The colors on the slab surface indicate the effective viscosity. The thinning is localized at the top of the slab due to the occurrence of a necking instability (Schmalholz, 2011). During the initial stages of slab detachment (Fig. 3.2e and f) thinning of the symmetric slab is more intense in the slab center than at the lateral sides of the slab. The results also show that there is a significant amount of lateral (horizontal, in y-direction) deflection of the two lateral sides of the slab at the depth of most intense thinning. The asymmetric slab thinning is, as expected, most intense at the side where the slab is initially longest, because there the negative buoyancy is largest (Fig. 3.2a - d). The region of localized thinning (necking) is propagating laterally inside the slab during slab detachment. Significant lateral deflection of the slab sides also takes place for the asymmetric slab.

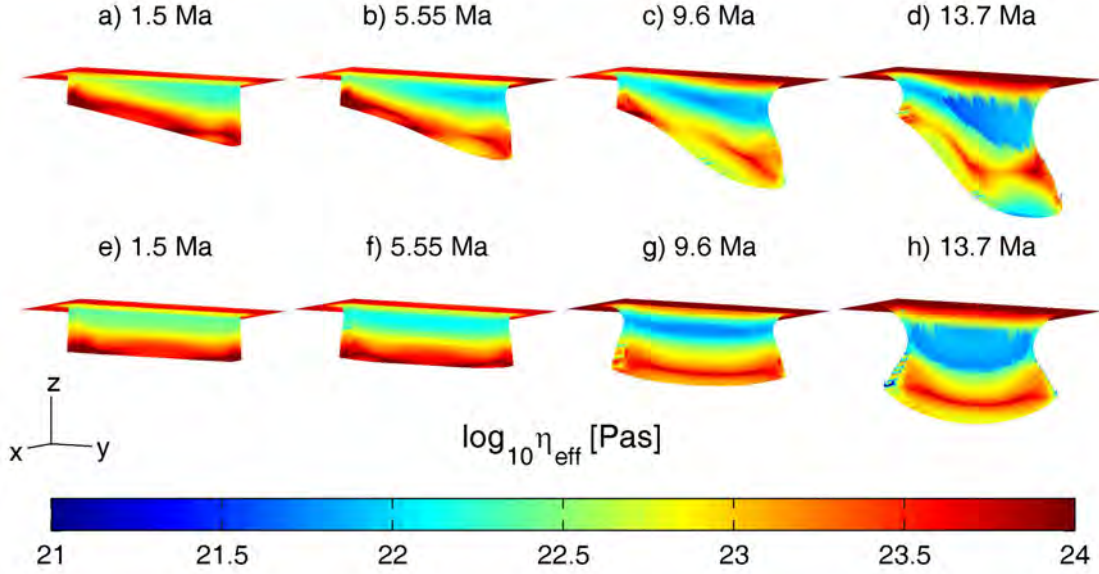


Figure 3.2: The 3-D geometric evolution of an initially symmetric (a-d) and asymmetric (e-h) slab of 800 km width for different times. The colors on the slab surface indicate the effective viscosity in Pa.s.

Figure 3.3 shows results of all the performed simulations. The evolution of the slab thickness (D) at the position of most intense thinning, the evolution of the minimal slab width (W , in y -direction), and the evolution of the horizontal cross-sectional area (A) at the depth of most intense thinning during slab detachment are displayed. For the symmetric simulations the minimum slab thickness D is measured in the middle of the slab at $y = W_{tot}/2$. For the asymmetric simulation we measure the minimum slab thickness for three different sections perpendicular to the y -axis, i.e. for $y = W_{tot}/2$ (asym. 800 mid) and at the short and long end of the slab (labelled asym. 800 short and asym. 800 long, respectively).

The change of A quantifies the downward out-of-plane flow of slab material during slab detachment, and also the upward flow of mantle material around the slab because the mantle material must replace the slab material to conserve mass during the incompressible flow. In figure 3.3a-c the quantities D , W and A are normalized by their respective initial quantities (with subscript 0), and are plotted versus the ratio slab length to initial slab length (L/L_0). The ratio L/L_0 indicates the vertical bulk slab extension. The evolution of D/D_0 with increasing L/L_0 is similar for all 3-D and the 2-D simulations independent of the initial slab size, slab shape, model size or the material parameters used for the mantle (i.e. linear or power-law viscous mantle, Fig. 3.3a). In

contrast, the evolution of W/W_0 with increasing L/L_0 mainly depends on the initial slab size, whereby the decrease of W/W_0 is largest for the smallest slab. Similar results are obtained for the evolution of A/A_0 where A/A_0 decreases strongest for the smallest slab. In figure 3.3d-f the dimensional quantities are plotted versus the absolute time. The evolution of D with time is more variable for the 3-D simulations. The thinning is significantly slower at the short side of the asymmetric slab, because the vertical buoyancy force is smallest at this side due to the smaller initial slab length. Also, the smallest slab (80 km) thins slower than the larger slabs due to its smaller buoyancy. However, slabs with 320 and 800 km width thin with the same rate that is equal to the thinning rate of the corresponding 2-D simulation. The thinning is significantly faster (i.e. 2-3 times) for the simulations with a power-law viscous mantle in agreement with results of Schmalholz (2011). The 3-D simulations with a power-law mantle with and without free surface thin with approximately the same rate. Also, these 3-D simulations are faster than the corresponding 2-D simulation.

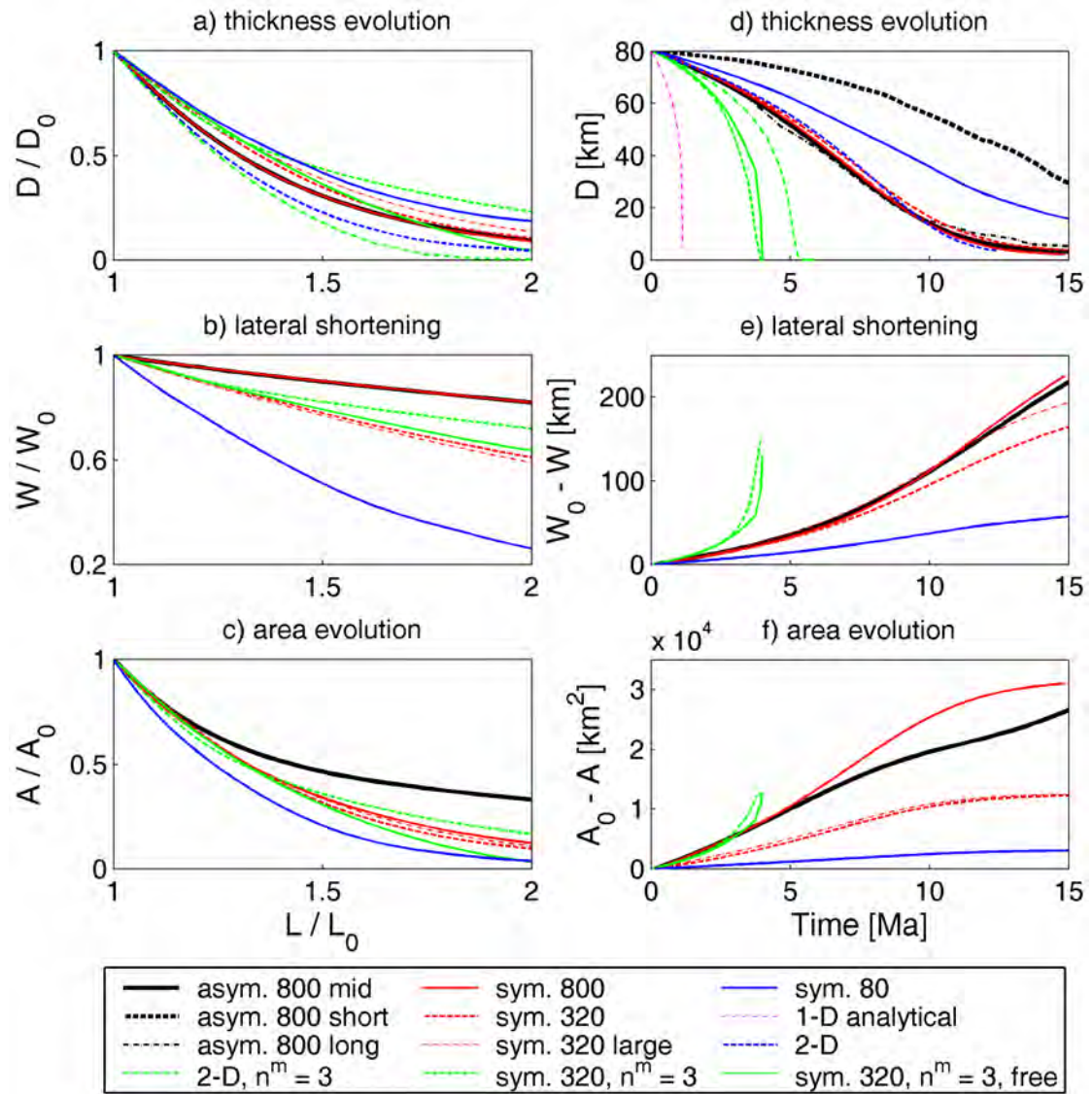


Figure 3.3: a-c) The evolution of the slab thickness D/D_0 , the slab width W/W_0 and the horizontal cross-sectional area A/A_0 (all at the depth of maximal thinning) are plotted versus the ratio of slab length to initial slab length L/L_0 . d-f) Dimensional quantities of slab thickness D [km], slab width $W_0 - W$ [km] and cross-sectional area $A_0 - A$ [km²] versus the absolute time [Ma].

The evolution of the absolute horizontal shortening of the slab ($W_0 - W$) with time is similar for the larger slabs (800 and 320 km), slowest for the smallest slab and fastest for the simulations with a power-law viscous mantle. For the symmetric slab of initially 320 km width the values

of $W_0 - W$ increase slightly faster for the simulation with a larger mantle width adjacent to the lateral slab sides, because the wider model causes a smaller shear resistance for the mantle. The values of $A_0 - A$ quantifying the vertical out-of-plane mass flow increase fastest with time for larger slabs. The evolution of $A_0 - A$ with time is similar for the symmetric and asymmetric slab. For the slabs of initially 320 km width the values of $A_0 - A$ increase similar independent on the width of the mantle adjacent to the lateral slab sides.

Figure 3.4 shows the evolution of the minimum slab thickness along the slab with progressive time for four selected simulations. The results for the initially symmetric slabs show that thinning is slightly faster in the central part of the slab, and homogeneous in most parts of the slab. Thinning is slightly slower at both lateral sides of the slabs. The velocity of the lateral deflection (or the horizontal shortening in the along-trench direction) increases with increasing slab size, and is in the order of $\sim 1 - 10$ mm/yr. For the asymmetric slab the obliqueness of the contours of thinning indicate the lateral propagation of thinning (necking), that is for the applied parameters approximately 9 cm/yr. The shape of the thickness contours indicate that the velocity of necking propagation is approximately constant during slab detachment, that is, no significant acceleration or deceleration of propagation occurs. The velocity of lateral slab deflection at the longer slab side is approximately 7 mm/yr, that is approximately one order of magnitude slower than the lateral thinning propagation.

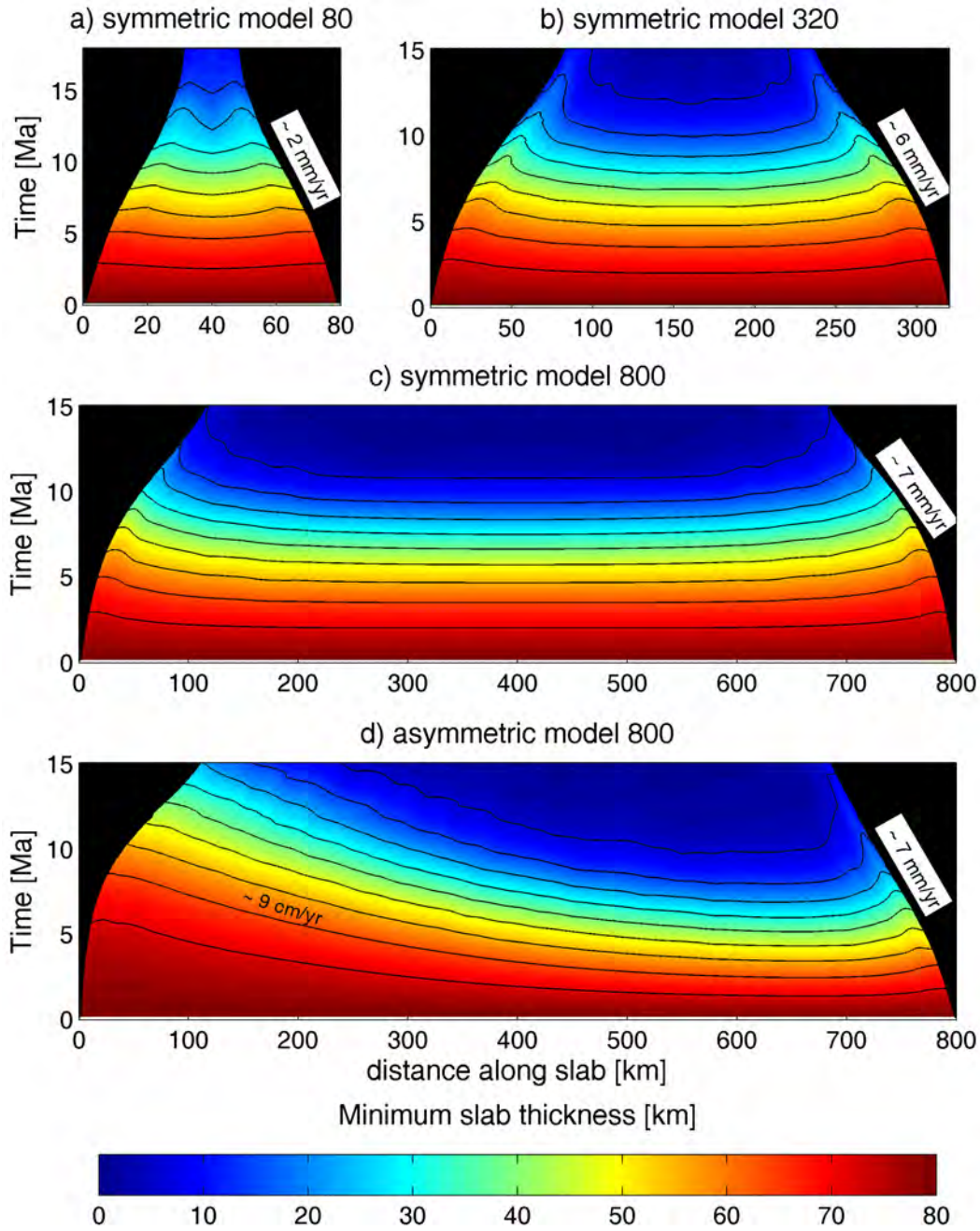


Figure 3.4: Contour maps showing minimal slab thickness (D) along the slab with time for selected 3-D simulations with a symmetric slab of 80 km width (a), 320 km width (b) and 800 km width (c), and an asymmetric slab of 800 km width (d). The black areas represent the gap of the slab due to the lateral (along trench) deflection (lateral shortening) during slab detachment. Velocities in mm/yr and cm/yr indicate velocities of lateral slab deflection and lateral propagation of thinning, respectively (see text).

3.4. Discussion

In our simulations a real detachment, that is a loss of continuity between the sinking slab and the floating lithosphere, does not occur, because our model does not include processes that cause discontinuities, such as fracturing. In our model the slab is effectively detached when the slab thickness is significantly reduced (Fig. 3.3d), because most of the sinking slab is then effectively mechanically decoupled from the lithosphere at the surface.

The evolution of necking (quantified by D/D_0) with progressive vertical bulk slab extension (quantified by L/L_0) is only weakly dependent on the slab size, the slab shape (symmetric or asymmetric), the width of the mantle adjacent to the lateral slab boundaries and the rheology of the mantle (i.e. linear or power-law viscous, Fig. 3.3a). This independence allows predicting the evolution of D/D_0 with increasing L/L_0 for many other slab configurations without performing additional 3-D simulations (for the same material parameters). In contrast, the evolution of thinning (D) with time is significantly different for slabs of different size, shape and mantle rheology.

In our simulations the 3-D finite slabs that are wider than ~ 300 km exhibit similar thinning rates as the corresponding 2-D slabs for both a linear viscous and a power-law viscous mantle. Hence, the 1-D analytical solution for slab necking (Schmalholz, 2011) can be applied at first-order accuracy to both 2-D and 3-D slab necking (Fig. 3.3a, d).

The zone of localized thinning in the asymmetric slab propagates laterally with a constant velocity. The lateral velocities of thinning of approximately 9 cm/yr for a linear viscous mantle and of approximately ~ 30 cm/yr for a power-law viscous mantle are similar to rates reported by van Hunen and Allen (2011) and Burkett and Billen (2011) who reported rates between 10 and 80 cm/yr. Such velocity is also consistent with the natural rates inferred from the Trans-Mexican volcanic belt (10-25 cm/yr), which may reflect lateral propagation of slab detachment (Ferrari, 2004).

Complex tomographic patterns around slab edges have been imaged by seismic tomography (Lallemand *et al.*, 2001; Lin *et al.*, 2004). In particular, slab gaps at slab edges have been evidenced by several studies in the Kamchatka region (Levin *et al.*, 2002, 2004; Jiang *et al.*, 2009). Our results show that such slab gaps can be the result of two processes: First, due to

a true detachment of the slab, and second, due to the lateral deflection of the slab during the process of slab detachment. Therefore, not every gap in a vertical section of tomographic results around a slab edge must necessarily indicate a fully detached slab, but could also be due to a laterally deflected slab that is still attached. Lateral deflection of a slab side can be larger than 100 km (Fig. 3.4c and d) and also affects narrow slabs. This further suggests that small slabs can also produce "drop-like" shapes of fast seismic velocity anomalies such as observed in the Hindukush (Koulakov and Sobolev, 2006) or the Vrancea regions (Koulakov *et al.*, 2010).

Natural slab detachment is a complex process controlled by thermal, mechanical and chemical processes and their coupling (e.g shear heating in Gerya *et al.* (2004)). Our viscous 3-D models are significantly simplified in order (1) to identify and quantify fundamental 3-D deformation processes during slab detachment, (2) to keep the model and the involved parameters comprehensible, and (3) to keep the computational costs low. More elaborated 3-D models are required in the future to model 3-D slab detachment in more detail.

3.5. Conclusions

3-D numerical simulations were performed to quantify the 3-D deformation during the buoyancy-driven necking of a laterally finite slab of power-law viscous fluid surrounded by a linear or power-law viscous mantle. The evolution of localized slab thinning (necking) with increasing vertical bulk extension of the slab is only weakly dependent on the slab size, the slab shape (symmetric or asymmetric), and the width of the mantle adjacent to the lateral slab side.

2-D simulations with the same model configuration and material parameters as the 3-D simulations indicate that 3-D slab detachment exhibits similar thinning rates as 2-D slab detachment for 3-D slabs with widths $> \sim 300$ km. Therefore, 2-D simulations can accurately predict thinning rates of such finite 3-D slabs.

During necking of the slab the vertical sides of the slab around the depth of necking deflect significantly in the lateral (along-trench) direction. Absolute values of lateral deflection increase with increasing slab size. This lateral deflection can be > 100 km, and could explain gaps in seismic tomography cross sections despite the fact that the slab is still attached.

For the applied parameters the velocities of lateral slab deflection are 2-7 mm/yr for a linear viscous mantle (wider slabs are deflecting faster) and 16 mm/yr for a power-law viscous mantle. These deflection velocities are approximately one order of magnitude smaller than the velocity of lateral propagation of slab necking which is ~ 9 cm/yr for a linear viscous mantle and ~ 30 cm/yr for a power-law viscous mantle. The velocity of lateral necking propagation is approximately constant during the slab detachment.

Acknowledgements

The data presented in this paper are the result of forward numerical simulations (see Sec. 2). The authors thank D.A. May and an anonymous reviewer for their helpful comments. This work was supported by SNF grant no. 200021_131897 and the University of Lausanne.

References

- Andersen T. B., Jamtveit B., Dewey J. F. and Swensson E., 1991: **Subduction and exhumation of continental crust: major mechanisms during continent-continent collision and orogenic extensional collapse, a model based on the south Norwegian Caledonides**, *Terra Nova* 3, 303–310
- Austermann J., Ben-Avraham Z., Bird P., Heidbach O., Schubert G. and Stock J. M., 2011: **Quantifying the forces needed for the rapid change of Pacific plate motion at 6 Ma**, *Earth Planetary Science Letters* 307, 289–297
- Bathe K.-J., 1996: **Finite Element Procedures**, Prentice hall, Inc., New Jersey
- Burkett E. R. and Billen M. I., 2011: **Three-dimensionality of slab detachment due to ridge-trench collision: Laterally simultaneous boudinage versus tear propagation**, *Geochemistry Geophysics Geosystems* 11, 189–203
- Capitanio F. and Replumaz A., 2013: **Subduction and slab breakoff controls on Asian Indentation tectonics and Himalayan Western Syntaxis formation**, *Geochemistry Geophysics Geosystems* doi:10.1002/ggge.20171

- Chatelain J.-L., Guillier B. and Gratier J.-P., 1993: **Unfolding the subducting plate in the central New Hebrides island arcs: geometrical argument for detachment of part of the downgoing slab**, *Geophysical Research Letters* 20, 655–658
- Dabrowski M., Krotkiewski M. and Schmid D. W., 2008: **MILAMIN: MATLAB-based finite element method solver for large problems**, *Geochemistry Geophysics Geosystems* 4
- Davies H. J. and von Blanckenburg F., 1995: **Slab breakoff: A model of lithosphere detachment and its test in the magmatism and deformation of collisional orogens**, *Earth and Planetary Science Letters* 129, 85–102
- Duretz T., Schmalholz S. M. and Gerya T. V., 2012: **Dynamics of slab detachment**, *Geochemistry Geophysics Geosystems* 13, 17PP, doi:10.1029/2011GC004024
- Duretz T., Gerya T. V. and Spakman W., 2014: **Slab detachment in laterally varying subduction zones: 3-D numerical modeling**, *Geophysical Research Letters*
- Faccenna C., Molin P., Orecchio B., Olivetti V., Bellier O., Funicello F., Minelli L., Piromallo C. and Billi A., 2011: **Topography of the Calabria subduction zone (southern Italy): Clues for the origin of Mt. Etna**, *Tectonics* 30, TC1003
- Ferrari L., 2004: **Slab detachment control on mafic volcanic pulse and mantle heterogeneity in central Mexico**, *Geology* 32, 77–80
- Gerya T. V., Yuen D. A. and Maresch W., 2004: **Thermomechanical modelling of slab detachment**, *Earth and Planetary Science Letters* 226, 101–116
- Isacks B. and Molnar P., 1969: **Mantle Earthquake Mechanisms and the Sinking of the Lithosphere**, *Nature* 223, 1121–1124
- Jiang G., Zhao D. and Zhang G., 2009: **Seismic tomography of the Pacific slab edge under Kamchatka**, *Tectonophysics* 465, 190–203
- Kohn M. J. and Parkinson C. D., 2002: **Petrologic case for Eocene slab breakoff during the Indo-Asian collision**, *Geology* 30, 591–594
- Koulakov I. and Sobolev S., 2006: **A tomographic image of Indian lithosphere break-off beneath the Pamir-Hindukush region**, *Geophys. J. Int.* 164, 425–440

- Koulakov I., Zaharia B., Enescu B., Radulain M., Popa M., Parolai S. and Zschau J., 2010: **Delamination or slab detachment beneath Vrancea? New arguments from local earthquake tomography**, *Geochemistry Geophysics Geosystems* 11, Q03002
- Lallemand S., Font Y., Bijwaard H. and Kao H., 2001: **New insights on 3-D plates interaction near Taiwan from tomography and tectonic implications**, *Tectonophysics* 333, 229–253
- Levin V., Shapiro N., Park J. and Ritzwoller M., 2002: **Seismic evidence for catastrophic slab loss beneath Kamchatka**, *Nature* 418, 763–767
- Levin V., Shapiro N., Park J. and Ritzwoller M., 2004: **Slab portal beneath the western Aleutians**, *Geology* 33, 253–256
- Li Z., Xu Z., Gerya T. V. and Burg J.-P., 2013: **Collision of continental corner from 3-D numerical modeling**, *Earth Planetary Science Letters* pages 98–11
- Lin J.-Y., Hsu S.-K. and Sibuet J.-C., 2004: **Melting features along the western Ryukyu slab edge (northeast Taiwan): Tomographic evidence**, *Journal of Geophysical Research* 109, B12402
- Lippitsch R., Kissling E. and Ansorge J., 2003: **Upper mantle structure beneath the Alpine orogen from high-resolution teleseismic tomography**, *Journal of Geophysical Research* 108
- Morley C. K. and Back S., 2008: **Estimating hinterland uplift exhumation from late orogenic basin volume, NW Borneo**, *Journal of the Geological Society* 165, 353–366
- Nolet G., 2009: **Slabs do not go gently**, *Science* 324, 152–153
- Replumaz A., Negredo A. M., Guillot S. and Villasenor A., 2010: **Multiple episodes of continental subduction during India/Asia convergence: Insight from seismic tomography and tectonic reconstruction**, *Tectonophysics* 483, 125–134
- Rogers R. D., Karason H. and van der Hilst R. D., 2002: **Epeirogenic uplift above a detached slab in northern Central America**, *Geology* 30, 1031–1034
- Rosenbaum G., Gasparon M., Lucente F. P., Peccerillo A. and Miller M. S., 2008: **Kinematics of slab tear faults during subduction segmentation and implications for Italian magmatism**, *Tectonics* 27, TC2008

- Schmalholz S. M., 2011: **A simple analytical solution for slab detachment**, *Earth Planetary Science Letters* 304, 45–54
- Schmalholz S. M. and Schmid D. W., 2012: **Folding in power-law viscous multilayers**, *Philosophical Transactions of the Royal Society A* 370, 1798–1826
- Schmalholz S. M., Schmid D. and Fletcher R., 2008: **Evolution of pinch-and-swell structures in a power-law layer**, *Journal of Structural Geology* 30, 649–663
- Sperner B., Lorenz F., Bonjer K., Hettel S., Müller B. and Wenzel F., 2001: **Slab break-off - abrupt cut or gradual detachment? New insights from the Vrancea Region (SE Carpathians, Romania)**, *Terra Nova* 13, 172–139
- van der Meer D., Spakman W., van Hinsbergen D., Amaru M. L. and Torsvik T. H., 2010: **Towards absolute plate motions constrained by lower-mantle slab remnants**, *Nature Geoscience* 3, 36–40
- van Hunen J. and Allen M. B., 2011: **Continental collision and slab break-off: A comparison of 3-D numerical models with observations**, *Earth Planetary Science Letters* 302, 27–37
- Widiyantoro S. and van der Hilst R., 1996: **Structure and evolution of lithospheric slab beneath the Sunda Arc, Indonesia**, *Science* 271, 1566–1570
- Wortel M. J. R. and Spakman W., 1992: **Structure and dynamics of subducted lithosphere in the Mediterranean region**, *Proceedings of the Koninklijke Nederlandse Akademie van Wetenschappen-Biological Chemical Geological Physical and Medical Sciences* 95, 325–347

4 3-D hydrodynamic modelling applied to fold nappes and the Rawil depression in the Helvetic nappe system (western Switzerland)

Abstract

The Helvetic nappe system in western Switzerland exhibits distinct three-dimensional (3-D) structural features such as the lateral variation in geometry and deformation style between the Morcles and Doldenhorn fold nappes or the Rawil depression that separates the two nappes. We perform 3-D finite element simulations of viscous flow to investigate the formation of fold nappes during shortening of a half graben with laterally varying thickness. The results show that the thickness of the half graben has a significant impact on the fold nappe evolution. Fold nappes that are generated above a thicker half graben have (i) larger amplitudes, (ii) a less sheared and less thinned overturned limb, and (iii) a larger nappe thickness than fold nappes that are generated above a thinner half graben. These fundamental differences are observed between the Morcles and Doldenhorn nappes, and suggest that the structural differences between the nappes resulted from different thickness of the corresponding pre-Alpine half graben. The simulations further show that during the shortening the half graben is closed and forms a mullion-like structure which also agrees with field observations. We also perform 3-D simulations to study the impact of an oblique half graben on the basement uplift during shortening accompanied by orthogonal extension. The results show that the half graben can cause a laterally varying basement uplift which generates a depression whose amplitude depends on the initial graben orientation and the power-law stress exponent of basement and sediments. The maximal axial plunge of the modelled depression is smaller than the observed plunge of the Rawil depression which indicates that additional processes are required to explain the observed geometry of the Rawil depression.

This chapter will be submitted to
Tectonophysics
co-authored by von Tscharnern M., Schmalholz S. M. and Eppard J.-L.

4.1. Introduction

4.2. Introduction

The Helvetic nappe system in western Switzerland (W-Switzerland) exhibits distinct three-dimensional (3-D) structural features such as the variation of the deformation style parallel to the fold axis between the Morcles and the Doldenhorn nappe or the Rawil depression which separates geographically the two nappes (Fig. 4.1). Several studies have argued that the Morcles and Doldenhorn nappes have been generated during the Alpine inversion of half grabens in the European passive continental margin (Pfiffner, 1993; Escher *et al.*, 1993). Also, several 2-D models have been presented that explain the overall formation of the Morcles fold nappe by ductile heterogeneous simple shear (Ramsay *et al.*, 1983; Casey and Dietrich, 1997; Bauville *et al.*, 2013). The geometry and deformation style of the Morcles and Doldenhorn nappe are different (see next section), and this lateral variation in geometry and deformation style has been explained with a different thickness of mechanically weak sediments in the two nappes (Pfiffner, 1993, 2011). However, there is no 3-D mechanical model that quantified the 3-D deformation due to such lateral thickness variation.

For the Rawil depression the geometry and structures are well documented and described in high detail (Argand, 1902-1911; Heim, 1921; Ramsay, 1981, 1989; Gasser and Mancktelow, 2010; Cardello and Mancktelow, 2014; Cardello, 2013). The Rawil depression has been explained with different tectonic scenarios such as oblique thrusting, tangential longitudinal strain or late folding during orogen-parallel shortening (Burkhard, 1988; Dietrich, 1989; Ramsay, 1989). Furthermore, several studies have shown that the Helvetic nappe system in western Switzerland was affected by SW-NE extension during the NW-SE shortening (Dietrich, 1989). However, there are no 3-D mechanical models for the formation of the Rawil depression that quantified the deformation or attempted to test a particular hypotheses for the formation of the Rawil depression.

We present here 3-D hydrodynamic numerical simulations of viscous flow to quantify the deformation for two tectonic scenarios (see next section) that potentially can explain (i) the combined formation of the Morcles and Doldenhorn fold nappes, and (ii) the formation of the Rawil depression. The Helvetic nappe system and the external crystalline massifs are characterised by

sharp and significant changes in mechanical strength between weak shale-rich sediments, strong limestones and strong basement. Therefore, the simulations require a numerical algorithm that can accurately track the material interfaces for large differences in material properties, and for large deformations. We hence apply a finite element (FE) algorithm based on a Lagrangian formulation combined with re-meshing (von Tscharner *et al.*, 2014). We consider here only linear and power-law viscous flow, and assume therefore that the dominant deformation mechanism during the formation of the fold nappes and the Rawil depression was ductile.

The aim of the study is to apply hydrodynamic models for 3-D viscous flow in order to test and quantify a simplified and potential tectonic scenario for the 3-D evolution of the Morcles and Doldenhorn nappes, and also a scenario for the 3-D formation of the Rawil depression.

4.3. Geological background and potential tectonic scenarios

Figure 4.1a and b shows two cross sections through the Helvetic nappe stack in the Western Swiss Alps. The cross section through the western part of the study area shows from bottom to top the Morcles nappe, the Diablerets nappe, the Mt. Gond nappe and the Sublage nappe (Fig. 4.1a; after Escher *et al.* (1993)). The cross section through the eastern part displays from bottom to top the Doldenhorn nappe, the Jägerchrüz nappe, Gellihorn nappe and Wildhorn nappe (Fig. 4.1b; after Kirschner *et al.* (1999)). The vertical simplified cross sections are perpendicular to the trend of the fold axis and show the projection of the mapped geological units and structures of the region. Young strike-slip faults such as the Rhone fault are not shown on the profiles. The sediments of the Helvetic nappe stack are generally a repetition of limestones, marls, shales and sandstones which were deposited from late Triassic to Early Oligocene on the Helvetic shelf of the European passive margin (Furrer, 1938; Trümpy, 1960; Ramsay, 1989; Epard, 1990; Escher *et al.*, 1993; Pfiffner, 1993). After the last sedimentation the Helvetic nappes were progressively formed by folding and overthrusting. The lowermost nappes, the Morcles and Doldenhorn nappe are autochthonous and parautochthonous, whereas the overlying Diablerets, Mt Gond, Sublage, Jägerchrüz, Gellihorn and Wildhorn nappes (so called Helvetic nappes) are detached from their basement (Escher *et al.*, 1993; Pfiffner, 1993).

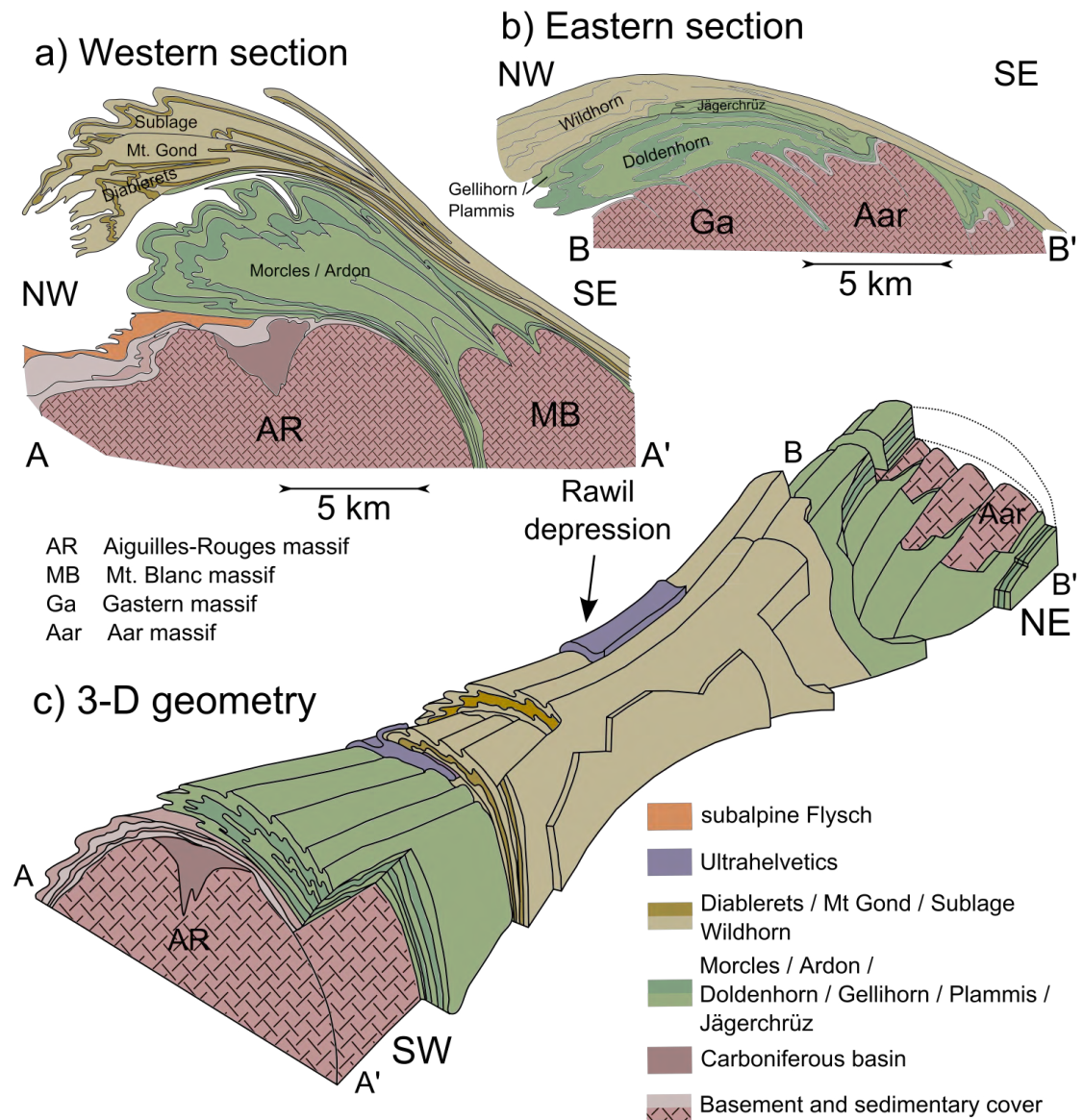


Figure 4.1: a) Cross section in the western part showing the Morcles nappe as well as the overlying Diablerets nappe, Mt. Gond nappe and Wildhorn nappe (reproduced after Escher et al., 1993). b) Cross section in the eastern part of the study area shows the Doldenhorn nappe as well as the overlying Diablerets nappe and Wildhorn nappe (reproduced after Kirschner et al., 1999). c) Schematic 3-D geometry of the axial Rawil depression between the Morcles nappe in the west and the Doldenhorn nappe in the east (reproduced after Ramsay, 1981).

The Morcles nappe represents a typical fold nappe with a prominent overturned limb (Fig. 4.1a). Fold nappes are recumbent folds with amplitudes usually exceeding 10 km, and they have been formed presumably by ductile shearing (Bauville *et al.*, 2013; Dietrich and Casey, 1989; Epard and Escher, 1996; Ramsay *et al.*, 1983). Fold nappes often exhibit a constant sense of shearing and a non-linear increase of shear strain from their normal to their overturned limb which has been observed across the Morcles nappe (Ramsay, 1981). It has been suggested that the Morcles nappe is mainly the result of layer parallel contraction and shearing (Ramsay, 1981), and that it has been deformed together with its underlying crystalline basement (external Mont-Blanc massif). The crystalline basement also exhibits a significant amount of ductile deformation (Escher *et al.*, 1993). The sediments forming the Morcles nappe can be to first order separated into mechanically strong carbonates and mechanically weak shales (Pfiffner, 1993). During the compression the massif carbonates were more competent than the surrounding shales, which led to the buckling characteristics of the Morcles nappe, especially in the normal limb and the frontal area (Fig. 4.1a). During the shortening, the basement deformed to a large extent by ductile deformation and formed a mullion structure. The Doldenhorn nappe exhibits (i) a smaller overall thickness, (ii) a less prominent overturned fold limb that is significantly more sheared and thinned, and (iii) a smaller amplitude than the Morcles nappe (Steck *et al.*, 1999) (Fig. 4.1b). The thickness of the Morcles nappe is between 3.5 km and 5 km (Ramsay, 1981; Escher *et al.*, 1993; Pfiffner, 1993) whereas the thickness of the Doldenhorn nappe is about 2.5 km (Kirschner *et al.*, 1999; Herwegh and Pfiffner, 2005). A possible explanation for these differences is that the weak sediments (especially the Aalenian shales) in the half graben deposits that form now the Doldenhorn nappe have been thinner than the weak sediments in the half graben deposits that form now the Morcles nappe (Loup, 1992; Pfiffner, 1993, 2011). The larger thickness of weak sediments in a deeper half graben in the area of the Morcles nappe would have hence favoured the development of a fold nappe with larger thickness, larger amplitude and less sheared overturned limb. A dominantly ductile deformation behaviour during the formation of the Morcles and Doldenhorn nappe is supported by the fold geometries on several scales (e.g. parasitic folds), the deviation from constant thickness behaviour of the weak shale units, and microstructural observations in carbonate mylonites observed in the overturned limbs of both nappes which indicate viscous deformation by diffusion and/or dislocation creep (Ebert *et al.*, 2008).

One possible tectonic scenario to explain the first-order features of the Morcles and Doldenhorn nappe is that the sediments forming the Morcles and Doldenhorn nappe have been deposited in one half graben with a laterally varying thickness where the thickness was larger on the side of

the Morcles nappe. The Morcles-Doldenhorn basin (i.e. North-Helvetic basin) was deepening towards the SW towards the Dauphinois basin. During the compression, the basin was closed towards the NE (Epard, 1990). This half graben has then been shortened during the Alpine orogeny, and the half graben sediments have been folded, squeezed out of the graben and sheared over the basement. We study here this tectonic scenario with 3-D hydrodynamic simulations.

The Rawil depression, also referred to as the Wildstrubel depression, was first described by Argand (1902-1911) and Heim (1921). The Rawil depression is an axial depression located in W-Switzerland around the border between the cantons of Bern and Valais, and separates geographically the Morcles nappe from the more eastern Doldenhorn nappe (Fig. 4.1c). The depression is characterized by an opposite plunge of fold axes in the Helvetic nappe system and the underlying basement. The fold axis of the Morcles fold nappe plunges to the ENE whereas the fold axes in the more eastern Doldenhorn nappe plunges to the WSW (Fig. 4.1c; after Ramsay (1981)) (Steck *et al.*, 1999). The maximal plunge of the fold axis in both nappes is approximately 30 degrees (e.g. Steck *et al.* (1999)). It was suggested that in the Rawil depression the nappe stack is overprinted by a dextral transtension zone (Cardello and Mancktelow, 2014; Cardello, 2013). In the deepest part of the depression, where the highest nappes are preserved (Ultrahelvetics), oblique normal faults with important displacement are observed (Gasser and Mancktelow, 2010). The evolution during exhumation and cooling from ductile to brittle deformation is documented in this area where ductile deformation led to the axial depression and brittle faulting led to the normal faults (grabens). Due to continuous compression the Helvetic nappe stack was folded and updomed after the nappe stacking (Lugeon, 1914-1918; Masson *et al.*, 1980; Ramsay, 1981; Ramsay *et al.*, 1983; Burkhard, 1988; Ramsay, 1989; Herwegh and Pfiffner, 2005). This led to the exhumation of the external massifs. The normal faults in the Rawil depression indicate orogen parallel extension whereas the exhumation of the external massifs took place due to NS compression (Steck, 1984; Cardello and Mancktelow, 2014). The Rawil depression has been explained with different tectonic scenarios. For example, according to Burkhard (1988) the Aiguilles Rouges massif and the Aar massif were updomed and exhumed on oblique thrusts in the underlying basement. The Rawil depression formed due to a dextral offset in the thrust plane in the crystalline basement. In contrast, Dietrich (1989) and Ramsay (1989) suggested that the Rawil depression formed due to changing thrusting directions. The change in thrusting direction from top-to-the-N to top-to-the-W in the early to late stages of the Alpine collision led to significant fold axis parallel extension (Steck, 1990) and the formation of the axial Rawil depression as well as the culmination of the Aiguilles-Rouges and Aar massifs.

Furthermore, Ramsay (1989) suggested that the Rawil depression could have formed (together with other structures such as the Rhone culmination or the Flaine depression) due to late E-W shortening superposed across all previously formed structures. Another potential scenario to form the Rawil depression was presented by Steck *et al.* (1989) where an oblique Carboniferous graben in the basement acted as a weak zone and caused the formation of the Rawil depression due to N-S compression and E-W extension.

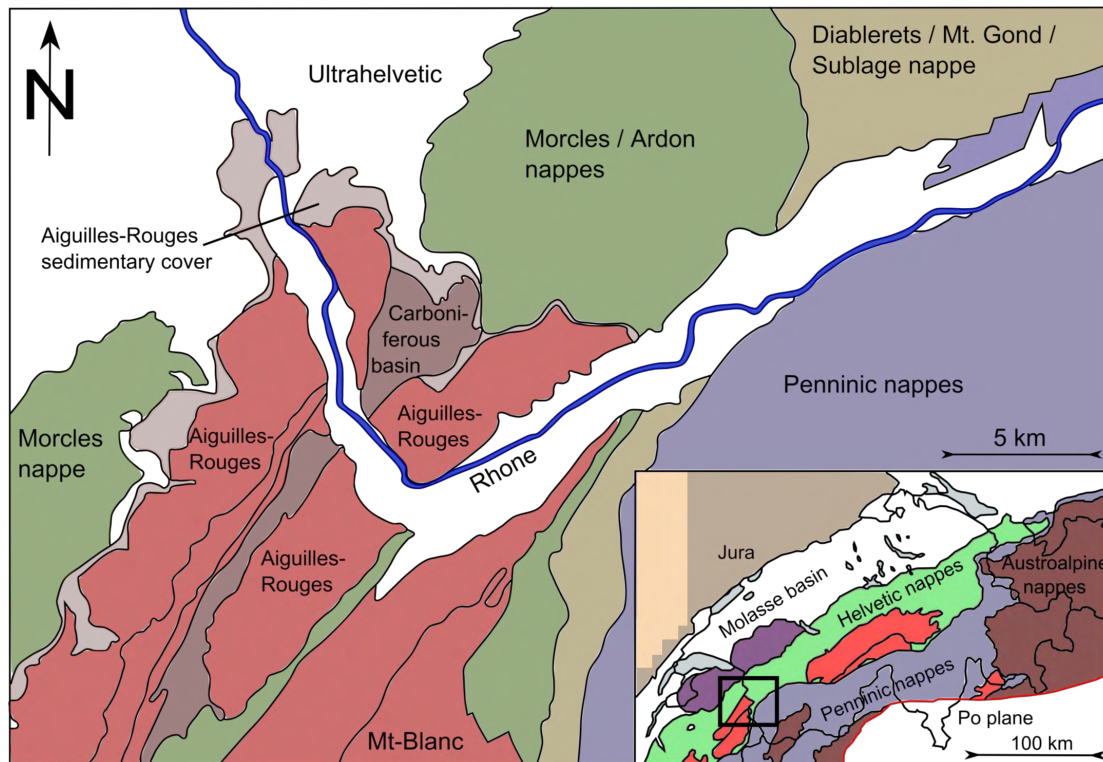


Figure 4.2: Simplified tectonic map of Western Switzerland (simplified after the tectonic map of Switzerland, 1:500000).

We will investigate here scenario which was presented by Steck *et al.* (1989) for the formation of the Rawil depression. Figure 4.2 shows a zoom of the simplified tectonic map of Switzerland of the area west of the Rawil depression. The map shows the Aiguilles-Rouges massif which includes a Carboniferous graben. Such Carboniferous grabens are frequent in the European basement, and in the Helvetic domain their orientation (approximately N-S) may have been oblique to the Alpine shortening direction (approximately NW-SE). During the Alpine shortening

such a Carboniferous graben may have acted as an oblique weak zone in the basement and may hence have influenced the basement deformation and uplift. Potentially, such a graben exists below the Rawil depression and could have been responsible for a laterally variable uplift that might have generated the Rawil depression (Piffner *et al.*, 1997). Today, the Carboniferous graben in the Aguilles-Rouges massif is oriented with a low angle to the strike of the orogen which suggests the graben was rotated during the NW-SE shortening (Fig. 4.2). We study here this potential scenario with 3-D hydrodynamic simulations.

4.4. Numerical Method

The 3-D viscous flow is described by the conservation of momentum and mass for an incompressible, highly viscous fluid (often referred to as Stokes equations). The flow law is either linear or power-law viscous where for the latter the effective viscosity is controlled by the second invariant of the strain rate tensor and the power-law stress exponent, n (see Schmalholz and Schmid (2012) for a 2-D version of the applied equations). The system of governing equations is solved numerically with the finite element method (FEM). In the applied finite element algorithm (termed PINK-3D) a mixed velocity-pressure formulation utilising a structured hexahedral mesh employing tri-quadratic shape functions for velocity (Q2) and piece-wise discontinuous linear shape functions for pressure (P1) (Bathe, 1996) is used (see von Tscherner *et al.* (2014) for an application of the algorithm to 3-D necking during slab detachment).

In the continuity equation we introduce a penalty term and solve the penalised system by applying a Richardson iteration to the reduced velocity Schur complement system (Dabrowski *et al.*, 2008). Non-linearities inherent to the power-law rheology are treated with Picard iterations.

The Stokes problem is solved on a structured hexahedral finite element mesh. The mesh is Lagrangian and thus the nodal coordinates are advected at each time step using the fluid velocity (explicit Euler step). Throughout the deformation, the elements get distorted and thus the mesh quality degenerates. At each re-meshing step, a new structured finite element mesh is generated. Within our 3-D numerical model, we represent all material-interfaces (e.g. between limestone and shale) with a set of marker points. The marker points on the material interfaces are Lagrangian and are advected together with the FE mesh. Initially, the faces of the elements within the mesh conform to the material interface wherever it is possible. However, once re-

meshing has occurred the material interface will intersect the element interiors. We use the material-interface to define the material phase (material properties) on each quadrature point. For a vertical line located at the horizontal coordinates of the quadrature point we determine all intersections with the material-interface. Using the vertical coordinates of these intersection points we are able to determine whether the quadrature point is located inside or outside the volume which is defined by the material-interface. After the re-meshing the finite element mesh is deformed again in a Lagrangian way until the quality of the mesh becomes unsatisfactory. The applied method allows to accurately follow the material-interface with the finite element mesh during the initial development of geometrical instabilities such as folding.

4.5. Simulations

4.5.1. Fold nappe formation

In this section we present a simple 3-D model of fold nappe formation during shortening of a half-graben with laterally varying thickness. For reference, we also perform 3-D cylindrical simulations (with only one finite element in the lateral, along graben, direction) with different half-graben thickness. The models are applied to better understand the formation of the Morcles and Doldenhorn nappe and particularly the lateral change on nappe geometry (Fig. 4.1). We assume that the thickness of weak shale-rich sediments in the half-graben decreases from one side to another, which is in broad agreement with the observed decrease in shale-rich sediments from the section of the Morcles nappe to the section of the Doldenhorn nappe (Pfiffner, 1993, 2011). The aim of the 3-D simulation is to better understand and quantify the impact of laterally varying half-graben and weak sediment thickness on the developing fold nappe.

Model configuration

Figure 4.3 shows the model configuration for both the cylindrical 3-D and full 3-D simulations for fold nappe formation. All geometrical and material parameters are given in dimensionless numbers using the thickness of the competent sedimentary layers H , the matrix viscosity η_M and the background strain rate $\dot{\epsilon}_B$ as characteristic parameters with which all parameters are made

dimensionless. The model consists of a half graben that is formed by material with a viscosity of $\eta_B = 200$ and a power-law stress exponent of $n = 1$ (i.e. Newtonian fluid) which mimics the basement. The half graben is filled with sedimentary layers of different viscosity. The competent layers have a viscosity of $\eta_L = 100$ and a power-law stress exponent of $n_L = 3$. The surrounding sedimentary material (matrix) has a viscosity of $\eta_M = 1$ and a power-law stress exponent of $n_M = 3$. Gravity is ignored. The mechanically strong and weak layers represent limestones and shales, respectively. The model box has an initial length of $L_x = 115$ and a total height of $H_{Model} = 25$ whereas the thickness of each of the competent sedimentary layers is $H = 1$. The maximal height of the basement is $H_B = 17$ whereas the maximal depth of the half graben is $D = 4.2$ and $D = 13.8$ for the shallow and deep part of the half graben, respectively. The cylindrical models consist of only one element in y-direction that is parallel to the cylindrical axis of the forming fold nappe whereas the 3-D model has a width of $L_y = 75$ in y-direction. The 3-D model consists of a varying maximum half graben depth in y-direction where the half graben has a constant maximum depth at the boundaries ($y = 0 - 15$ and $y = 60 - 75$) and a linear change from the deep to the shallow part of the graben in the middle of the model between $y = 15$ and $y = 60$ (Fig. 4.3c and 4.3d). The boundary conditions are free slip on three vertical boundaries (i.e. $x = 0$, $y = 0$ and $y = L_y$, where L_y is the model width in y-direction) as well as on the bottom boundary ($z = 0$). Boundary velocities are prescribed at the fourth vertical boundary ($x = L_x$) to generate horizontal pure shear shortening. During shortening the model width in the y-direction remains constant. The top boundary ($z = H_{Model}$) acts as a free surface. The layers are initially perfectly horizontal and folding initiates around the lateral contact between the sedimentary layers and the basement. With our numerical method we are able to accurately follow the layer geometry with the initial Lagrangian mesh. This is important because during the initial stages of folding the instability is strongest and the fold wavelength is selected. In contrast, the material interface that defines the bottom of the half graben crosses the individual finite elements because this interface does not develop an instability. The re-meshing is performed as soon as the fold amplitude of the competent layers has significantly grown and a fold wavelength has been selected. The resolution is locally increased in the x-direction around the contact point of the competent sedimentary layers with the basement and in z-direction around the competent layers to accurately resolve the folding process.

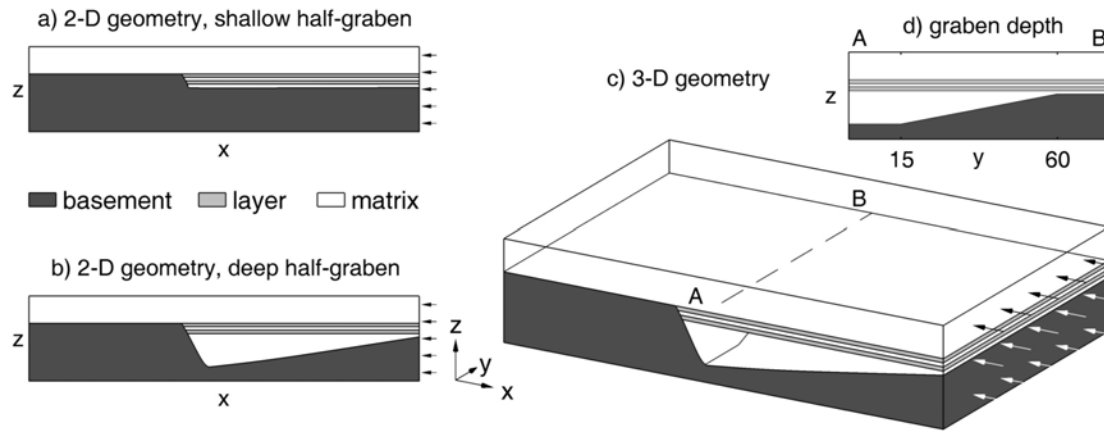


Figure 4.3: 2-D and 3-D model configuration. The dimensionless dimensions of the model box are $115 \times 75 \times 25$. a) 2-D geometry with a shallow half graben. b) 2-D geometry with a deep half graben. c) 3-D geometry with d) laterally varying graben depth where profiles through the shallow and deep graben are similar to a) and b), respectively. Shortening is applied in x-direction, the boundary condition for the top boundary is either pure shear extension or free surface and the boundary condition for all other boundaries is free slip.

3-D cylindrical simulations

We present two simulations for 3-D cylindrical fold nappe formation. The two simulations differ in the initial half graben depth and represent the two end members with a shallow and deep half graben of $D = 4.2$ and $D = 13.8$, respectively. The simulations were performed with an initial numerical resolution of $222 \times 1 \times 59$ elements. Figure 4.4 shows the geometrical evolution for the two simulations, where the colors indicate the distribution of the dimensionless effective viscosity. For both simulations folding initiates around the contact between the competent sedimentary layers and the basement (Fig. 4.4a and 4.4d) where the amplification is much faster and therefore the fold amplitude is larger for the simulation with a deep initial half graben. The faster amplification rate of the folds above a thicker weak horizon is in agreement with analytical results of detachment folding Schmalholz *et al.* (2002). The layers are first buckled and then sheared over the basement to form a recumbent fold nappe with an overturned limb. This overturned limb is more dominant for the simulation with a deep sedimentary basement whereas the deformation is more localized and the fold nappe remains flatter for the shallow half graben. In the same time as the the formation of the fold nappes takes place, the sediment-basement contact forms a cusbate-lobate structure (mullion) which is much more dominant for the simulation with

the deep initial half graben. The stronger localization at the base and the smaller thickness of the fold nappe that develops above the shallower half graben (after 58% bulk shortening) is in broad agreement with the observed differences between the geometry of the Morcles nappe and the Doldenhorn nappe (Fig. 4.1).

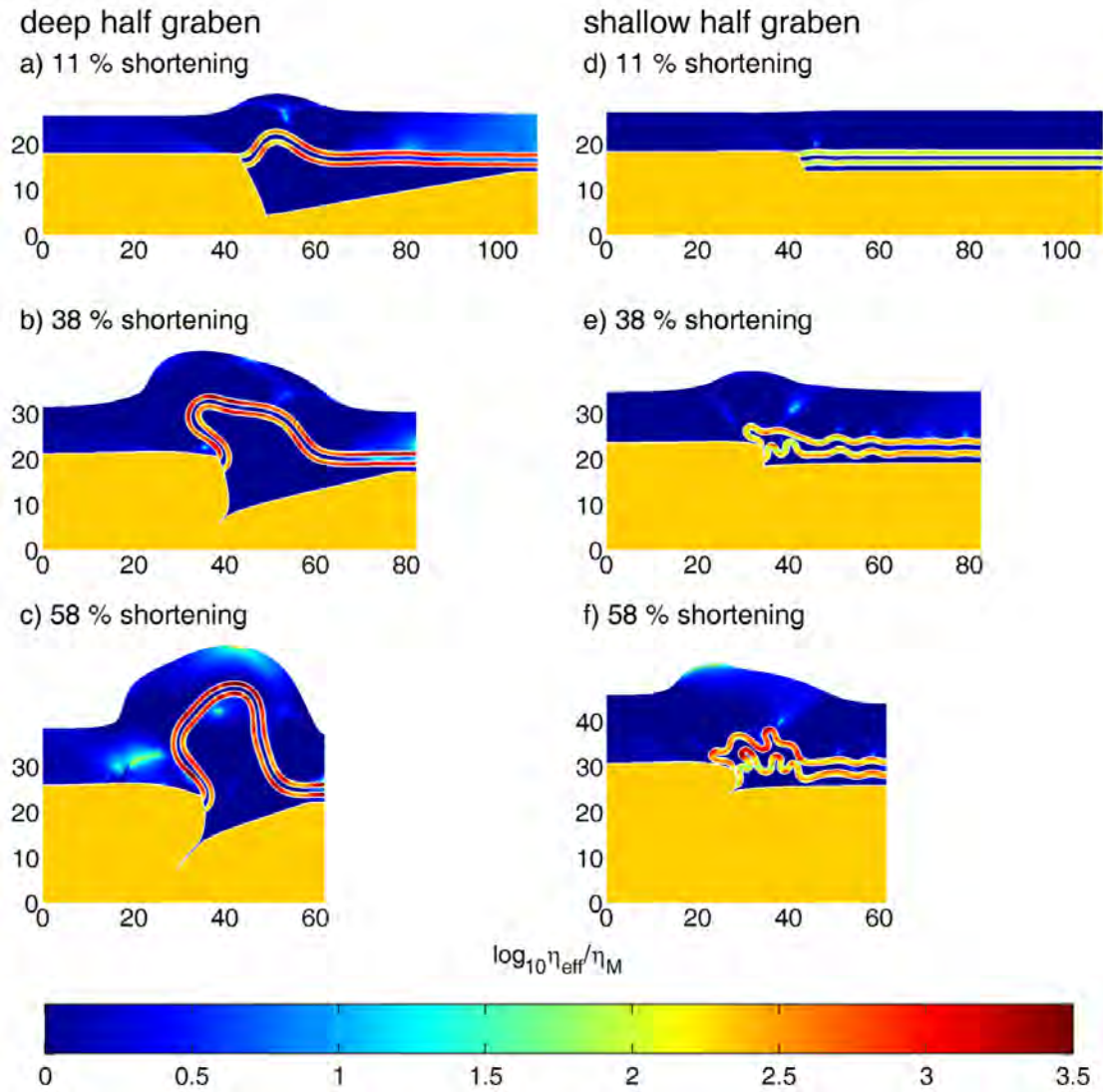


Figure 4.4: Evolution of two cylindrical 3-D simulations for the compression of a deep (a-c) and a shallow (d-f) sediment filled half graben. The colors indicate the dimensionless effective viscosity. Folding initiates around the contact between the competent sedimentary layers and the basement.

3-D simulation with laterally varying half graben depth

The 3-D simulations with a laterally varying graben depth were performed with a numerical resolution of $47 \times 23 \times 13$ elements. The results for this simulation are given in figure 4.5 to 4.7. Figure 4.5 shows the 3-D geometry after 55% bulk shortening. The deformed circles on the basement-sediment and layer-sediment interfaces as well as on the model boundaries quantify the finite strain. The circles have an initial dimensionless diameter of $d/H = 2$ and are deformed using interpolated nodal velocities. The colors on the material interfaces indicate their dimensionless topography. The basement shows higher deformation where the initial graben was shallow. The fold nappe on the side where the initial half graben was deeper shows the highest amplitude and the fold nappe amplitude laterally decreases towards the shallow half graben.

Figure 4.6 shows 8 selected lines on the basement-sediment interface as well as on the top layer interface. Five of them are initially parallel to the x-direction and three are initially parallel to the y-direction. For these lines we show the relative change in length during the deformation. The lateral fold axis parallel extension of the lines which were initially parallel to the y-direction versus the bulk shortening is given in figure 4.6a whereas the shortening of the lines which were initially parallel to the x-direction is given in figure 4.6b. The lateral fold axis parallel extension for all selected lines is relatively small, i.e. up to 5% and is caused by the difference in the rate of amplification along the individual folds. The lateral extension is varying with time for the different lines depending on the formation of other folds in the competent sedimentary layers which cross the corresponding line. The lateral deformation on line 2 for example indicates first extension, when the amplitude of the fold is growing faster on the deep graben side. A new fold which starts to grow later and behind the main fold (where line 4 starts on the deep graben side in figure 4.6c) is bended towards the main fold and causes shortening of line 2. The shortening for the lines parallel to the x-direction is higher, i.e. up to 40% and is highest where the graben is shallow. High values of line shortening indicate thickening of the competent layers during bulk shortening. The shortening of the line is smaller where the amplification of the folds in the competent sedimentary layers is faster.

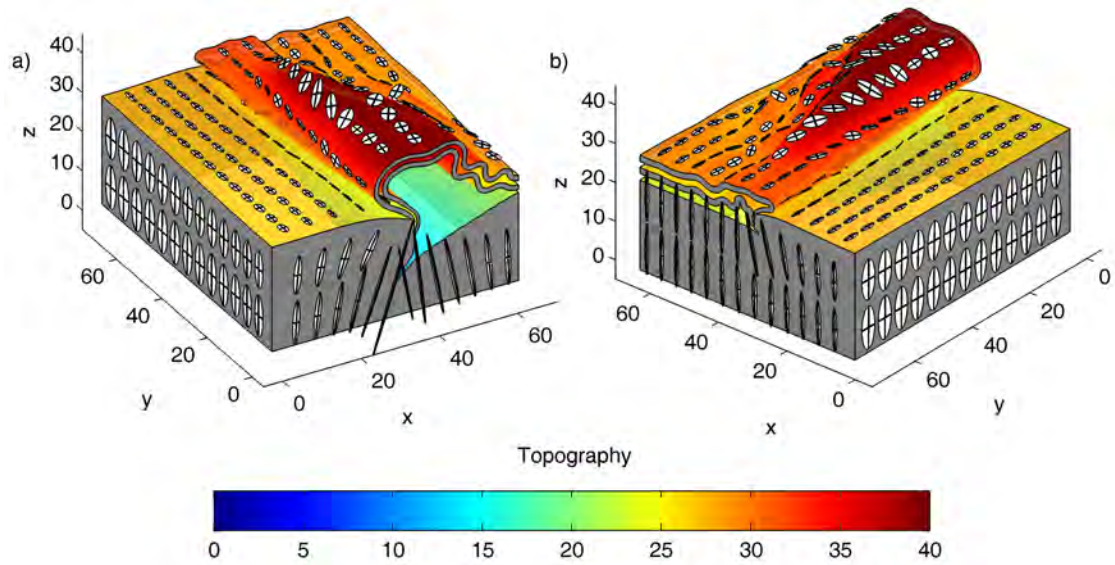


Figure 4.5: Intersection ellipses between the finite strain ellipsoids and the material interfaces on the layer-matrix and basement-matrix interface as well as on the box boundaries within the basement quantifying the total deformation after 55% bulk shortening.

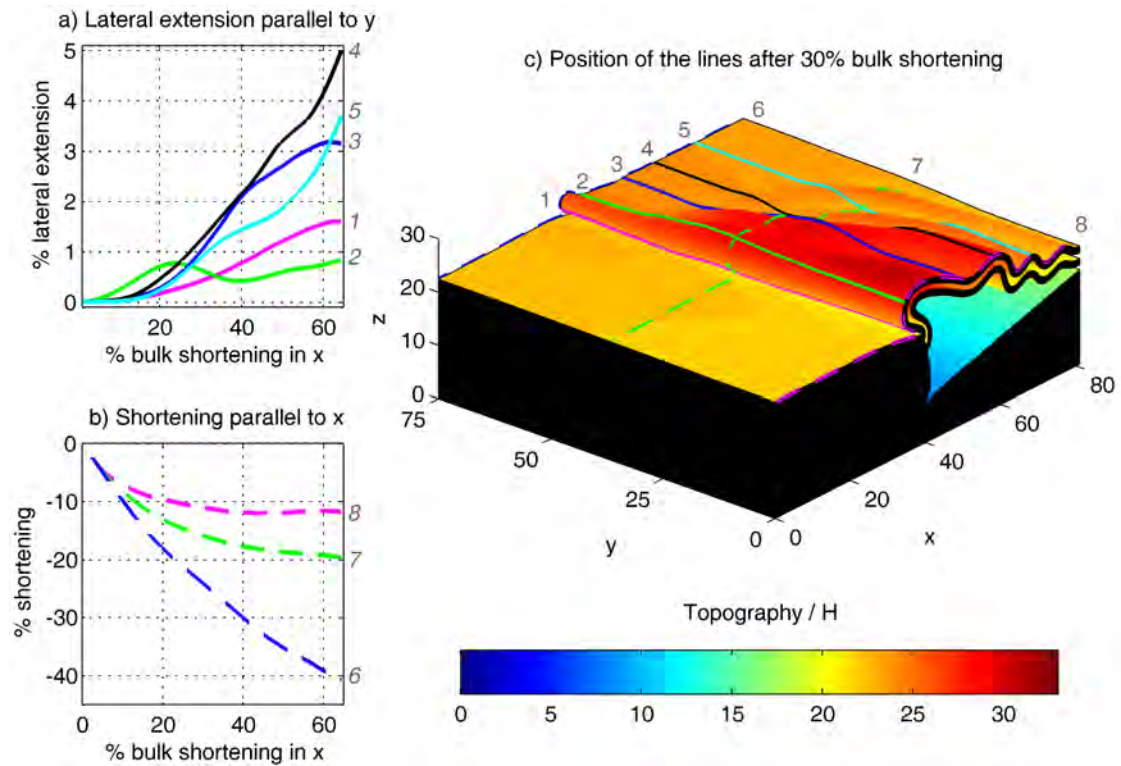


Figure 4.6: Lateral extension in y-direction (a) and shortening in x-direction for five and three selected lines which were initially parallel to the y-direction and x-direction, respectively. The position of these selected lines is given in c) for 30% shortening.

Figure 4.7 shows the normal strain rates in x-direction and y-direction on the top basement-sediment and layer-sediment interfaces. Negative strain rate values (blue) indicate compression whereas positive values (red) indicate extension. The normal strain rate in x-direction (Fig. 4.7a-d) shows extension on the folds antiformes and compression on the synforms. Further, the basement is stronger compressed in x-direction on the side where the half graben is shallow. In this area the normal strain rate in y-direction (Fig. 4.7e-h) indicates extension.

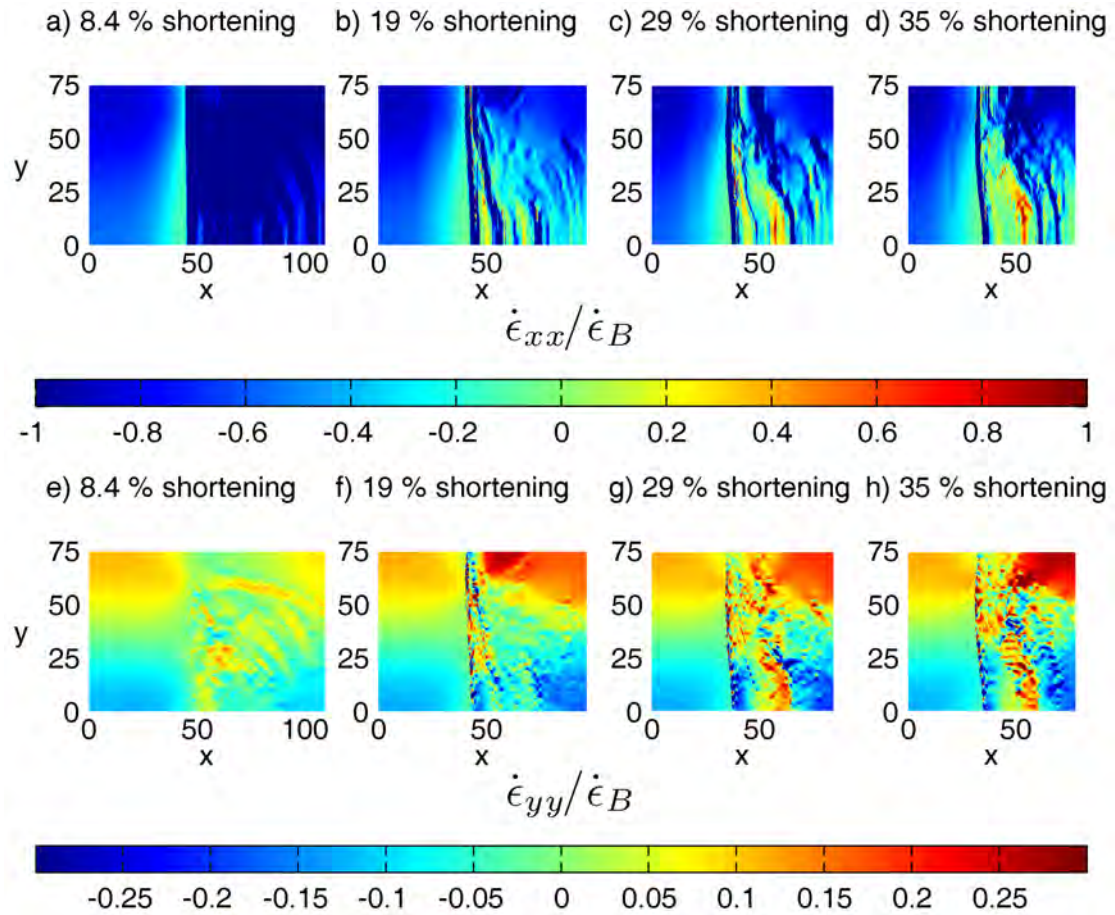


Figure 4.7: Evolution for the 3-D fold nappe simulation with lateral varying graben depth viewing from the top. The colors indicate normal strain rates in x-direction (a-d) and y- direction (e-h) on the top basement-matrix and layer-matrix interfaces. Negative values imply compression.

4.5.2. 3-D formation of the Rawil depression

In this section we test the hypothesis that the Rawil depression was affected by orogen perpendicular compression and orogen parallel extension where a Carboniferous graben in the basement (Fig. 4.2) is assumed to act as a weak zone.

Model configuration

Figure 4.8 shows the model configuration for the simulation of the formation of the Rawil depression. The dimensions of the model box are $60 \times 30 \times 17$ km ($L_x \times L_y \times H_{Model}$). The model is characterised by a competent block which mimics the basement and a sediment filled graben cutting through this basement (mimicing a Carboniferous graben). The graben has an initial width of 4 km and a maximal initial depth of 2 km where the graben sides have an angle of 60° with respect to the horizontal x-direction. The graben and the rest of the model is filled with weaker material (matrix) which mimics the overlying sediments and the fold nappes (i.e. Morcles and Doldenhorn nappe) which we assume are already formed and lie on top of the basement. We assume here for simplicity that after the formation of the fold nappes the top of the basement is horizontal. The basement has an initial thickness of 10km. The orientation of the graben with respect to the x- direction is varied in the different simulations which were performed. On the top surface of the basement we added an initial sinusoidal perturbation in y-direction with a wavelength of $L_y = 30$ km and an initial amplitude of $A_0 = 100$ m. The basement has an initial viscosity which is exponentially decreasing with increasing depth using the following expression:

$$\eta = \eta_0 e^{-z/n\lambda} E_{II}^{1/n-1} \quad (4.1)$$

where η_0 is the viscosity at the top of the basement, z is the depth from the top of the basement, λ is the e-fold length and E_{II} is the second invariant of the strain rate tensor. We assume an initial viscosity of $\eta_0 = 10^{23}$ Pa.s for the top of the basement and an e-fold length of $\lambda = 750$ m (Bauville *et al.*, 2013). In order to track the material properties during the re-meshing steps, the basement is divided in 10 layers of 1km thickness where each of them has a constant initial viscosity. The exponential viscosity profile and the used viscosity profile within the basement are given in figure 4.8d. The minimum viscosity within the basement is set to 10^{19} Pa.s and the matrix has an initial viscosity of $\eta_M = 10^{21}$ Pa.s. The power-law stress exponent of both materials is varied in the performed simulations. An overview on the performed 3-D simulations is given in Table 4.1. The boundary velocities are prescribed for all vertically oriented boundaries ($x = 0$, $x = L_x$, $y = 0$ and $y = L_y$) to generate extension in x-direction and shortening in y-direction. The ratio of the applied strain rates in x- and y-direction is $\dot{\epsilon}_y/\dot{\epsilon}_x = -0.5$. The boundary conditions for the bottom boundary and the top boundary ($z = 0$, $z = H_{Model}$) is free slip and free surface, re-

spectively. The Helvetic nappe stack in the Rawil depression is overprinted by a dextral transtension zone (Ramsay *et al.*, 1983; Burkhard, 1988; Gasser and Mancktelow, 2010; Cardello and Mancktelow, 2014) which indicates dextral shearing. Therefore, the boundary conditions for all vertical boundaries ($x = 0$, $x = L_x$, $y = 0$ and $y = L_y$) are changed after 40% pure shear shortening in y -direction, such that the whole model domain is dextrally sheared along a vertical plane with an angle of 45° with respect to the x -direction (oblique simple shear). The oblique shearing is performed for one selected simulation. Ramsay (1989) suggested that the Rawil depression formed due to late EW compression superposed on all previously formed structures. In order to test this hypothesis we performed a simulation where we apply compressional boundary conditions in x -direction (i.e. the velocities on the boundaries $x = 0$ and $x = L_x$ are prescribed to generate compression, the top boundary acts as free surface and all other boundaries have free slip conditions) after the main compression in y -direction and extension in x -direction.

simulation	graben orientation	n_b	n_m
Rawil_90_1_1	90°	1	1
Rawil_90_3_1	90°	3	1
Rawil_90_3_3	90°	3	3
Rawil_90_6_1	90°	6	1
Rawil_90_6_3	90°	6	3
Rawil_65_1_1	65°	1	1
Rawil_65_3_1	65°	3	1
Rawil_65_3_3	65°	3	3
Rawil_65_6_1	65°	6	1
Rawil_65_6_3	65°	6	3
Rawil_45_1_1	45°	1	1
Rawil_45_3_1	45°	3	1
Rawil_45_3_3	45°	3	3
Rawil_45_6_1	45°	6	1
Rawil_45_6_3	45°	6	3

Table 4.1: Names and varied material parameters for the simulations for the formation of the Rawil depression.

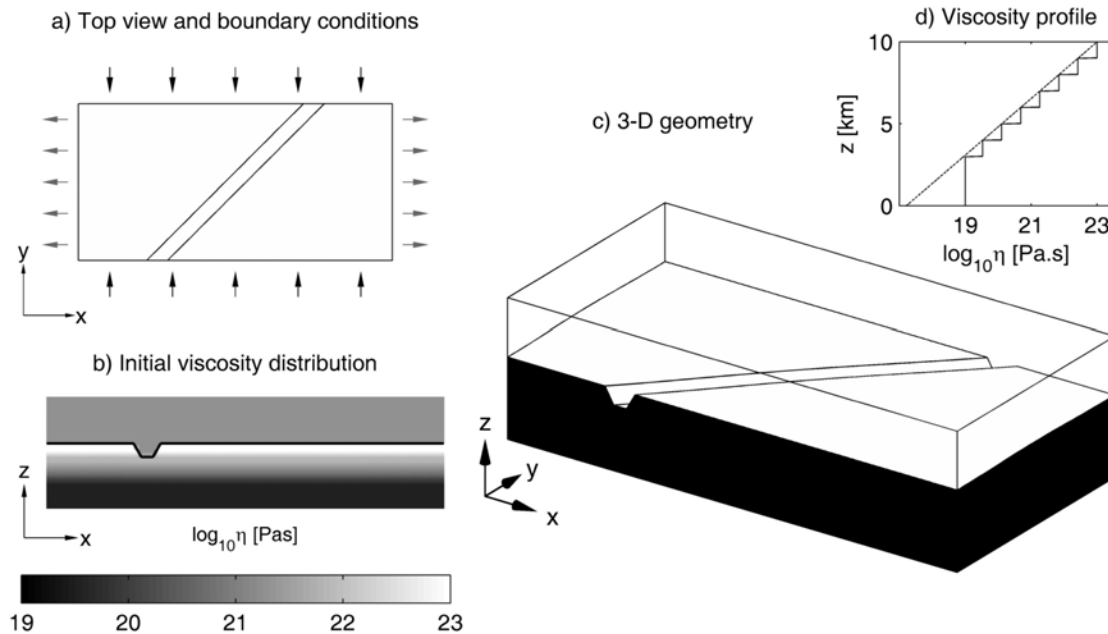


Figure 4.8: Model configuration for the simulations of the formation of the Rawil depression. The dimensions of the model box are $60 \times 30 \times 17$ km. a) Top view with boundary conditions. b) Initial viscosity distribution. c) 3-D geometry. d) Viscosity profile with in the basement where the black line is the true exponential function and the red line represents the viscosity profile which is used in the simulations.

Results

The simulations for the formation of the Rawil depression were performed with a numerical resolution of $50 \times 15 \times 20$ elements. The basement geometry after 40% shortening in y -direction for all simulations with linear sediments (i.e. $n_s = 1$) is given in figure 4.9. Due to the compression in y direction the strong top of the basement is folding upwards on both sides of the graben. This folding is stronger for high power-law stress exponent in the basement (i.e. $n_b = 6$). For high power-law stress exponents in the basement (i.e. $n_b = 3$ and $n_b = 6$) as well as a graben which is oriented with a high angle with respect to the x -direction (i.e. 65° and 90°) a depression is formed along the top of the basement. For the simulations Rawil_45_6_1, Rawil_45_3_1 and Rawil_65_1_1 the basement geometry becomes asymmetric. Due to the vertically free slip boundary conditions the basement is allowed to rotate around a horizontal axis in x -direction. Therefore, the basement topography is significantly lower on one side in y -direction (e.g. Fig. 4.9a). A classification with respect to the basement geometry (i.e. depression in the basement

and asymmetry) for all simulations sorted by the power-law stress exponent used for the sediments is given in figure 4.10.

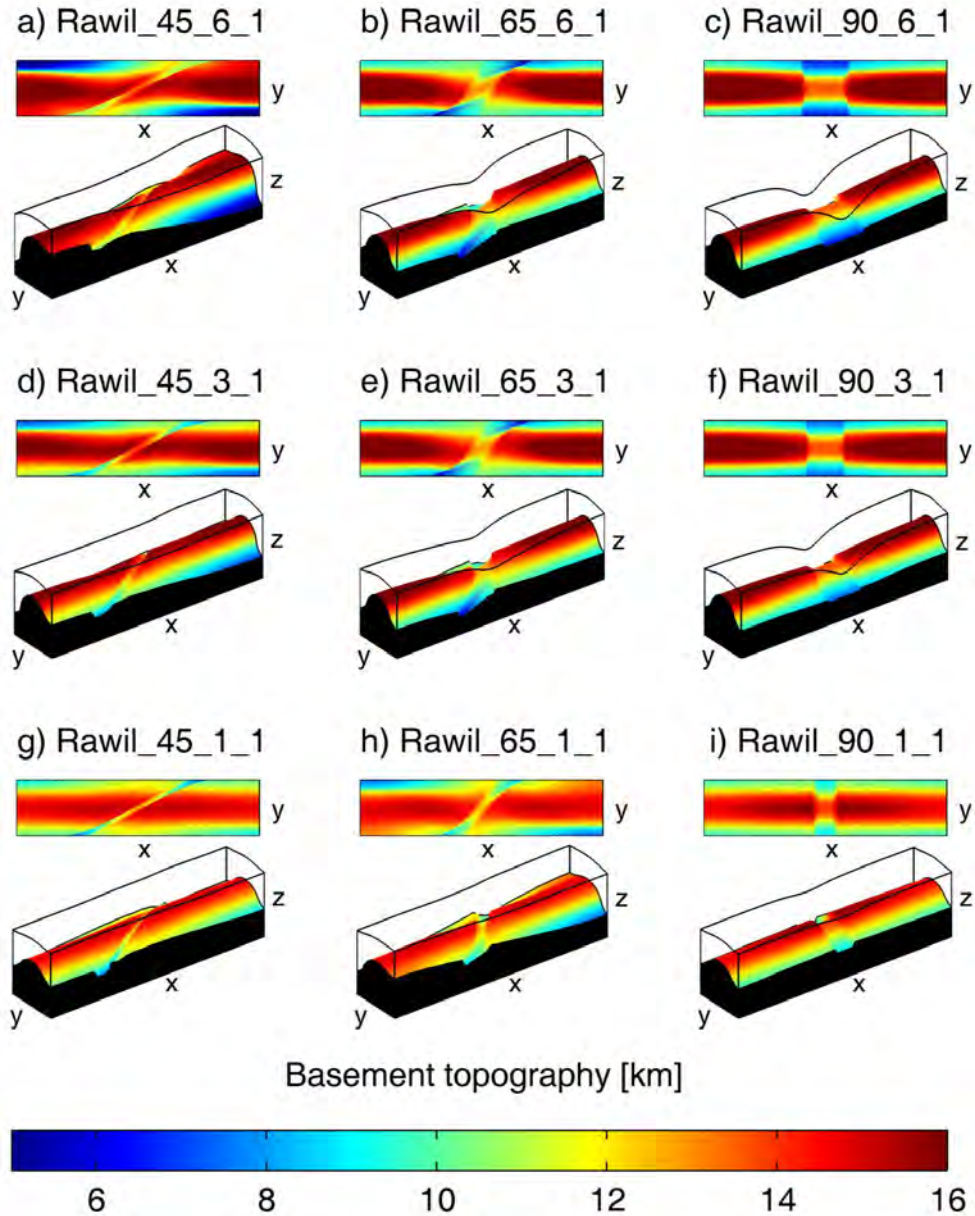


Figure 4.9: Basement geometry after 40% shortening in x-direction for all performed simulations with linear sediments (i.e. $n_s=1$) in top view and 3-D view. The basement geometry becomes asymmetric for the simulations Rawil_45_6_1, Rawil_45_3_1 and Rawil_65_1_1.

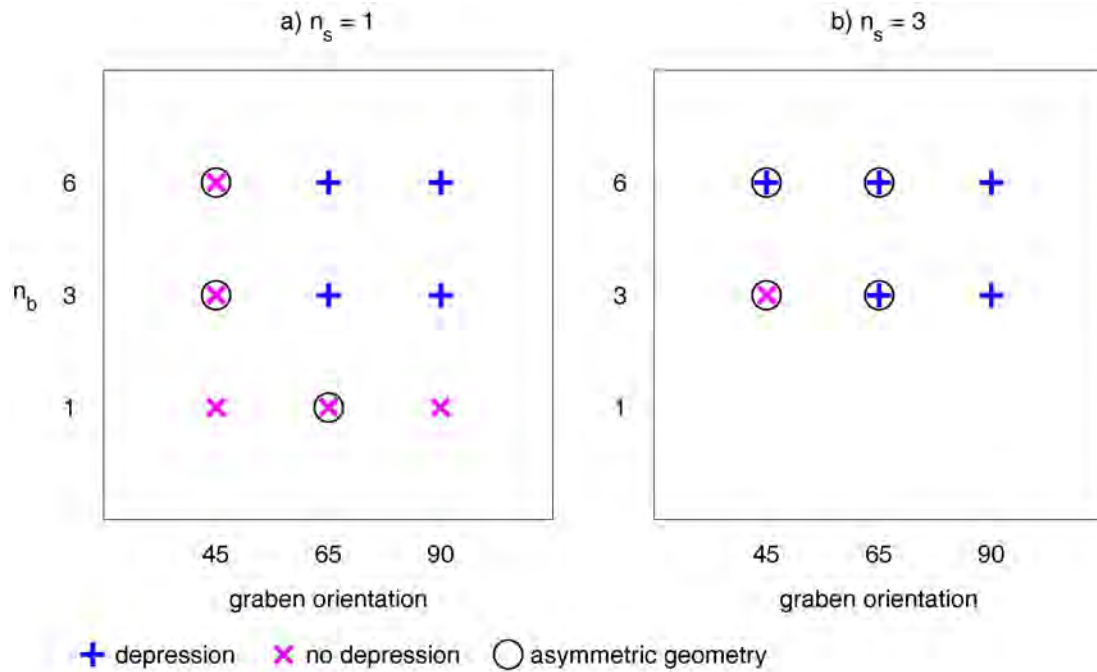


Figure 4.10: Classification of the performed simulations for the formation of the Rawil depression. The simulations are sorted with respect to the power-law stress exponent in the sediment: a) $n_s = 1$ and b) $n_s = 3$. The criteria for the classification is whether the results show a depression in the basement or not and the asymmetry of the basement geometry after 40% shortening in x-direction.

Figure 4.11 shows a profile parallel to the x-direction located in the middle of the model box (i.e. $y = L_y/2$) for the topography of the basement-sediment interface and a passive plane in the sediments for all performed simulations after 40% shortening in y-direction. The passive plane in the sediments is initially perfectly horizontal and located 1km above the basement-sediment interface. The simulations are sorted with respect to the initial orientation of the graben which cuts through the basement. Again the results show that there is no depression formed in the basement if the whole model is Newtonian (i.e. $n_b = n_s = 1$). The simulations where the graben is initially oriented with an angle of 45° with respect to the x-direction form shoulder-like hills on both sides of the Carboniferous graben and no significant depression in the basement. For the simulations with an initial graben orientation of 65° and 90° with respect to the x-direction and non-linear basement material (i.e. $n_b > 1$) a depression in the basement and the passive plane in the sediments is developed during the deformation. The maximum slope of the depression in the basement as well as on the passive plane in the sediments is about 10° .

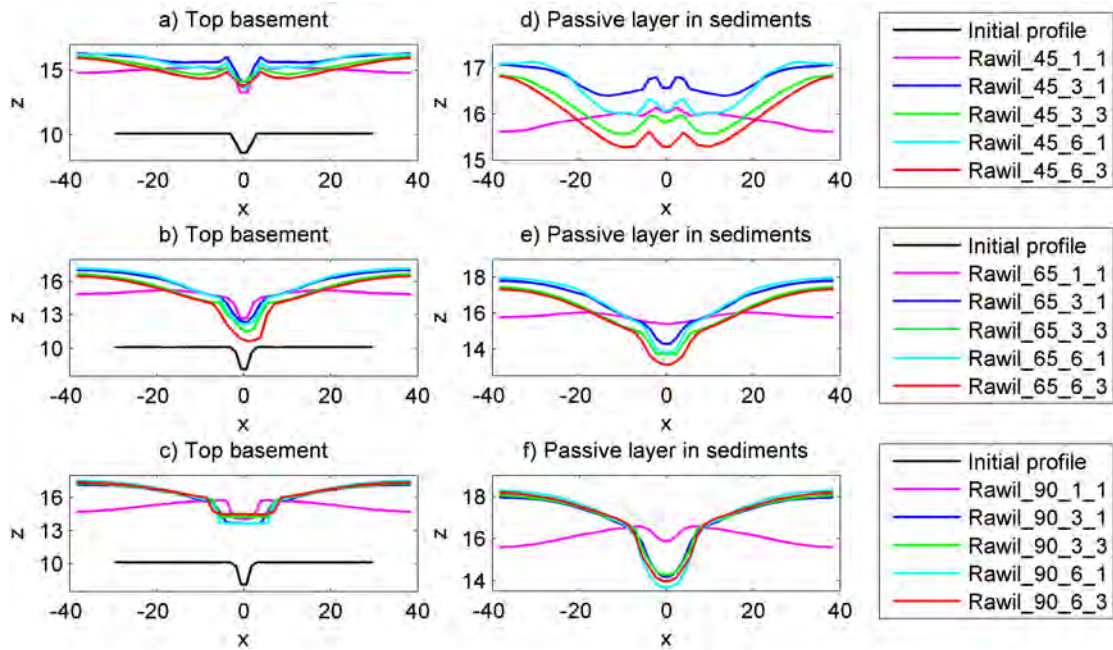


Figure 4.11: Profiles at $y = 0$ for the top basement and a passive plane within the sediment initially located 1km above the basement-sediment interface. The passive plane within the sediments was initially perfectly plane (i.e. without any perturbation). The results are sorted with respect to the initial orientation of the graben for 45° , 65° and 90° given in the subplots a) and d), b) and e) and c) and f), for the topography of the top basement-sediment interface and the passive plane within the sediments, respectively.

From the classification in figure 4.10 and the profiles in figure 4.11 we can see that the simulation Rawil_65_6_1 shows a depression in the basement as well as on the passive plane in the sediments and no asymmetric geometry. Since the simulation with an initial graben orientation of 90° with respect to the x -direction is unlikely (because of the today's orientation of the Carboniferous graben in the Aiguilles-Rouge massif) we choose the simulation with 65° to be the one which fits best to the geometrical data of the Rawil depression.

After the pure shear deformation of simulation Rawil_65_6_1 (i.e. 40% shortening in y -direction) we apply compressional boundary conditions in x -direction to test the hypothesis by Ramsay (1989). After 20% bulk shortening in x -direction we obtain a maximal plunge of the fold axis of 30° on both sides of the depression. The results of this simulation are shown in figure 4.12d and i. As another additional scenario after the pure shear deformation of the simulation Rawil_65_6_1 we also apply an oblique dextral simple shear which is oriented with an angle of

45° with respect to the x-direction. The velocities are prescribed on all vertical boundaries (i.e. $x = 0$, $x = L_x$, $y = 0$ and $y = L_y$). The bottom boundary condition is free slip and the top boundary is stress free. Figure 4.12 shows the evolution for the simulation Rawil_65_6_1 for the pure shear deformation and the oblique dextral simple shear deformation as well as the deformed circles quantifying the total deformation on the basement-sediment interface and the model boundaries. The circles have an initial diameter of $d = 1.2$ km and are deformed using interpolated nodal velocities. The colors indicate the top basement topography. The basement is strongly deformed on the base of the model box where it has a low viscosity due to the prescribed decrease of the viscosity with depth. During the compression in y-direction and the extension in x-direction the basement is updomed and forms a depression where the graben cuts through the basement. In the same time the weak graben in the basement is rotated. During the oblique simple shear the whole model box is further extended parallel to the fold axis in the basement, compressed perpendicular to the fold axis as well as rotated in clockwise direction. The amplitude of the developed depression in the basement as well as on the passive plane in the sediments slightly increases during the simple shear deformation.

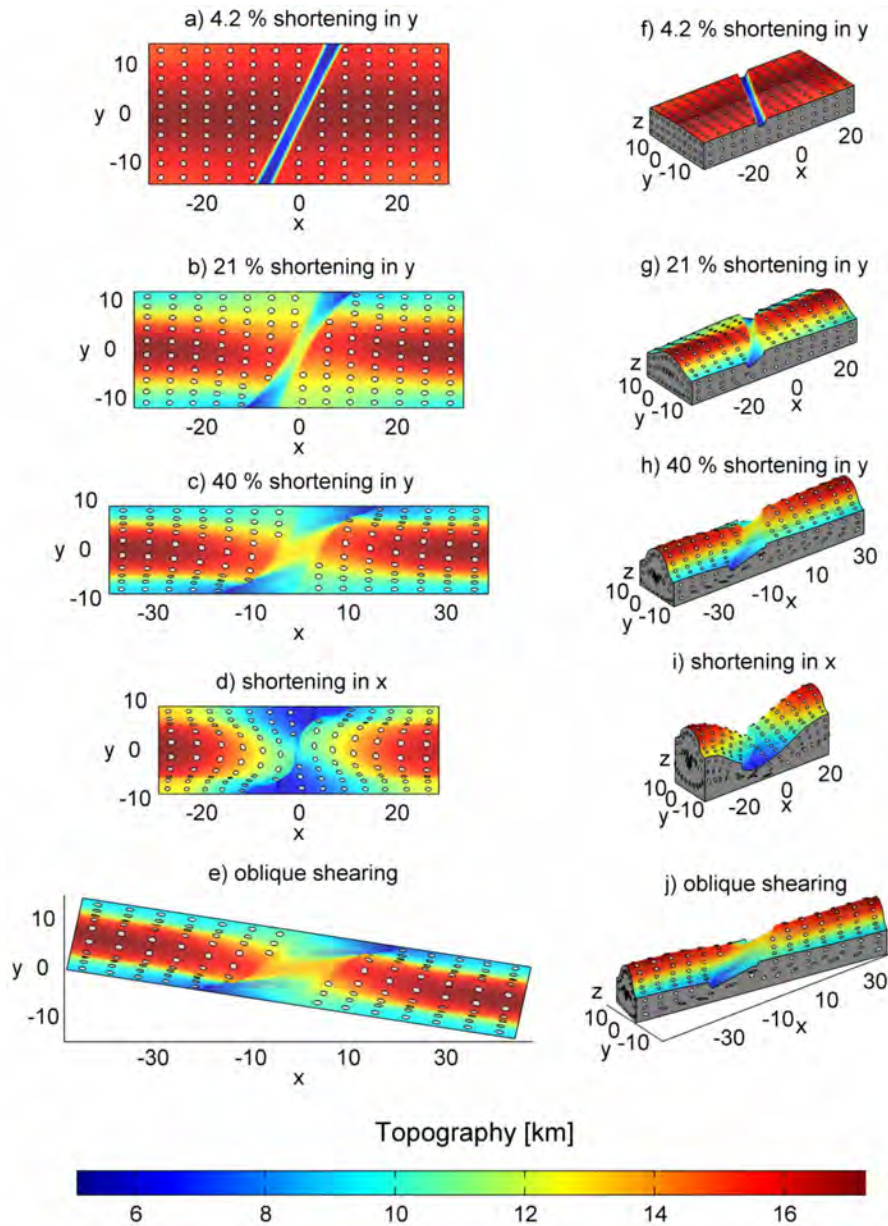


Figure 4.12: Evolution for a simulation for the Rawil depression with an initial graben orientation of 65° with respect to the x-direction, a power-law stress exponent of $n_s = 1$ and $n_b = 6$ for the sediments and the basement, respectively. The colors on the basement-sediment interface indicate the basement topography. The deformed circles on the basement-sediment interface as well as the model box boundaries quantify the total deformation. The circles have an initial diameter of $d = 1.2$ km and are deformed using interpolated nodal velocities.

4.6. Discussion

The cylindrical simulations for the formation of the Morcles and Doldenhorn nappes support the hypothesis that the weak sediments in the half graben deposits forming now the Doldenhorn nappe have been thinner than the sediments in the half graben deposits forming the Morcles nappe, and that this different thickness controlled the different deformation style (Pfiffner, 1993, 2011). The deformed geometry of the simulation with the deep initial half graben shows similarities with the Morcles nappe. The layers which were first buckled and then sheared over the basement form a recumbent fold nappe with an overturned limb (Fig. 4.4c). The deformation is more localized and the entire fold nappe remains thinner for the simulation with thinner sediments in the half graben. This geometry is similar to the Doldenhorn nappe (Fig. 4.4f). During fold nappe formation the basement-sediment interface forms a cusate lobate structure (mullion). The orientation of this cusate-lobate structure is opposite to the orientation of the cusate-lobate structure in the basement below the Morcles and Doldenhorn nappes (Fig. 4.4c, f and Fig. 4.1a, b). This problem may be solved with an additional prescribed drag velocity in the positive x-direction at the bottom model boundary. A smaller initial half graben thickness can explain (i) the stronger shear deformation in the overturned limb of the Doldenhorn nappe compared to the one of the Morcles nappe, (ii) the smaller overall thickness of the Doldenhorn nappe compared to the one of the Morcles nappe, and (iii) the smaller fold amplitude of the Doldenhorn nappe.

The full 3-D simulation with laterally varying graben depth shows small amounts of internal lateral extension in the y-direction in the competent sedimentary layers although the bulk extension in the y-direction was zero (Fig. 4.6, Fig. 4.7 e to h). The amplitude of the forming fold nappe is higher for the deeper half graben, whereas the deformation is more localized for the shallow half graben where the fold nappe remains thinner. Laterally, the fold nappe amplitude is decreasing towards the shallow half graben (Fig. 4.5). The difference in the amplification rates leads to lateral fold axis parallel extension of up to 5%. Dietrich (1989) measured fold axis parallel extension as well as extension which is at high angle to the fold axis in the Helvetic nappes around the Rawil depression. From pressure shadows and conjugated veins they obtained fold axis parallel extension of more than 100%. From fold axis parallel sections Dietrich (1989) calculated fold axis parallel extension of 60% for the southwestern slope of the Rawil depression and up to 120% in the northeastern slope. These calculations and measurements significantly exceed

the lateral fold axis parallel extension which we obtain from the difference in the amplification rates in our models (up to 5%, Fig. 4.6). Therefore, a bulk fold axis parallel extension, as we consider in the simulations for the formation of the Rawil depression, is needed to explain these observed structures and measured extension values around the Rawil depression. However, the small internal extension of up to 5% is sufficient to generate extensional brittle structures such as veins and joints.

The performed 3-D simulations for the formation of the Rawil depression show the first order impact of an oblique graben (representing a weak zone) on the updoming of the basement during shortening. The simulations also show that it is possible to form a depression by horizontal compression and perpendicular extension of a basement with an oblique weak zone. The best fitting simulation for the formation of the Rawil depression is the simulation Rawil_65_6_1 with a graben orientation of 65° with respect to the x-direction, a power-law stress exponent of $n_b = 6$ in the basement and Newtonian sediments (i.e. $n_s = 1$). The results for this simulation show a depression in the basement as well as in the sediments and no asymmetric geometry of the basement. Some of the simulations show a asymmetric basement geometry, especially when we use a power-law stress exponent of $n_b > 1$ and $n_s = 3$. The asymmetric basement geometry is characterized by a significantly lower basement topography and significantly steeper plunge (almost vertical) on one side of the model box. If we compare this geometry with the basement geometry of the Aiguilles-Rouges / Mt. Blanc massifs and the Aar massif, this asymmetric basement geometry seems unrealistic (Pfiffner *et al.*, 1997). The formation of the asymmetric basement geometry is likely because of the free slip boundary conditions which allow the basement to rotate around a horizontal axis in x-direction. When we fix the vertical movement of the vertical boundaries we prevent the basement from becoming asymmetric. However, the amplitude of the depression in the basement remains the same. The amplitude of the depression on the passive plane in the sediments becomes larger with higher power-law stress exponents in the sediments (i.e. $n_s > 1$). The maximal slope in the depression in x-direction is 10° which is not as high as in the Rawil depression where we have slopes of up to 30° . The highest depression amplitudes are obtained with a graben which is oriented with an angle of 65° or 90° with respect to the x-direction. However, based on the today's orientation of the Carboniferous graben in the Aiguilles-Rouges massif (Fig. 4.2), the initial graben orientation of 90° with respect to the x-direction is improbable. The simulation results indicate that shortening of a basement with an oblique graben generates a depression but also that this process alone is not sufficient to generate the observed local plunge of the fold axis of approximately 30° . Hence, additional processes

must have been active to generate the observed plunge of the Rawil depression. One possible scenario to obtain a larger plunge is a later E-W shortening of the already formed structure. The simulation showed that it is possible to obtain 30° plunge on both sides of the depression after additional 20% bulk shortening in x-direction. However, there is no evidence in the field for such late E-W shortening.

The applied models are significantly simplified and effects such as a temperature dependent viscosity or a plastic yield strength have not been considered. A temperature dependent viscosity may cause a larger shear localization within the overturned limbs of the modelled fold nappes as shown by (Bauville *et al.*, 2013). A plastic yield strength may have affected especially the deformation in the upper part of the model above the fold nappes. Furthermore, during the Alpine deformation there was likely a significant amount of simple shear with a top-to-the NW (or to the W?) shear sense and also some amount of vertical flattening. Such simple shear and flattening has also been ignored in our simple models. Such additional deformations will be investigated in future studies.

4.7. Conclusions

4.8. Conclusions

We performed 3-D numerical simulations of viscous flow to study the formation of fold nappes during the inversion of a half graben with laterally (i.e. along the graben axis) varying thickness. The half graben was filled at the top with mechanically competent layers of equal thickness and below with weak material of correspondingly laterally varying thickness. The simulations show that the thickness of weak material in the half graben has a significant impact on the fold nappe evolution. Fold nappes that are generated from a thicker half graben have (i) larger amplitudes, (ii) a less sheared and thinned overturned limb, and (iii) a larger nappe thickness than fold nappes that are generated from a thinner half graben. These three differences are observed between the Morcles and Doldenhorn nappes. Our simulations therefore support the field based interpretations that the first order structural differences between the two nappes are due to a different pre-Alpine thickness of the half graben in which the sediments that build now the two nappes have been deposited during mainly the Mesozoic. The simulations also show that during

the shortening the half graben is closed and forms a mullion-like structure which also agrees with field observations. The viscous flow simulations can generate many first order features of the Morcles-Doldenhorn nappe system and suggest that ductile deformation (and not brittle) was likely the dominant deformation behaviour during fold nappe formation and related basement deformation. The simulations also show that the laterally varying fold amplification causes a fold-axis-parallel extension of up to 5% in the layers although the bulk extension is zero. Such extension could explain brittle extensional structures that are observed in the competent layers of the fold nappes. However, this internal extension cannot explain the overall orogen-parallel extension in the Helvetic nappe system which is significantly larger.

We also performed 3-D numerical simulations of viscous flow to quantify the impact of an oblique graben in the basement on the basement uplift during shortening accompanied by orthogonal extension. The results show that the half graben can cause a laterally varying basement uplift which generates a depression above the half graben. The amplitude of the depression depends on the initial orientation of the graben and the power-law stress exponent of the basement and sediments. The maximal axial plunge of the modelled depression is only approximately 10 degrees whereas the maximal observed plunge of the Rawil depression is approximately 30 degrees. The results therefore indicate that an oblique graben in the basement may have contributed to the formation of the Rawil depression but that additional processes are required to generate the observed geometry of the Rawil depression.

Acknowledgements

We thank Dave May for his helpful comments on the description of the numerical method. The data presented in this paper are the result of forward numerical simulations (see Sec. 2). This work was supported by SNF grant no. 200021_131897 and the University of Lausanne.

References

- Argand E., 1902-1911: **Coupes géologiques des Alpes occidentales**, Matériaux pour la Carte Géologique de la Suisse n.s. 31
- Bathe K.-J., 1996: **Finite Element Procedures**, Prentice hall, Inc., New Jersey
- Bauville A., Epard J.-L. and Schmalholz S., 2013: **A simple thermo-mechanical shear model applied to the Morcles fold nappe (Western Alps)**, *Tectonophysics* 583, 76–87
- Burkhard M., 1988: **L'Helvétique de la bordure occidentale du massif de l'Aar (évolution tectonique et métamorphique)**, *Eclogae Geologicae Helveticae* 81, 63–114
- Cardello G., 2013: **Cretaceous syn-sedimentary faulting in the Wildhorn Nappe (SW Switzerland)**, *Swiss Journal of Geoscience*
- Cardello G. and Mancktelow N., 2014: **The Rawil depression**, Diss., ETH zurich, Nr. 21176 107, 223–250
- Casey M. and Dietrich D., 1997: **Overthrust shear in mountain building**, *Evolution of Geological Structures in Micro- to Macro-scales*, Springer pages 119–142
- Dabrowski M., Krotkiewski M. and Schmid D. W., 2008: **MILAMIN: MATLAB-based finite element method solver for large problems**, *Geochemistry Geophysics Geosystems* 4
- Dietrich D., 1989: **Fold-axis parallel extension in an accurate fold-and-thrust belt: the case of the Helvetic nappes**, *Tectonophysics* 170, 183–212
- Dietrich D. and Casey M., 1989: **A new tectonic model for the Helvetic nappes**, *Alpine Tectonics*, Geological Society Special Publication 54, 47–63
- Ebert A., Herwegh M., Berger A. and Pfiffner A., 2008: **Grain coarsening maps for polymineralic carbonate mylonites: A calibration based on data from different Helvetic nappes (Switzerland)**, *Tectonophysics* pages 128–142
- Epard J.-L., 1990: **La Nappe de Morcles au Sud-Ouest du Mont-Blanc**, *Mem. Geol. Lausanne* page 165 pp.

- Epard J.-L. and Escher A., 1996: **Transition from basement to cover: a geometric model**, Journal of Structural Geology 18, 333–548
- Escher A., Masson H. and Steck A., 1993: **Nappe geometry in the Western Swiss Alps**, Journal of Structural Geology 15, 501–509
- Furrer H., 1938: **Geologische Untersuchungen in der Wildstrubelgruppe, Berner Oberland**, Mitt. Natf. Ges. Bern pages 35–177
- Gasser D. and Mancktelow N., 2010: **Brittle faulting in the Rawil depression: field observations from the Rezli fault zones, Helvetic nappes, Western Switzerland**, Swiss Journal of Geoscience 103, 15–32
- Heim A., 1921: **Geologie der Schweiz, Band II**, Tauchnitz Verlag Gmbh, Leipzig
- Herwegh M. and Pfiffner O., 2005: **Tectono-metamorphic evolution of nappe stack: A case study of the Swiss Alps**, Tectonophysics 404, 55–76
- Kirschner D., Masson H. and Sharp Z., 1999: **Fluid migration through thrust faults in the Helvetic nappes (Western Swiss Alps)**, Contributions to Mineralogy and Petrology 136, 169–183
- Loup B., 1992: **Evolution de la partie septentrionale du domain helvétique en Suisse occidentale au Trias et au Lias: contrôle par subsidence thermique et variations du niveau marin**, Publications du département de géologie et de paléontologie, Université de Genève, Genève 12
- Lugeon M., 1914-1918: **Les Hautes calcaires entre la Lizerne et la Kandern: Wildhorn, Wildstrubel, Balmhorn et Torrenthorn: explication de la carte spéciale no. 60**, Matériaux pour la carte géologique de la Suisse. Nouvelle série 60
- Masson H., Herb R. and Steck A., 1980: **Helvetic Alps of Western Switzerland**, Geology of Switzerland, A Guide Book. Part B. Birkhauserverlag, Basel pages 109–153
- Pfiffner A., 1993: **The structure of the Helvetic nappes and its relation to the mechanical stratigraphy**, Journal of Structural Geology 15, 511–521
- Pfiffner A., 2011: **Structural Map of the Helvetic Zone of the Swiss Alps, including Vorarlberg (Austria) and Haute Savoie (France), 1:100000**, Geological Special Map 128. Explanatory notes.

- Pfiffner A., Lehner P., Heitzmann P., Mueller S. and Steck A., 1997: **Deep structure of the Swiss Alps: Results of NRP 20**, Birkhäuser Verlag, Basel, Boston, Berlin
- Ramsay J. G., 1981: **Tectonics of the Helvetic Nappes**, Geological Society, London, Special Publications 9, 293–309
- Ramsay J. G., 1989: **Fold and fault geometry in the western Helvetic nappes of Switzerland and France and its implication for the evolution of the arc of the Western Alps**, Geological Society, London, Special Publications 45, 33–45
- Ramsay J. G., Casey M. and Kligfield R., 1983: **Role of shear in development of the Helvetic fold-thrust belt of Switzerland**, *Geology* 11, 439–442
- Schmalholz S. M. and Schmid D. W., 2012: **Folding in power-law viscous multilayers**, *Philosophical Transactions of the Royal Society A*
- Schmalholz S. M., Podladchikov Y. Y. and Burg J.-B., 2002: **Control of folding by gravity and matrix thickness: Implications for large-scale folding**, *Journal of Geophysical Research* 107
- Steck A., 1984: **Structures de déformations tertiaires dans les Alpes centrales (transversales Aar-Simplon-Ossola)**, *Eclogae geol. Helv.* 77
- Steck A., 1990: **Une Carte des zones de cisaillement ductile des Alpes Centrales**, *Eclogae geol. Helv.* 83, 603–627
- Steck A., Epard J.-L., Escher A., Marchand R., Masson H. and Spring L., 1989: **Coupe tectonique horizontale des Alpes centrales**, *Mémoires de Géologie*, Université de Lausanne, Lausanne
- Steck A., Bigioggero B., Piaz G. D., Escher A., Martinotti G. and Masson H., 1999: **Carte tectonique des Alpes de Suisse occidentale et des régions avoisinantes, 1:100000**, Carte géologique spéciale n 123, Swiss National Hydrological and Geological Survey
- Trümpy R., 1960: **Paleotectonic evolution of the central and western Alps**, *Bull. Soc. Geol. Am.* 71, 843–908
- von Tscharner M., Schmalholz S. and Duretz T., 2014: **Three-dimensional necking during viscous slab detachment**, *Geophysical Research Letters* 41, 4194–4200

5 Discussion

In chapter 2 we showed that the presented algorithm with a deformable lagrangian mesh can accurately resolve small geometrical perturbations on material interfaces and reproduce the analytical solutions for several hydrodynamic instabilities. During large strain deformation the coordinates of the material interface that cross the individual elements are deformed together with the deforming Lagrangian mesh. The deformation of the material-interface is consistent with the applied numerical finite element approximation. Therefore, it is not necessary to interpolate nodal velocities on the interface coordinates in order to advect the interface points. Furthermore, the velocities around material-interfaces with strongly varying viscosities are accurate even if the interfaces cross the individual finite element (Fig. 2.3). Based on this the presented algorithm is suitable to simulate high strain deformation structures which emerge due to hydrodynamic instabilities. During the initial stages of the deformation when the instability amplitudes are still low the material interfaces are accurately resolved and followed with the initial finite element mesh. During the low amplitude stage the deformation is highly sensitive to small perturbations on the material interface geometry and on the intra-layer stress distribution. On the other hand during the high amplitude stages the deformation is less sensitive to the interface geometry and large strain deformation is simulated with re-meshing and element cutting material interfaces. If higher order time integration schemes such as Runge-Kutta are applied, the movement of the material interfaces and the FE mesh can be made more accurate. In order to test the accuracy of the 3-D algorithm for large strain deformation, results for 3-D cylindrical Rayleigh-Taylor diapirism and single layer folding with different re-meshing szenarios were compared with the results of another 2-D algorithm (Fig. 2.5). In the re-meshing test we showed the importance of an initial Lagrangian mesh to accurately follow the initial perturbations on the material interfaces. Further the test showed the importance of the coice of the first re-meshing time step that should be performed not until the amplitude of the material interface is significant, that is, not until the wavelength of the emerging structure has been selected. Until now we did not implement a special metric to determine if re-meshing is necessary or not. When we remesh after each timestep our method is similar to the Eulerian finite element method in combination with a particle-in-cell scheme (FE-PIC) (Moresi *et al.*, 2007; Thielmann *et al.*, 2014). The sim-

ulations performed for the re-meshing test showed that our method is more suitable to model large strain deformation of instabilities than the FE-PIC method.

The presented 3-D results in chapter 2 show that the algorithm yields smooth stress fields in folded material for viscous and visco-elastic fluids (Fig. 2.6). Furthermore, the 3-D results presented in chapter 3 and chapter 4 show that algorithm provides smooth viscosity fields (Fig. 2.8, Fig. 2.12) and strain rate fields (Fig. 2.15) within a material after several re-meshing steps. Hence, the presented algorithm is useful, if certain quantities such as stress, strain or viscosity have to be calculated on deformed 3-D surfaces.

Since the algorithm is written in Matlab (i.e. the algorithm is not in parallel) other numerical algorithm may be much faster. Therefore, it may be of interest to translate the presented FE algorithm to another programming language as for example C++ or Fortran.

Until now, we did not implement any interpolation of the stored elastic stress between the old and new mesh. Therefore, the elastic or visco-elastic rheology can currently only be used without re-meshing.

The problem sizes treated with PINK-3D as part of this PhD thesis reached up to 650'000 degrees of freedom. One timestep at the maximum problem size required approximately 19 hours.

Compared to other algorithms the presented method has advantages as well as disadvantages:

Advantages

- Accurate resolution of initial geometrical instabilities
- Accurate tracking of the material interfaces
- Interpolation is only necessary during re-meshing
- Free surface boundary conditions

Disadvantages

- Performance, possible degrees of freedom and speed
- Rheology (e.g. temperature dependent viscosities, plasticity or elasticity for large strain)

In general, there are several things which can be approved or added to the presented numerical algorithm:

- Metric for re-meshing
- Interpolation of the stored elastic stresses and power-law viscosities during the re-meshing steps
- Performance
- Translation to C++ or Fortran - Parallelization
- Plasticity (visco-elasto-plastic rheology)
- Temperature solver and temperature dependent viscosity
- Adaptive timestep
- Higher order time integration schemes such as Runge-Kutta

The application of the algorithm to viscous necking during slab detachment presented in chapter 3 showed that the evolution of necking with progressive bulk slab extension is only weakly dependent on the slab size, the slab shape, the width of the mantle adjacent to the lateral slab boundaries and the rheology of the mantle (i.e. linear or non-linear). Therefore, we are able to predict the evolution of necking with increasing slab length for many other slab configurations with the same initial material parameter configurations without performing additional 3-D simulations. However the evolution of the necking with absolute time is significantly different for different slab size, shape and mantle rheology.

The 3-D slabs that are wider than ~ 300 km exhibit similar thinning rates as the corresponding 2-D slabs with the same material properties for both linear viscous and power-law viscous mantle. Therefore, the 1-D analytical solution for necking presented by Schmalholz (2011) can be applied at first-order accuracy to both 2-D and 3-D necking during slab detachment (Fig. 3.3a, d).

For the asymmetric slab the zone of localized thinning propagates laterally with a constant velocity of approximately 9 cm/yr for a linear viscous mantle and approximately 30 cm/yr for a power-law viscous mantle. These velocities are similar to the rates which are reported by van Hunen and Allen (2011) and Burkett and Billen (2011) who reported rates between 10 and 80 cm/yr. The measured velocities are also consistent with the natural rates inferred from the Trans-Mexican volcanic belt (10-25 cm/yr), which may reflect lateral propagation of slab detachment (Ferrari, 2004).

Seismic tomography have been imaging complex tomographic patterns around slab edges (Lallemand *et al.*, 2001; Lin *et al.*, 2004). In particular, slab gaps at slab edges have been evidenced by several studies in the Kamchatka region (Levin *et al.*, 2002, 2004; Jiang *et al.*, 2009). The simulations presented in chapter 3 show that such gaps can be the result of two processes: First, due to a true detachment of the slab, and second, due to the lateral deflection of the slab during the process of slab detachment. Therefore, not every gap in a vertical section of tomographic results around a slab edge must necessarily indicate a fully detached slab, but could also be due to a laterally deflected slab that is still attached. Lateral deflection of a slab side can be larger than 100 km (Fig. 3.4c and d) and also affects narrow slabs. This further suggests that small slabs can also produce "drop-like" shapes of fast seismic velocity anomalies such as observed in the Hindukush (Koulakov and Sobolev, 2006) or the Vrancea regions (Koulakov *et al.*, 2010).

However, natural slab detachment is a very complex process that is controlled by thermal, mechanical and chemical processes as well as their coupling (e.g shear heating in Gerya *et al.* (2004)). Our simulations for viscous necking during slab detachment are significantly simplified in order (1) to identify and quantify fundamental 3-D deformation processes during slab detachment, (2) to keep the model and the involved parameters comprehensible, and (3) to keep the computational costs low. More elaborated 3-D models are required in the future to model 3-D slab detachment in more detail.

in chapter 4 the 3-D numerical algorithm PINK-3D is applied to study the formation of fold nappes as the Morcles and Doldenhorn nappes as well as to the formation of the axial Rawil Depression. The cylindrical simulations for the formation of the Morcles and Doldenhorn fold nappes support the hypothesis that the weak basal sediments in the half graben deposits forming now the Doldenhorn nappe are likely to be thinner than the sediment in the half graben forming the Morcles nappe (Pfiffner, 2011). The different sediment thickness in the half graben controlled the different deformation style in the fold nappes. The deformed geometry of the simulation with the deep initial half graben shows similarities with the Morcles nappe. The layers which were first buckled and then sheared over the basement form a recumbent fold nappe with an overturned limb (Fig. 4.4c). The deformation is more localized and the fold nappe remains flatter for the simulation with thinner sediments in the half graben. This geometry is similar to the Doldenhorn nappe (Fig. 4.4f). In the same time as the fold nappe forms, the basement-sediment interface forms a cusate lobate structure (mullion). The orientation of this cusate-lobate structure is opposite to the orientation below the Morcles and Doldenhorn nappes

(Fig. 4.4c, f and Fig. 4.1a, b). This problem may be solved with an additional drag in x-direction at the bottom model boundary. A smaller initial half graben thickness can explain (i) the stronger shear deformation in overturned limb of the Doldenorn nappe compared to the one of the Morcles nappe, and (ii) the smaller overall thickness of the Doldenhorn nappe compared to the one of the Morcles nappe.

The full 3-D simulation with laterally varying graben depth shows small amounts of lateral extension in y-direction for the competent sedimentary layers (Fig. 4.6, Fig. 4.7 e to h). The amplitude of the forming fold nappe is higher for the deep sedimentary basement, whereas the deformation is more localized for the shallow half graben where the fold nappe remains flatter. Laterally, the fold nappes amplitude is decreasing towards the shallow half graben (Fig. 4.5). This difference in the amplification rates leads to lateral fold axis parallel extension. In the 3-D numerical simulations we obtain a fold axis parallel extension of up to 5% which is significantly smaller than the fold axis parallel extension which was reported by Dietrich (1989) from the measurements of pressure shadows, en échelon veins and fold axis parallel sections. Therefore, a bulk fold axis parallel extension, as we use in the simulations for the formation of the Rawil depression, is needed to explain these observed structures and measured extension values around the Rawil depression. However, the small internal extension of up to 5% is sufficient to generate extensional brittle structures such as veins and joints.

The performed 3-D simulation to study the formation of the Rawil depression show that it is possible to form a depression by horizontal compression and extension of a strong block an oblique half graben (representing a weak zone). The best fitting simulation for the formation of the Rawil depression is Rawil_65_6_1 with a graben orientation of 65° with respect to the x-direction, a power-law stress exponent of $n_b = 6$ in the basement and Newtonian sediments (i.e. $n_s = 1$). The results for this simulation show a depression in the basement as well as in the sediments and no asymmetric geometry of the basement. Some of the simulations show a asymmetric basement geometry, especially when we use a power-law stress exponent of $n_b > 1$ and $n_s = 3$ for the basement and sediments, respectively. The asymmetric basement geometry is characterized by a significantly lower basement topography and significantly steeper plunge (almost vertical) on one side of the model box. If we compare this geometry with the basement geometry of the Aiguilles-Rouges / Mt. Blanc massifs and the Aar massif, this asymmetric basement geometry seems unrealistic (Pfiffner *et al.*, 1997). The formation of the asymmetric basement geometry is likely because of the free slip boundary conditions which allow the basement to rotate around a

horizontal axis in x-direction. When we fix the vertical movement of the vertical boundaries we prevent the basement from becoming asymmetric. However, the magnitude of the depression remains more or less the same. The maximal slope of the depression in x-direction is 10° which is not as high as in the Rawil depression where we have slopes of up to 30° . The highest depression amplitudes are obtained with a graben which is oriented with an angle of 65° or 90° with respect to the x-direction. However, based on the today's orientation of the Carboniferous graben in the Aiguilles-Rouges massif (Fig. 4.2), the initial graben orientation of 90° with respect to the x-direction is improbable. The simulation results indicate that shortening of a basement with an oblique graben generates a depression but also that this process alone is not sufficient to generate the observed plunge of the fold axis of approximately 30° . Hence, additional processes must have been active to generate the observed plunge of the Rawil depression. The applied models are significantly simplified and effects such as a temperature dependent viscosity or a plastic yield strength have not been considered. A temperature dependent viscosity may cause a larger shear localization within the overturned limbs of the modelled fold nappes as shown by (Bauville *et al.*, 2013). A plastic yield strength may have affected especially the deformation in the upper part of the model above the fold nappes. Furthermore, during the Alpine deformation there was likely a significant amount of simple shear with a top-to-the NW shear sense and also some amount of vertical flattening. Such simple shear and flattening has also been ignored in our simple models. Such additional deformations will be investigated in future studies.

As part of this doctoral thesis, the presented 3-D algorithm PINK-3D is applied to a variety of problems in geoscience as slab detachment, fold nappe formation and basement-cover deformation. However, other possible applications and possible extensions of the presented simulations would be:

- Fold nappe formation and basement-cover deformation with basal drag boundary conditions.
- Formation of the Rawil depression with simple shear and additional flattening.
- Slab detachment with free surface boundary condition to track the lateral propagation of the surface response to the detaching slab.
- Lateral propagation of Rayleigh-Taylor diapirism with free surface boundary conditions.

DISCUSSION

- Lateral propagation of folding in both horizontal direction.
- Lateral propagation of necking under layer parallel extension in both directions and the formation of chocolate-tablet structures.
- And many others.

References

- Bauville A., Epard J.-L. and Schmalholz S., 2013: **A simple thermo-mechanical shear model applied to the Morcles fold nappe (Western Alps)**, *tectono* 583, 76–87
- Burkett E. R. and Billen M. I., 2011: **Three-dimensionality of slab detachment due to ridge-trench collision: Laterally simultaneous boudinage versus tear propagation**, *Geochemistry Geophysics Geosystems* 11, 189–203
- Dietrich D., 1989: **Fold-axis parallel extension in an accurate fold-and-thrust belt: the case of the Helvetic nappes**, *Tectonophysics* 170, 183–212
- Ferrari L., 2004: **Slab detachment control on mafic volcanic pulse and mantle heterogeneity in central Mexico**, *Geology* 32, 77–80
- Gerya T. V., Yuen D. A. and Maresch W., 2004: **Thermomechanical modelling of slab detachment**, *Earth and Planetary Science Letters* 226, 101–116
- Jiang G., Zhao D. and Zhang G., 2009: **Seismic tomography of the Pacific slab edge under Kamchatka**, *Tectonophysics* 465, 190–203
- Koulakov I. and Sobolev S., 2006: **A tomographic image of Indian lithosphere break-off beneath the Pamir-Hindukush region**, *Geophys. J. Int.* 164, 425–440
- Koulakov I., Zaharia B., Enescu B., Radulain M., Popa M., Parolai S. and Zschau J., 2010: **Delamination or slab detachment beneath Vrancea? New arguments from local earthquake tomography**, *Geochemistry Geophysics Geosystems* 11, Q03002
- Lallemand S., Font Y., Bijwaard H. and Kao H., 2001: **New insights on 3-D plates interaction near Taiwan from tomography and tectonic implications**, *Tectonophysics* 333, 229–253
- Levin V., Shapiro N., Park J. and Ritzwoller M., 2002: **Seismic evidence for catastrophic slab loss beneath Kamchatka**, *Nature* 418, 763–767
- Levin V., Shapiro N., Park J. and Ritzwoller M., 2004: **Slab portal beneath the western Aleutians**, *Geology* 33, 253–256

- Lin J.-Y., Hsu S.-K. and Sibuet J.-C., 2004: **Melting features along the western Ryukyu slab edge (northeast Taiwan): Tomographic evidence**, *Journal of Geophysical Research* 109, B12402
- Moresi L., Quenette S., Lemiale V., Meriaux C., Appelbe B. and Mühlhaus H.-B., 2007: **Computational approaches to studying non-linear dynamics of the crust and mantle**, *Physics of the Earth and Planetary Interiors* 163, 69–82
- Pfiffner A., Lehner P., Heitzmann P., Mueller S. and Steck A., 1997: **Deep structure of the Swiss Alps: Results of NRP 20**, Birkhäuser Verlag, Basel, Boston, Berlin
- Pfiffner O., 2011: **Structural Map of the Helvetic Zone of the Swiss Alps, including Vorarlberg (Austria) and Haute Savoie (France), 1:100000**, Geological Special Map 128. Explanatory notes.
- Schmalholz S. M., 2011: **A simple analytical solution for slab detachment**, *Earth Planetary Science Letters* 304, 45–54
- Thielmann M., May D. and Kaus B., 2014: **Discretization Errors in the Hybrid Finite Element Particle-in-cell Method**, *Pure and Applied Geophysics* pages 1–20, doi:{10.1007/s00024-014-0808-9}
- van Hunen J. and Allen M. B., 2011: **Continental collision and slab break-off: A comparison of 3-D numerical models with observations**, *Earth Planetary Science Letters* 302, 27–37

6 Conclusions

The presented 3-D algorithm that combines a deformable Lagrangian mesh and a material-interface technique with re-meshing can handle a power-law visco-elastic rheology. The algorithm is therefore suitable to model structures that emerge due to hydrodynamic instabilities which are caused by large and sharp contrasts in material parameters (e.g. mechanical strength and density) between different rock units. The Lagrangian FE formulation is suitable to accurately resolve the small initial geometrical instabilities (i.e. geometrical perturbations) of the material interfaces that control the instability. The Eulerian re-meshing formulation on the other hand is suitable to simulate the large strain evolution of structures emerging from initial geometrical instabilities.

The presented algorithm is especially suitable to exactly follow material interfaces in 3-D for large strains, because (i) the interface-points on the material interface are accurately deformed with the deforming Lagrangian finite element mesh, and (ii) the element velocities are accurate also for elements that include integration points with strongly varying material properties, that is, for elements that are crossed by material interfaces due to re-meshing. Further the presented 3-D algorithm is useful to quantify and visualize finite strain either by finite strain ellipsoids or by passively deformed initial circles on the material interfaces. Such quantification of finite strain is useful to better understand the 3-D evolution of processes such as necking and folding which control to a large extent the evolution of geodynamic processes such as slab detachment or fold nappe formation. In nature, these processes often exhibit a significant 3-D deformation and the resulting structures often exhibit a complicated 3-D geometry. Hence, 3-D numerical models are required to better understand these processes and interpret the observed 3-D data and geometry.

The simulations applied to the viscous necking during slab detachment were performed in order to quantify the 3-D deformation during the buoyancy-driven necking of a laterally finite slab of power-law viscous fluid surrounded by a linear or power-law viscous mantle. The evolution of localized slab thinning (necking) with increasing vertical bulk extension of the slab is only weakly dependent on the slab size, the slab shape (symmetric or asymmetric), and the width of the mantle adjacent to the lateral slab side. During necking of the slab the vertical sides of

CONCLUSIONS

the slab around the depth of necking deflect significantly in the lateral (along-trench) direction. Absolute values of lateral deflection increase with increasing slab size. This lateral deflection can be > 100 km, and could explain gaps in seismic tomography cross sections despite the fact that the slab is still attached.

Further, we performed 3-D numerical simulations of viscous flow to study and quantify the formation of fold nappes during the inversion of a half graben with laterally varying thickness. The half graben was filled with mechanically competent layers of equal thickness and with weak material of correspondingly laterally varying thickness. The simulations show that the thickness of weak material in the half graben has a significant impact on the fold nappe evolution. Fold nappes that are generated from a thicker half graben have (i) larger amplitudes, (ii) a less sheared and thinned overturned limb, and (iii) a larger nappe thickness than fold nappes that are generated from a thinner half graben. These three differences are observed between the Morcles and Doldenhorn nappes. Our simulations therefore support the field based interpretations that the first order structural differences between the two nappes are due to a different pre-Alpine thickness of the half graben in which the sediments that build now the two nappes have been deposited during mainly the Mesozoic. The simulations also show that during the shortening the half graben is closed and forms a mullion-like structure which also agrees with field observations. The viscous flow simulations can generate many first order features of the Morcles-Doldenhorn nappe system and suggest that ductile deformation (and not brittle) was likely the dominant deformation behaviour during fold nappe formation and related basement deformation.

The simulations also show that the laterally varying fold amplification causes a fold-axis-parallel extension of up to 5% in the layers although the bulk extension is zero. Such extension could explain brittle extensional structures that are observed in the competent layers of the fold nappes. However, this internal extension cannot explain the overall orogen-parallel extension in the Helvetic nappe system which is significantly larger.

We also performed 3-D numerical simulations of viscous flow to study and quantify the impact of an oblique half graben in the basement on the basement uplift during shortening accompanied by orthogonal extension. The results show that the half graben can cause a laterally varying basement uplift which generates a depression similar to the Rawil depression. The amplitude of the depression depends on the initial orientation of the graben and the power-law stress exponent

CONCLUSIONS

of the basement and sediments. The maximal axial plunge of the modelled depression is only approximately 10 degrees whereas the maximal observed plunge of the Rawil depression is approximately 30 degrees. The results therefore indicate that an oblique graben in the basement may have contributed to the formation of the Rawil depression but that additional processes are required to generate the observed geometry of the Rawil depression.

In general the presented PhD thesis showed the importance of the third dimension for the numerical modelling of geological structures. The 3-D deformation of laterally varying initial geometries as for example a laterally varying graben depth in a compressed half graben, a laterally varying slab length of a detaching slab or an oblique graben (i.e., weak zone) in a compressed and stretched model configuration is not trivial at all. A laterally varying initial geometry influences the final geometry significantly. The presented algorithm PINK-3D is suitable to simulate the deformation of such laterally varying initial geometries as well as to quantify and visualize quantities as stress, strain rate, effective viscosity or finite strain in three dimensions. The advantage of the presented 3-D numerical algorithm is that it can be run on a standard workstation with MATLAB without the need of installing any additional libraries.

Appendix A

Intersection ellipses

Stress and strain in three dimensions are described by ellipsoids in 3-D space. However, measurement in the field usually include only two-dimensional data on a plane (e.g. the material interface). Therefore, we are interested in the intersection of an ellipsoid with a plane. There exist different analytical solutions to solve this problem (Ramsay, 1967; Ferguson, 1979; Gendzwill and Stauffer, 1981) which calculate the intersection ellipse on a given plane or the ellipsoid from three intersection ellipses. However, we use a numerical solution which is easier to implement.

A.1. Calculation of intersection ellipses

The function which calculates the ellipsoid and the intersection ellipses on a plane through the ellipsoid's center is called: `fct_ellipsoid_intersection_hc`. The inputs for this function are the center point of the ellipsoid, the Tensor which describes the ellipsoid (Cauchy-Green tensor) and the normal vector of the plane. The outputs are the surface coordinates of the ellipsoid, the coordinates of the intersection ellipse, the indexes of the half axis and the half axis of the ellipsoid as well as the coordinates of the intersection ellipse. The normal vector of a plane can be easily found using three points on the plane (A,B,C) and take the crossproduct of two vectors on the plane (AB,AC). Note, that the normal vector should be normalized by its own length. Here we give a step by step description of the function:

1. Find eigenvalues of tensor T and define the half axis.
2. Rotate ellipsoid coordinates and normal vector such that the half axis are parallel to the coordinate system.
3. Create ellipsoid using the Matlab function "ellipsoid".

4. In order to find the intersection points between the ellipsoid and the plane we define a line on the plane which goes through the center of the ellipsoid. For this line we search for the intersection points with the ellipsoid. Then we rotate the line in small steps and calculate the intersection points again. For this we define a vector α which goes in small steps from 0 to π . The line is then defined as:

$$x = y \tan \alpha \quad (\text{A.1})$$

5. The equation for the plane is given by:

$$dx + ey + fz = 0 \quad (\text{A.2})$$

where (d, e, f) is the normal vector to the plane which goes through (0,0,0)

6. The equation for the ellipsoid is:

$$\frac{x^2}{a^2} + \frac{y^2}{b^2} + \frac{z^2}{c^2} = 1 \quad (\text{A.3})$$

where a, b and c are the half axis in x-, y- and z- direction, respectively.

7. The line defined in equation A.1 is part of the plane. Therefore, we substitute equation A.1 into the equation A.2 for the plane:

$$d y \tan \alpha + ey + fz = 0 \quad (\text{A.4})$$

and solve it for y:

$$y = \frac{-f}{d \tan \alpha + e} z \quad (\text{A.5})$$

8. In order to find the intersection of this line with the ellipsoid we substitute the equation A.1 and A.5 into the equation A.3 for the ellipsoid:

$$\frac{B^2 z^2}{a^2} + \frac{A^2 z^2}{b^2} + \frac{z^2}{c^2} = 1 \quad (\text{A.6})$$

where $A = -f/(d \tan \alpha + e)$ and $B = -f \tan \alpha / (d \tan \alpha + e)$.

9. Now, we solve equation A.6 for z and get:

$$z^2 = \frac{a^2 b^2 c^2}{B^2 b^2 c^2 + A^2 a^2 c^2 + a^2 b^2} = E^2 \quad (\text{A.7})$$

which will give us two solutions for z :

$$z = \pm E \quad (\text{A.8})$$

10. Together with equation A.1 and A.5 we end up with:

$$z = \pm E \quad (\text{A.9})$$

$$y = Az \quad (\text{A.10})$$

$$x = Bz \quad (\text{A.11})$$

11. These two solutions lie on the initially defined line opposite of each other. If we now calculate the distance between all these pairs of points, take the maximum and minimum we will find the half axis of the intersection ellipsoid.
12. Save all coordinates of the points of the intersection ellipse as well as indexes for the half axis for later visualization.
13. Rotate coordinates of the ellipsoid and the intersection ellipse back to the original coordinate system and translate both to the original center point.

Figure A.1 shows the intersection ellipse and the its half axis of a given general ellipsoid and a given plane.

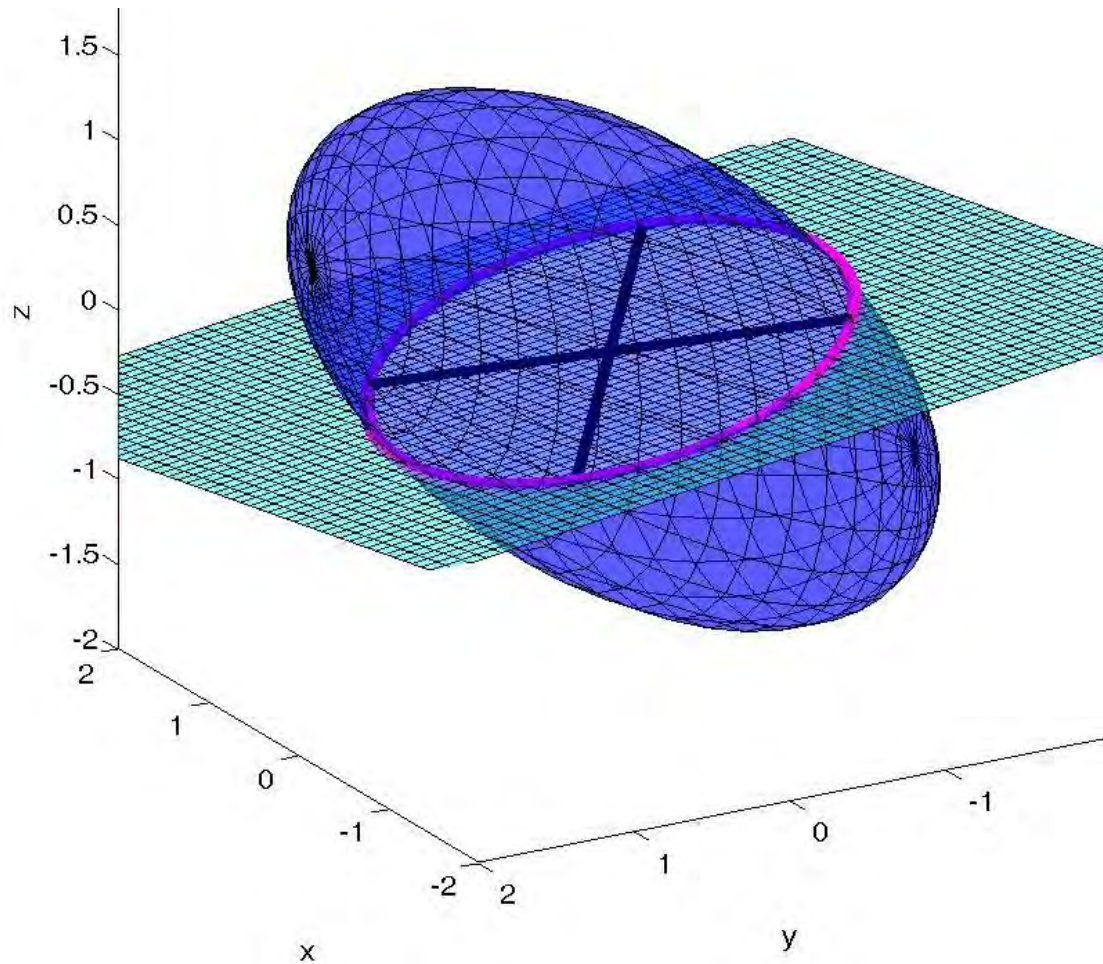


Figure A.1: Intersection ellipse (pink) and its half axis (black) for a given ellipsoid (blue) and a given plane (cyan).

The presented algorithm to calculate and visualize the intersection ellipse of a given ellipsoid and a given plane can be used to for example visualize the finite strain on material interfaces. Figure A.2 shows the results for 3-D fold nappe formation with an initial laterally varying geometry. The figure shows the intersection ellipses and the their half axis of the finite strain ellipsoids with the material interface between the basement and sediments as well as on the material in-

terface between competent and weak sediments. Note, that the intersection ellipses are oriented tangentially to the material interfaces.

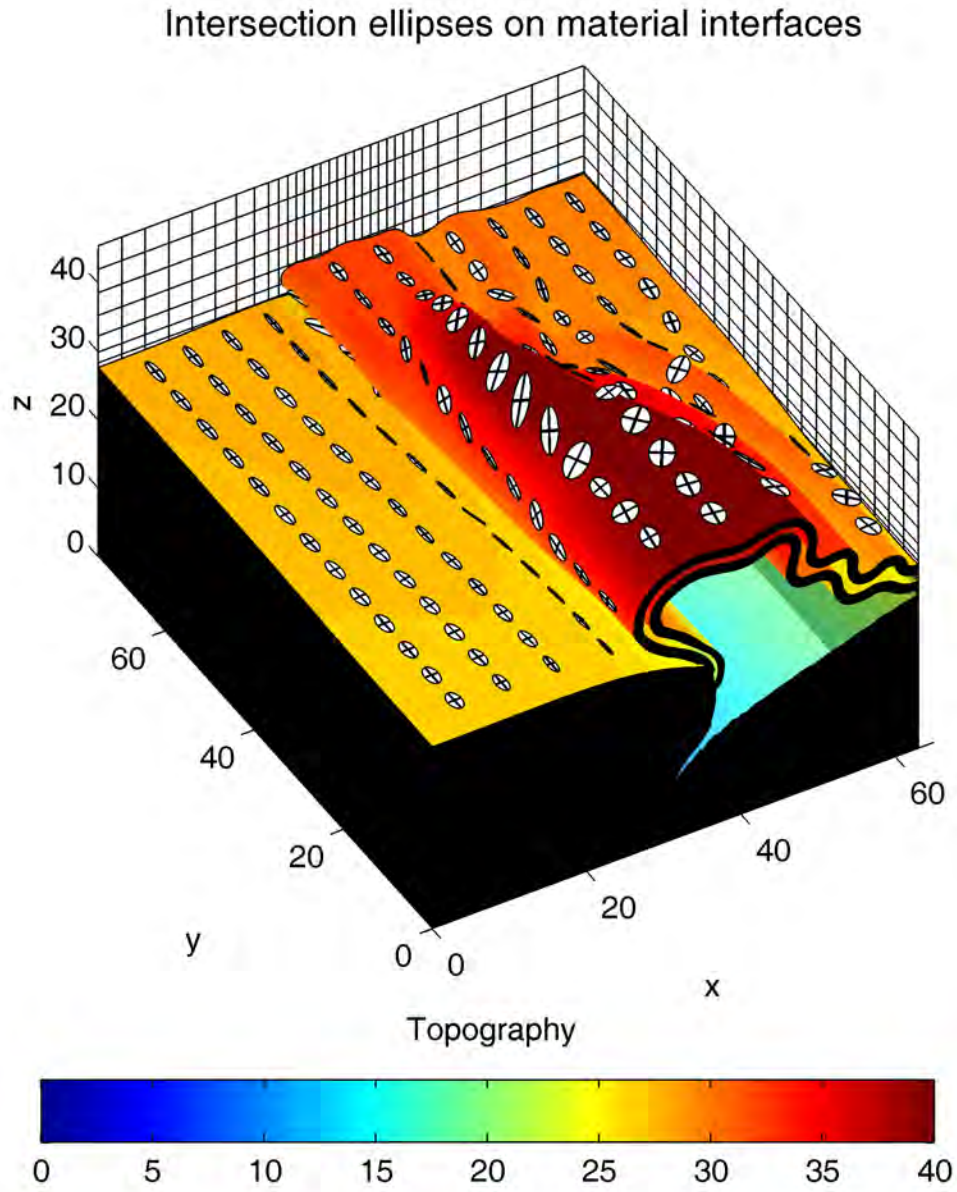


Figure A.2: Intersection ellipses for finite strain ellipsoid on the material interfaces. The colors indicate the dimensionless topography of the material interfaces.

References

Ferguson C., 1979: **Intersection of Ellipsoids and Planes of Arbitrary Orientation and Position**, *Mathematical Geology* 11, 329–336

Gendzwill D. and Stauffer M., 1981: **Analysis of Triaxial Ellipsoids: Their Shapes, Plane Sections, and Plane Projections**, *Mathematical Geology* 13, 135–152

Ramsay J. G., 1967: **Folding and fracturing of rocks**, McGraw-Hill, New York, N.Y.

Acknowledgements

First and most of all I would like to thank Stefan for supervising this PhD and for motivating and fascinating me for numerical modelling and finite elements (thank you to endure me for a PhD after my Bachelor and Master Thesis). I'm proud to have the opportunity to work with you. Further, I'd like to thank you to accept my wish to mainly work from home when I did not feel comfortable in Lausanne. And last but not least, thank you for not complaining about using pink and magenta in uncounted figures and even the name of the algorithm :). Dank.

Next, I want to thank Yuri for the help with the code and many explanations and discussions on how the algorithm is implemented. Honestly, I did not always understand what you wanted to tell me but I learned a lot by listening to you, also at lunch conversations and seminar discussions. Спасибо.

Further thank goes to Jean-Luc who went to the field with Arthur and me to show me real rocks, real geology and the Morcles nappe. Thanks also for many discussions on the model configurations which we designed for the simulations to study the formation of fold nappes and the Rawil depression. Merci beaucoup de partager tes connaissances avec moi.

Thibault, it was a pleasure to work with you. It was always fun. Thank you for the collaboration and the help with the inclusion test. Merci beaucoup aussi pour les discussions à propos du code.

Further, I want to thank Boris Kaus for the explanations about the 3-D analytical solution of the Raileigh-Taylor instability and for being the external expert of my PhD defence. Hartelijk dank.

I also want to thank Dave May for answering uncounted and sometimes stupid questions via e-mail and for many helpful comments on the manuscripts.

I thank my office mates in Lausanne Arthur, Yoann, Ludovic and Samuel for sharing the office in Geopolis with me. Thanks to Yoann and Arthur for taking care of my computer and for tracking my IP address for remote desktop. Thank you Yoann for correcting my bumpy french abstract.

I guess you had a lot to laugh. I thank Arthur, Yoann, Xavier, Thibault and Laure for funny lunch breaks, conferences and field trips during these four years. Sylvia, thank you for good and helpful private conversations, thank you for listening to my problems in bad times. Vielen Dank.

Further, I want to thank the administrative staff of the University in Lausanne, especially Krystel and Anne-Marie. Thanks to Philippe Logean for taking care of my simulations on achilles.

Last but not least, I want to thank my family, my parents and especially my husband Jan for standing behind me all the time and when I mutated from early bird to night owl in the final stage of my PhD. I love you all...

Curriculum Vitae

Personal Details

Name Marina von Tscharner
Birth date May 2th 1983
Birth place Chur, Switzerland
Nationality Swiss

Education

2011 – 2014 Ph.D. at Institute de geologie et paleontologie of University Lausanne, Switzerland
Committee: Prof. Dr. Stefan M. Schmalholz
Prof. Dr. Yuri Podladchikov
Prof. Dr. Boris Kaus
Prof. Dr. Eric Verecchia

2005 – 2010 Studies of Earth Science at ETH Zurich, Switzerland
Major subject: Structural Geology, Tectonics and Geodynamics
Minor subjects: Sedimentology and Stratigraphy, Petrography
Geochemistry and Isotope Geology
Master thesis: Finite Element simulations of subduction zones
and the formation of backarc basins

2003 – 2005 4 Semesters Studies of Physics at ETH Zurich, Switzerland
1999 – 2003 Swiss Matura with major subject Physics and applied Mathematics
Bündner Kantonsschule, Chur, Switzerland

Work experience

2011 – 2014 Research Assistant, Institut de geologie et paleontologie, Uni Lausanne, Switzerland

Teaching experience

2011 – 2014 Teaching Assistant, Institut de geologie et paleontologie, Uni Lausanne, Switzerland
including courses on the finite element method, Geodynamics, tectonics,
geological field courses, fundamentals of earth science

2007 – 2010 Teaching Assistant, Institut of Geology, ETH Zurich, Switzerland
including courses on mathematics, fundamentals of geology and
geological field courses, fundamentals of earth science

Publications and conference presentations

Publications

von Tscharnner M., Schmalholz S.M., Duretz T., Three-dimensional necking during viscous slab detachment. *Geophysical Research Letters* 41, 4194-4200

Conference presentations and seminar talks

- | | |
|-----------------|--|
| 11-13.11. 2011 | 9 th Swiss Geoscience Meeting, Zurich, Switzerland
3D FEM modeling of fold nappe formation in the Western Swiss Alps (poster) |
| 2.12. 2011 | Journee Lemanique, Lausanne, Switzerland
3D FEM modeling of fold nappe formation in the Western Swiss Alps (talk) |
| 22.-27.4. 2012 | EGU, Vienna, Austria
3D FEM modeling of fold nappe formation in the Western Swiss Alps (talk) |
| 16.-18.7. 2012 | GeoMod 2012, Lausanne, Switzerland
3D FEM modeling of fold nappe formation in the Western Swiss Alps (poster) |
| 16.-17.11. 2012 | 10 th Swiss Geoscience Meeting, Bern, Switzerland
3D FEM modeling of fold nappe formation in the Western Swiss Alps (poster) |
| 27.3.2013 | Geophysical Fluid Dynamics Group Seminar, ETH Zurich, Switzerland
3D FEM modelling of geological structures caused by geometrical instabilities and contrasts in rock strength (talk) |
| 7.-12.4. 2013 | EGU, Vienna, Austria
3D FEM modelling of geological structures caused by geometrical instabilities and contrasts in rock strength (poster) |
| 7.-14.9. 2013 | Emile Argand Conference, Schladming, Austria
11 th Worksho on Alpine Geological Studies
3D FEM modeling of fold nappe formation in the Western Swiss Alps (poster) |

- 15.-16.11. 2012 11th Swiss Geoscience Meeting, Lausanne, Switzerland
(1) 3-D FEM modelling of geological structures caused by geometrical instabilities and contrasts in rock strength (poster)
(2) Slab detachment – 3D versus 1D (poster)
- 27.4.-2.5. 2014 EGU, Vienna, Austria
(1) 3-D FEM modelling of geological structures caused by geometrical instabilities and contrasts in rock strength (poster)
(2) Slab detachment – 3-D versus 1-D & 2-D (poster)
- 5.-6.5. 2014 Tectonomechanics Colloquium 2014, Zurich, Switzerland
(1) 3-D FEM modelling of geological structures caused by geometrical instabilities and contrasts in rock strength (poster)
(2) Slab detachment – 3-D versus 1-D & 2-D (poster)
- 16.-18.7. 2014 GeoMod 2014, Potsdam, Germany
A 3-D Lagrangian finite element algorithm with contour-based re-meshing for simulating large-strain hydrodynamic instabilities in visco-elastic fluids (poster)
- 21.-22.11. 2014 12th Swiss Geoscience Meeting, Fribourg, Switzerland
3D FEM modelling of fold nappe formation and the Rawil depression in western Switzerland (poster)